

# Comparative Binding Analysis of Pyrimidine Derivative to BSA: Equilibrium, FTIR and Acoustical Study

Ajay Madhukarrao Pisudde, Pradip Vitthalrao Tekade\*, Shrikant Bandupant Thakare

Department of Chemistry, Jankidevi Bajaj College of Science, Jamnalal Bajaj Marg, Civil lines, Wardha-442001-M.S. India

Article history: Received: 14 November 2017; revised: 06 January 2018; accepted: 01 February 2018. Available online: 29 March 2018. DOI: <http://dx.doi.org/10.17807/orbital.v10i2.1116>

## Abstract:

This paper presented the comparative binding interaction of ethyl-4-(4-hydroxyphenyl)-6-methyl-2-oxo-1,2,3,4-tetrahydropyrimidine-5-carboxylate (4-HP2OTP) and ethyl-4-(2-hydroxyphenyl)-6-methyl-2-thioxo-1,2,3,4-tetrahydropyrimidine-5-carboxylate (2-HP2STP) to bovine serum albumin (BSA) in 1,4-dioxane, DMSO and DMF by equilibrium dialysis, FT-IR and acoustical study at physiological pH. The binding data obtained was interpreted by scatchard plot, which gives the association constants. An increase in association constants is observed with increase in temperature and concentration. FT-IR study explains the binding through shifting in peak positions of amide I and II. It explained the changes in secondary structure of BSA on binding with the drugs. The free energy ( $\Delta G$ ), enthalpy ( $\Delta H$ ) and entropy ( $\Delta S$ ) values were calculated by using van't Hoff equation. The negative  $\Delta G$  showed the spontaneous process and positive values of  $\Delta H$  and  $\Delta S$  showed endothermic interaction between ligands and BSA.  $\Delta G$  becomes more negative with increased in temperature, indicated feasibility of binding interaction at high temperature. The positive values of  $\Delta H$  and  $\Delta S$  also showed specific electrostatic and hydrophobic interaction between ligand and BSA.

**Keywords:** equilibrium dialysis; FT-IR; acoustical study; BSA; scatchard analysis; thermodynamic parameters

## 1. Introduction

Serum albumins are the most abundant proteins in the circulatory system of wide variety of organisms, being the major macromolecules contributing to the osmotic blood pressure [1]. Their functional and physiological properties have been studied over several decades [2]. These proteins have long been used as model proteins in both industrial and academic research areas [3]. The protein is single polypeptide chain of 585 amino acids with a large helical triple domain structure with the concentration of 0.63 mM in the blood. Protein binds relatively a number of insoluble endogenous drugs such as unesterified fatty acids, bilirubin and bile ducts and thus facilitates their transport. A variation in temperature is found to be a key factor in binding affinities of proteins [4] as evident from the drugs

ligustrazine [5], ciprofloxacin [6], methotrexate [7] and cisplatin [8]. 4-HP2OTP and 2-HP2STP are the poly-functionalized dihydropyrimidine compounds exhibiting a broad range of therapeutic and pharmacological [9], anticarcinogenic [10], antihypertensive, antiviral, antitumor, antibacterial, anti-inflammatory, calcium channel modulators [11], antimycobacterial and anticonvulsant [12], anticancer [13] properties. Human serum albumin (HSA) and BSA exhibit similar chemical properties due to high percentage of sequence identities. BSA in lieu of HSA was used in this study because of low cost and easy availability. In BSA varying binding sites are available for ligands [14-15]. Ranges of techniques are available to monitor the binding interactions of ligands to protein viz. NMR [16], isothermal titration calorimetry (ITC) [17], UV- visible absorbance [18], fluorescence [19],

\*Corresponding author. E-mail:  [pradiptekade@gmail.com](mailto:pradiptekade@gmail.com)

FT-IR and CD spectroscopy [20].

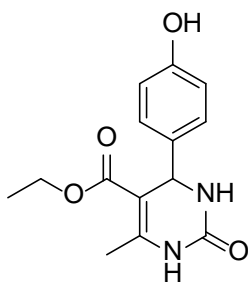


**Figure 1.** Ethyl 4-(4-hydroxyphenyl)-6-methyl-2-oxo-1,2,3,4-tetrahydropyrimidine-5-carboxylate (4-HP2OTP)

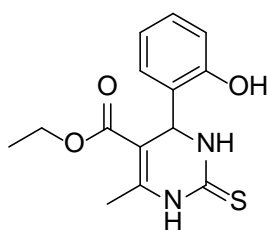


**Figure 2.** Ethyl 4-(2-hydroxyphenyl)-6-methyl-2-thio-1,2,3,4-tetrahydropyrimidine-5-carboxylate (2-HP2STP).

In the view of above considerations, present study demonstrates the effect of drug concentration, temperature and polar/non-polar solvent on binding interaction of ligands to BSA at

physiological pH and determination of thermodynamic parameters like free energy, enthalpy and entropy.

## 2. Results and Discussion

### Equilibrium dialysis

The binding parameters of 4-HP2OTP-BSA and 2-HP2STP-BSA complexes have been determined using scatchard analysis. Scatchard curves obtained by plotting the absorbance and specific binding against the concentrations of ligands. Different observations have noticed for both the drugs in all the solvents. The association constants for 4-HP2OTP are found to be 0.7845 ( $\pm 0.0005$ ), 0.7185 ( $\pm 0.0005$ ), 0.7305 ( $\pm 0.0005$ ) in 1,4-dioxane, DMSO and DMF respectively. While the association constants for 2-HP2STP are in 1,4-dioxane, DMSO and DMF are 0.7405 ( $\pm 0.0005$ ), 0.7265 ( $\pm 0.0005$ ), 0.7265 ( $\pm 0.0005$ ) respectively. It has been seen that, the binding affinity of 4-HP2OTP is slightly more than 2-HP2STP in 1,4-dioxane than DMSO and DMF. The scatchard analysis of binding of 4-HP2OTP & 2-HP2STP with BSA at pH 7.4 in all the solvents were provided a non-linear curve. This suggests the presence of at least two binding sites for the binding of the ligands to BSA. Figures 3 and 4 shows the scatchard plots of BSA-ligands complexes in 1,4-dioxane, DMSO and DMF.

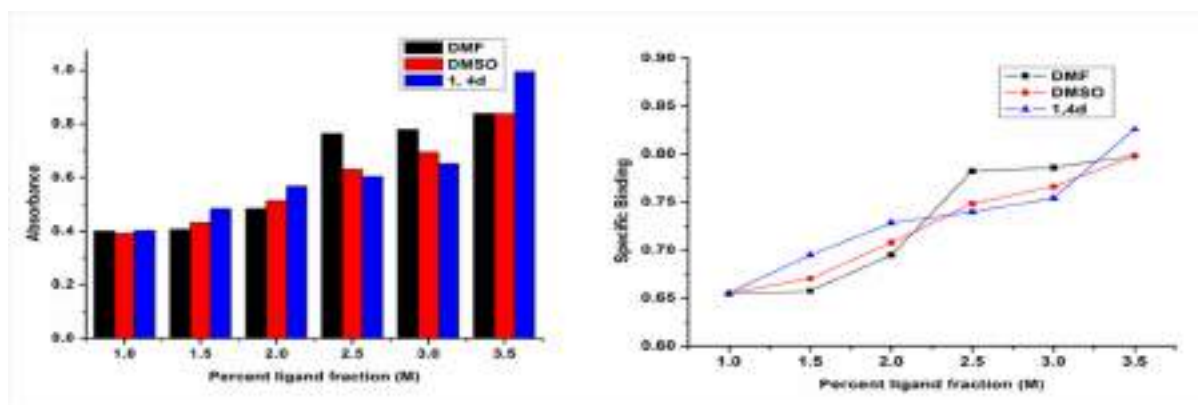


**Figure 3.** Scatchard plot of 4-HP2OTP-BSA complex in 1,4-dioxane, DMSO, DMF at room temperature.

### Effect of foreign particles

The binding analysis of 4-HP2OTP and 2-HP2STP to BSA is also studied in presence of foreign particles. Results obtained are interpreted

by the Scatchard plot (Figure 5 and 6). The association constants for 4-HP2OTP-BSA and 2-HP2STP-BSA complexes in presence of foreign particles are 0.7006 ( $\pm 0.0005$ ) & 0.5757 ( $\pm 0.0005$ ) for Hg and 0.6782 ( $\pm 0.0005$ ) & 0.6855 ( $\pm 0.0005$ )

respectively. The association constant for 4-HP2OTP and 2-HP2STP in absence of impurities of foreign particles were  $0.7305 (\pm 0.0005)$  and  $0.7261 (\pm 0.0005)$ . It is noticed that the binding of

these ligands is decreased in presence of foreign particles may be due to packing of binding sites in the BSA.

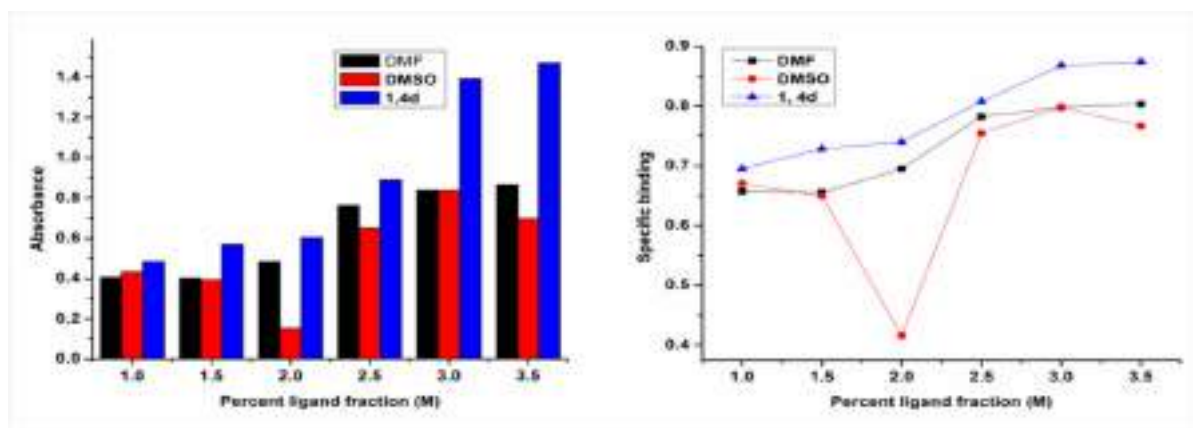


**Figure 4.** Scatchard plot of 2-HP2STP -BSA complex in 1,4-dioxane, DMSO, DMF at room temperature.

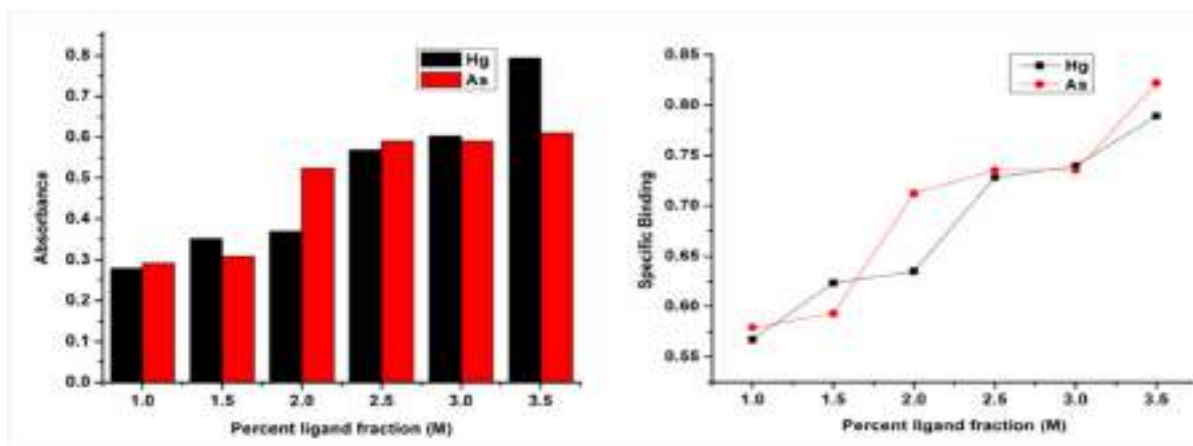


**Figure 5.** Effect of As and Hg on scatchard plot of 4-HP2OTP-BSA complex in 1, 4 dioxane.

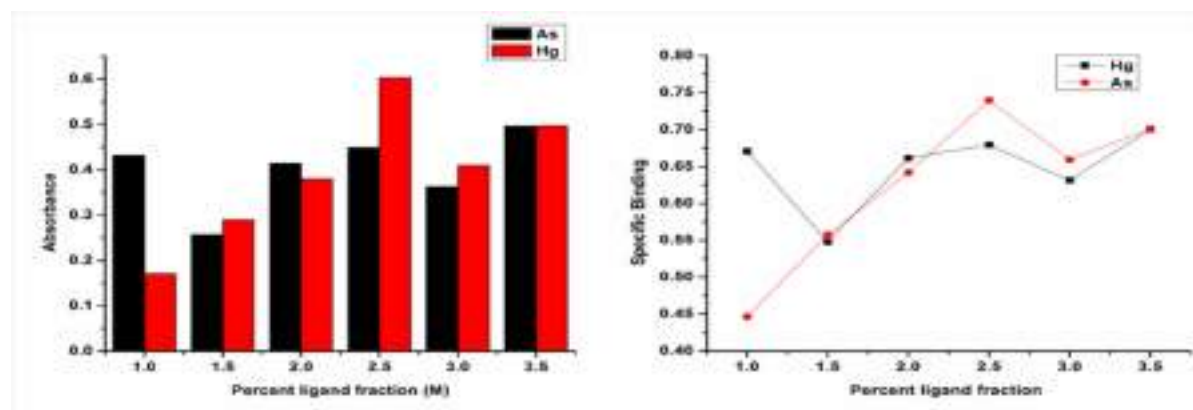


**Figure 6.** Effect of As and Hg on scatchard plot of 2-HP2STP-BSA complex in 1,4-dioxane.

### FT-IR analysis

The protein drug binding by FT-IR spectroscopy is analyzed by shifting of amide bands in BSA. The amide I band at  $1635\text{ cm}^{-1}$  is due to C=O stretching and amide II band at  $1543\text{ cm}^{-1}$  is due to C-N stretch coupled with N-H bending. A change in frequency of these bands is observed on binding of ligands to BSA. Similar to ultrasonic and equilibrium dialysis study, more binding is observed in case 1,4-dioxane than DMSO & DMF. The peak position of amide I is shifted from  $1635$  to  $1650\text{ cm}^{-1}$  in 4-HP2OTP and to  $1644\text{ cm}^{-1}$  in 2-HP2STP as compared to BSA. However, a very small change is observed in the shifting of amide II band in the complex. It is noticed that, as the concentration of ligands increases the frequency of the binding of amide I bands is also increases (Figure 7 and 8). As amide I band is more sensitive to the changes of secondary structure of BSA than amide II therefore increase in binding is characterized by shift in amide I band. Similarly, BSA-ligands binding are not as much as significant in case of DMSO and DMF.

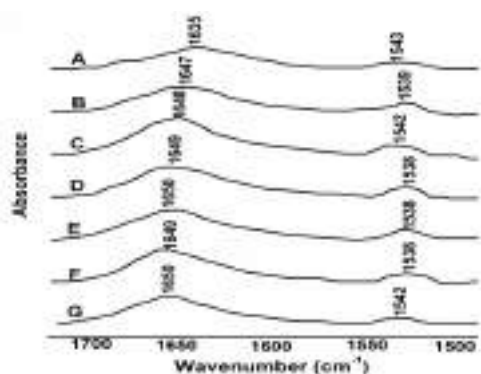


**Figure 7.** FT-IR spectra of 4-HP2OTP-BSA complex in 1,4-dioxane.

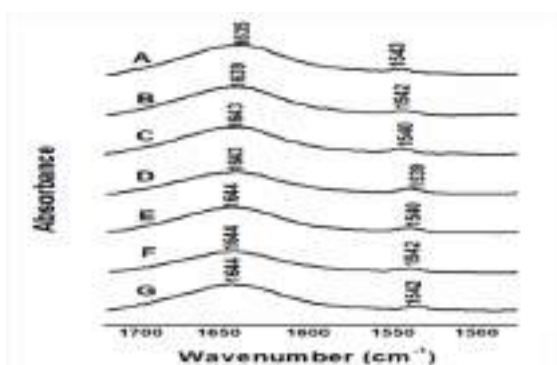


**Figure 8.** FT-IR spectra of 2-HP2STP-BSA complex in 1,4-dioxane.

### Ultrasonic study

In present study, ultrasonic velocities of  $0.15\text{ }\mu\text{M}$  BSA are measured at temperature 298, 303 and 308K and are found to be 1390.301, 1393.720 and 1398.105 m/s respectively. Ultrasonic velocities of 4-HP2OTP-BSA and 2-HP2STP-BSA complexes are also measured at various concentrations and temperatures (Table 1 and 2). It is observed that different values are obtained at different concentrations and temperatures for the ligands.

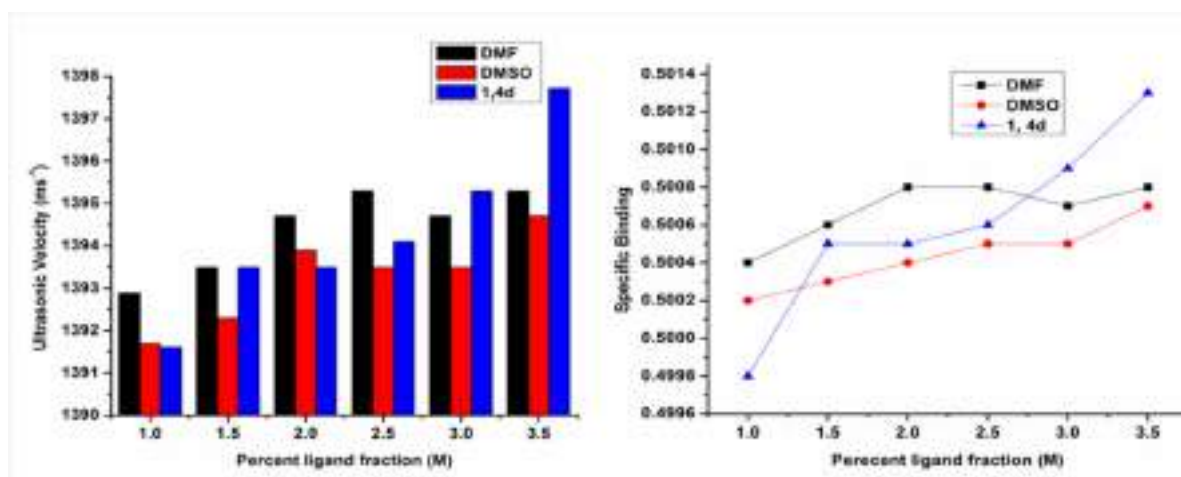
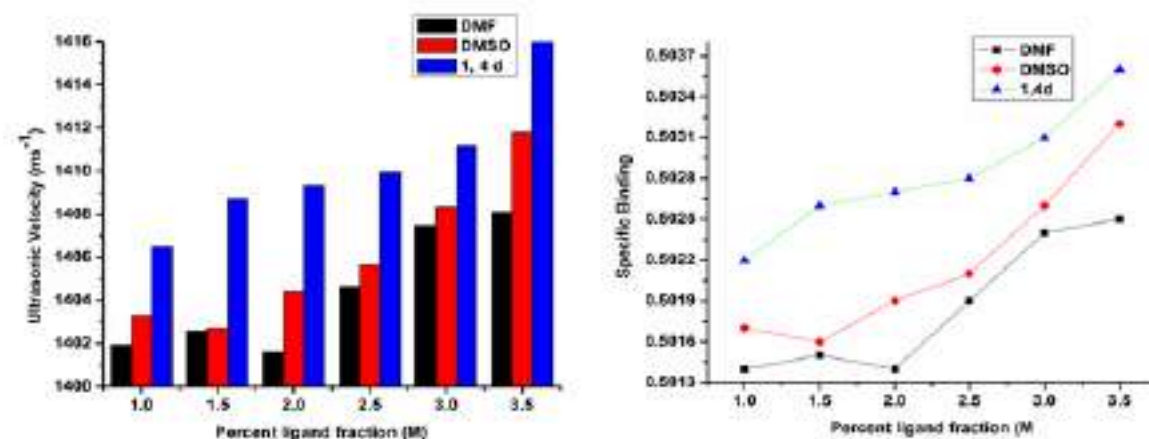
The Scatchard graph has plotted against ultrasonic velocity and specific binding versus percent ligand fraction. Binding parameters of 4-HP2OTP and 2-HP2STP to BSA have been determined using Scatchard plot. The Scatchard analysis gave different association constants at different temperatures and solvents. It is found that the association constants in 1, 4-dioxane at 308K is higher than 298K and 303K than DMSO and DMF. It means that the association constants for binding are more significant in 1,4-dioxane at high temperature, concluding that the binding increases with the increased in temperature. Binding is more significant in 1,4-dioxane than DMSO and DMF which is due to aprotic and non-polar nature of 1,4-dioxane. Comparatively binding is more significant in 4-HP2OTP than 2-HP2STP. From the structural analysis it is evident that, more binding of 4-HP2OTP is may be due to greater hydrogen bonding of oxygen in 4-HP2OTP than sulphur in 2-HP2STP. This increase of association constants in 1, 4-dioxane at high temperature clearly indicates the endothermic nature of reaction. This supports the interaction of ligands to BSA by means of Vander Waal's interactions and hydrogen bonds in the hydrophobic packet of binding sites. It is also observed that binding affinity increased as the concentration of the ligands increases; this probably enhances the pharmacological activity of the drug. Figures 9 to 11 shows the Scatchard plots of BSA-4-HP2OTP binding in 1,4-dioxane, DMSO and DMF at 298, 303 and 308 K respectively. Similarly figures 12 to14 shows the Scatchard plots of BSA-2-HP2STP binding in 1,4-dioxane, DMSO and DMF at 298, 303 and 308 K, respectively. The effect of temperature on BSA-ligands binding is summarized in van't Hoff equation.

**Table 1.** Ultrasonic velocities of 4-HP2OTP -BSA complex solutions at diff. conc. and temperature.

Temp	25 °C			30 °C			35 °C		
	1,4-Dioxane	DMSO	DMF	1,4-Dioxane	DMSO	DMF	1,4-Dioxane	DMSO	DMF
1	1391.607	1391.688	1392.890	1406.481	1403.301	1401.943	1414.413	1413.599	1412.266
1.5	1393.492	1392.289	1393.492	1408.711	1402.720	1402.584	1416.757	1414.271	1414.892
2	1393.492	1392.890	1394.698	1409.327	1404.416	1401.599	1417.379	1418.626	1415.513
2.5	1394.095	1393.492	1395.301	1409.943	1405.641	1404.641	1418.003	1418.003	1417.379
3	1395.301	1393.492	1394.698	1411.177	1408.327	1407.481	1422.096	1419.251	1416.757
3.5	1397.720	1394.698	1395.301	1416.125	1411.794	1408.096	1424.266	1419.876	1419.876
BSA	1390.301	1390.301	1390.301	1393.720	1393.720	1393.720	1398.105	1398.105	1398.105

**Table 2.** Ultrasonic velocities of 2-HP2STP -BSA complex solutions at diff. conc. and temperature.

Temp	25 °C			30 °C			35 °C		
	1,4-Dioxane	DMSO	DMF	1,4-Dioxane	DMSO	DMF	1,4-Dioxane	DMSO	DMF
1	1401.974	1385.806	1400.756	1409.559	1408.381	1409.943	1420.501	1416.003	1416.626
1.5	1401.365	1385.708	1401.365	1411.794	1410.559	1410.559	1420.754	1417.379	1418.003
2	1402.584	1398.148	1401.974	1410.559	1411.177	1411.794	1421.637	1418.626	1418.626
2.5	1403.805	1398.933	1402.756	1414.271	1412.413	1410.559	1424.266	1419.847	1421.172
3	1404.416	1399.148	1403.194	1416.135	1411.794	1412.413	1426.155	1421.127	1422.381
3.5	1406.933	1403.194	1404.416	1422.381	1413.032	1413.032	1431.855	1421.754	1423.637
BSA	1378.010	1378.010	1378.010	1408.148	1408.148	1408.148	1406.867	1406.867	1406.867

**Figure 9.** Scatchard plot of 4-HP2OTP-BSA complex in 1,4-dioxane, DMSO, DMF at 25 °C.**Figure 10.** Scatchard plot of 4-HP2OTP-BSA complex in 1,4-dioxane, DMSO, DMF at 30 °C.

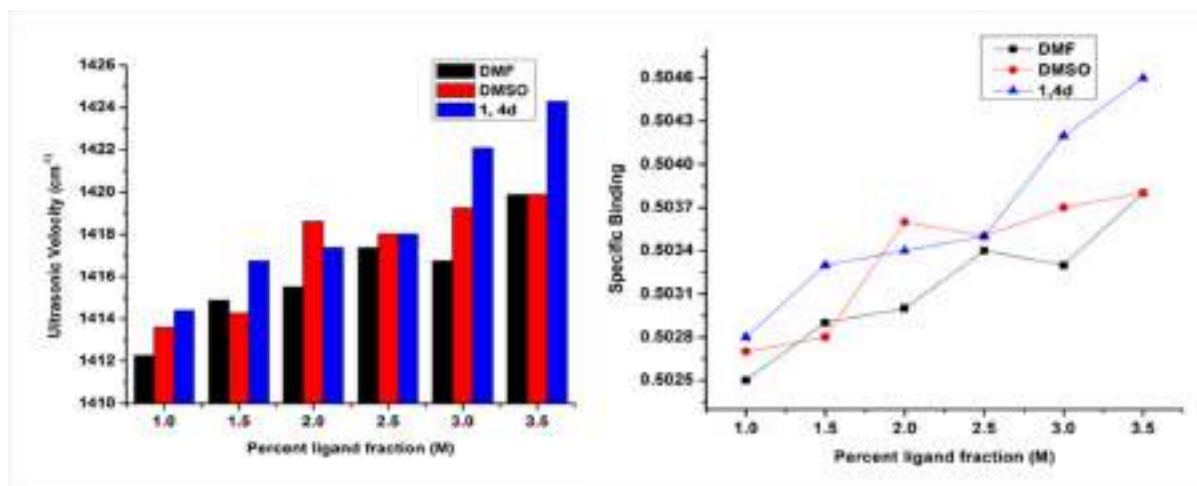


Figure 11. Scatchard plot of 4-HP2OTP-BSA complex in 1,4-dioxane, DMSO, DMF at 35 °C.

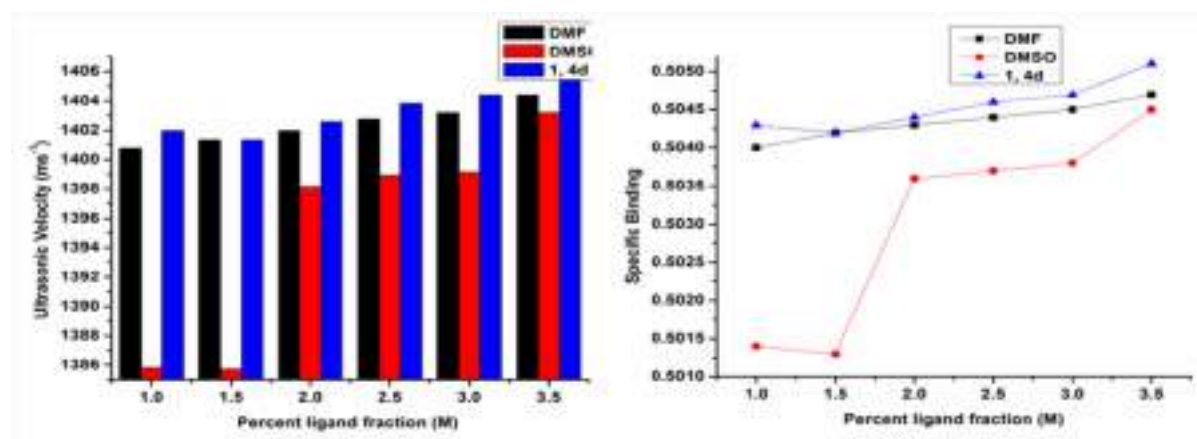


Figure 12. Scatchard plot of 2-HP2STP-BSA complex in 1,4-dioxane, DMSO, DMF at 25 °C.

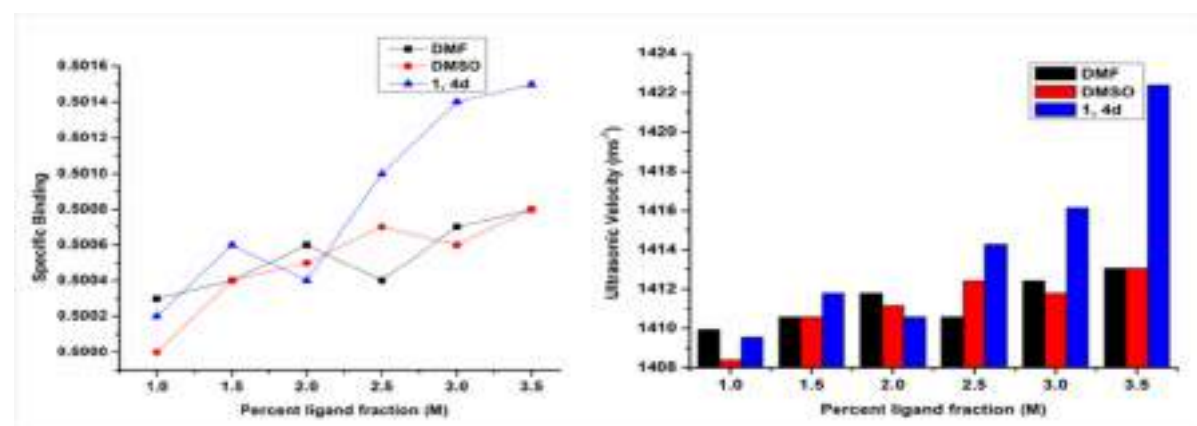


Figure 13. Scatchard plot of 2-HP2STP-BSA complex in 1,4-dioxane, DMSO, DMF at 30 °C.

### Thermodynamic study

In order to elucidate the interaction of ligands to the BSA, the thermodynamic parameters ( $\Delta G$ ,  $\Delta H$  and  $\Delta S$ ) have been calculated by using van't Hoff equation at the temperatures 298, 303 and

308 K. The enthalpy change is calculated from the slope of the van't Hoff relationship.

$$\ln k = -\frac{\Delta H}{RT} + \frac{\Delta S}{R} \quad (1)$$

Graph plotted between  $\ln k$  vs  $1/T$  shows

straight line with positive slope (Figure 15 and 16).

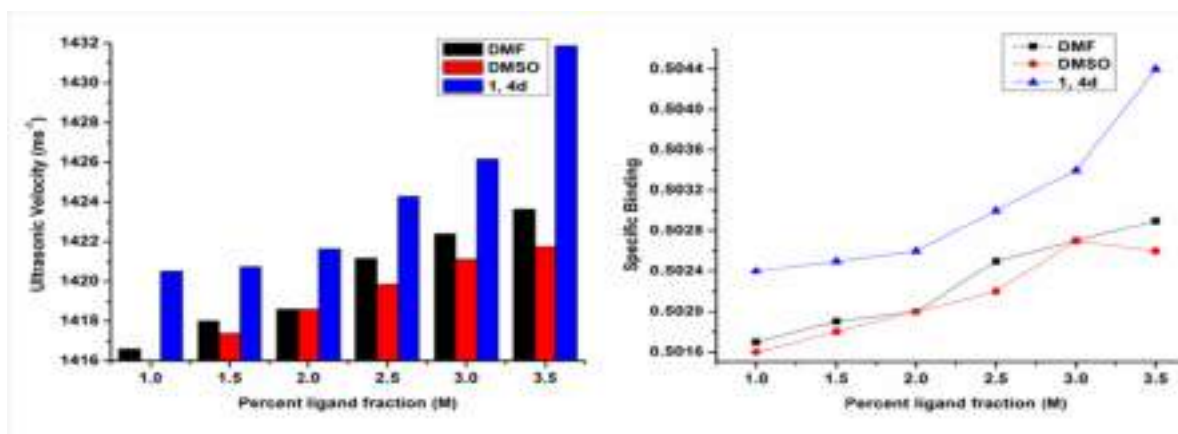


**Figure 14.** Scatchard plot of 2-HP2STP-BSA complex in 1,4-dioxane, DMSO, DMF at 35 °C.

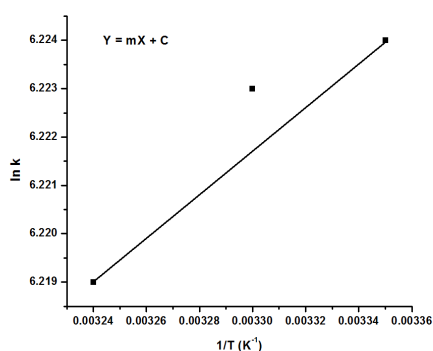


**Figure 15.** Graph of  $\ln k$  vs  $1/T$  in 1,4-dioxane for 4-HP2OTP-BSA complex.

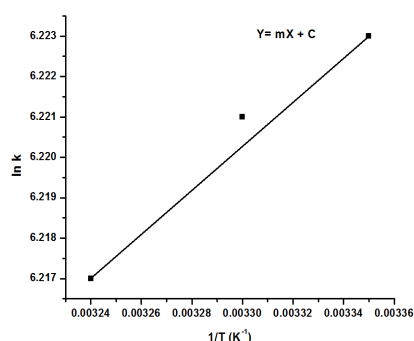


**Figure 16.** Graph of  $\ln k$  vs  $1/T$  in 1,4-dioxane for 2-HP2STP-BSA complex.

Positive values of  $\Delta H$  and  $\Delta S$  indicate that ligands interaction to BSA are enthalpy and entropic driven. Positive values of entropy indicate that there is unfolding of BSA. For unfolding, process must be endothermic which is indicated

by positive values of enthalpy and entropy (table 3 and 4). The specific electrostatic interaction is also characterized by the positive values of enthalpy and entropy. The negative value of  $\Delta G$  indicates that the ligands-BSA complexation is a spontaneous process. As the temperature increased the negative value of  $\Delta G$  is also increases, which concluded the ligands -BSA interaction is more feasible at high temperature. So, the hydrogen bonding, electrostatic and hydrophobic interactions are supposed to be possible factors contributing binding of the ligands to BSA. Slightly greater free energy values for 4-HP2OTP than 2-HP2STP is due to greater intermolecular hydrogen bonding of oxygen than Sulphur.

**Table 3.** Thermodynamic parameters at different temperature of 4-HP2OTP-BSA in 1,4-dioxane.

Sr. No.	Temp. (k)	$\Delta H$ J/mol	$\Delta G$ kJ/mol	$\Delta S$ J/mol
1	298 k	554.12	-14.343	49.99
2	303 k		-14.593	
3	308 k		-15.843	

**Table 4.** Thermodynamic parameters at different temperature of 2-HP2STP-BSA in 1,4-dioxane.

Sr. No.	Temp. (k)	$\Delta H$ J/mol	$\Delta G$ kJ/mol	$\Delta S$ J/mol
1	298 k	554.12	-14.313	49.89
2	303 k		-14.562	
3	308 k		-14.812	

### 3. Material and Methods

Dialysis membrane (molecular weight cut off 3500) used in the experiment purchased from Sigma Chemical Co. (USA). UV-VIS spectrophotometer (UV-1800, Shimadzu, Japan) and metabolic shaking incubator (REMI RS-24AC) used in the experiment. FT-IR measurements were taken at room temperature on a Bruker FT-IR spectrometer (Alpha model, Germany) equipped with Zn-Se attenuated total reflection (ATR) accessory. Multi-frequency ultrasonic interferometer (VI microsystem, Chennai, India), BSA (essential fatty acid free) purchased from Chemsworth Chemicals Ltd (India) and used without further purification. Basic buffer selected to maintain the physiological pH. For the synthesis, all the chemicals used are of A.R. grade of Merck India Limited and purchased from commercial suppliers. The purity of the synthesized compound was ascertain by thin layer chromatography on silica gel G in petroleum ether and ethyl acetate (7:3) mixture, melting point recorded using digital melting point apparatus Equiptronics (EQ 730).  $^1\text{H}$  NMR spectra of the compound recorded in  $\text{CDCl}_3$  on NMR instrument (500MHz) using TMS as an internal standard from

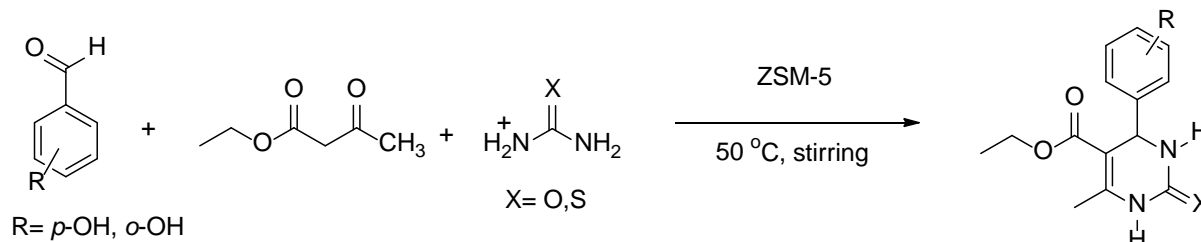
SAIF, CDRI Lucknow.

#### Optimization study

4-HP2OTP and 2-HP2STP are not completely soluble in buffer. Hence mixture of buffer with non-aqueous solvent such as 1,4-dioxane, DMF & DMSO used to dissolve 4-HP2OTP and 2-HP2STP. Different ratio of buffer: non-aqueous solvent tried, but the complete solubility of these drugs was obtained at optimum ratio 30:70:non-aqueous solvent:buffer.

#### Preparation of 4-HP2OTP and 2-HP2STP

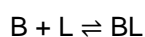
A one-pot synthesis of dihydropyrimidine derivatives has been carried out via Biginelli reaction using zeolite ZSM-5 as a catalyst under solvent free condition (Scheme 1). A mixture of aromatic aldehydes (4.71 mmol), ethylacetoacetate/(4.71 mmol), urea/thiourea (7.07 mmol) and catalyst zeolite ZSM-5 (10 wt%) in relation to the amount of aldehyde used was heated at  $50^\circ\text{C}$  for 10-25 min [21].



**Scheme 1.** Preparation of 4-HP2OTP and 2-HP2STP.

#### Measurements of binding affinity

For the Scatchard analysis, binding affinity of BSA and 4-HP2OTP and 2-HP2STP is expressed as an association constant or binding constant which is derived from the law of mass action. BSA (B) interacts with the ligands (L) i.e. 4-HP2OTP and 2-HP2STP to form the complex as given below.



$$\text{Hence, association constant } K_a = \frac{[\text{BL}]}{[\text{B}][\text{L}]}$$

Binding strength of the ligand to BSA is a measure of association constants.

#### Equilibrium dialysis

Different concentrations ( $1 \times 10^{-3}$  M to  $3.5 \times 10^{-3}$  M) of 4-HP2OTP and 2-HP2STP in 1,4-dioxane, DMSO, DMF (30:70:solvent:buffer) were prepared and mixed separately with  $0.15 \mu\text{M}$  BSA solution. These solutions were allowed to stand at room temperature for the maximum binding of ligands to BSA. From each mixture 3.5 ml solution was poured into previously prepared semi-permeable membrane and both the ends were sealed properly. The membrane tubes having 4-HP2OTP-BSA and 2-HP2STP-BSA complex solutions were immersed in a 100 ml conical flask

containing 40 ml buffer solution each. These conical flasks placed in a metabolic shaker for dialysis for 12 hrs at room temperature. After dialysis, absorbance's of bound fraction of 4-HP2OTP and 2-HP2STP to BSA were measured on a UV spectrophotometer ( $\lambda_{\max}$  520 nm).

### Effect of foreign particles

The binding study of 4-HP2OTP-BSA and 2-HP2STP-BSA is carried out in presence of foreign particles in 1,4-dioxane. 0.1M solution of arsenic and mercury salts were prepared and mixed with same solutions of ligands and BSA. These mixed complex solutions were kept some time to check the effect of foreign particles on binding.

### FT-IR spectroscopic study

Different concentrations of 4-HP2OTP and 2-HP2STP and the BSA as mentioned above mixed and allowed to stand at room temperature for maximum binding. FT-IR measurements were carried out at room temperature on FT-IR spectrometer equipped with Zn-Se attenuated total reflection (ATR) method. All spectra taken via the ATR method with a resolution of  $4\text{ cm}^{-1}$  and 60 scans in the region  $1800\text{-}1300\text{ cm}^{-1}$ . Absorbances of complexes were measured at room temperature.

### Ultrasonic study

Ultrasonic is a versatile non-destructive and highly investigatory technique. Ultrasonic absorption in a medium provides important tools for the evaluation of the structural, chemical and physical properties of the medium [22]. Initially ultrasonic interferometer set at 1MHz. Different concentrations of 4-HP2OTP and 2-HP2STP mixed with BSA and allowed to stand for some time to get maximum binding, ultrasonic velocities of these complex solutions were recorded at 298K. Similar steps were performed at 303K and 308K to determine ultrasonic velocities of the complexes. Specific binding and association constants are determined using Scatchard plot.

## 4. Conclusions

In the present study, the binding interaction of

4-HP2OTP and 2-HP2STP to BSA has been studied by equilibrium dialysis, FT-IR spectroscopy and acoustical study at physiological pH in various solvents. The scatchard analysis provided a non-linear curve on binding of ligands to the BSA, suggested the presence of at least two binding sites in BSA. The experimental result by equilibrium dialysis and acoustical study clearly indicate that 4-HP2OTP and 2-HP2STP interact to BSA by means of Vander Waal's interactions and hydrogen bonds in the hydrophobic packet of binding sites. It is also observed that binding affinity increases with increased in the concentrations and temperatures; this probably enhances the pharmacological activity of the drugs. FT-IR spectroscopy showed the binding mainly through amide I site by hydrophobic interaction, which changes the secondary structure of BSA. The greater binding is observed in 4-HP2OTP than 2-HP2STP due to greater intermolecular hydrogen bonding of oxygen than sulphur. Aprotic and non-polar nature of 1,4-dioxane supports the binding of 4-HP2OTP and 2-HP2STP to BSA than DMSO and DMF. The thermodynamic parameters also indicated that the hydrogen bonding, electrostatic and hydrophobic interactions induce alterations in secondary structure of the BSA.

## Supporting Information

[<sup>1</sup>H NMR, UV and IR spectra of 4-HP2OTP and 2-HP2STP.](#)

## References and Notes

- [1] Chuang, V. T. G.; Otagiri, M. *Drugs Today* **2007**, *43*, 547. [\[Crossref\]](#)
- [2] He, X. M.; Carter, D. C. *Nature* **1992**, *358*, 209. [\[Crossref\]](#)
- [3] Carter, D. C.; Ho, J. X. *Adv. Protein Chem.* **1994**, *45*, 153. [\[Crossref\]](#)
- [4] Michalcová, L.; Glatz, Z. *J. Sep. Sci.* **2015**, *38*, 325. [\[Crossref\]](#)
- [5] Shuai, Li.; Chen, Z.; Tan, Z. *Spectrosc. Lett.* **2013**, *46*, 211. [\[Crossref\]](#)
- [6] Hu, Y. J.; Ou-Yang, Y.; Zhang, Y.; Liu, Y. *Protein J.* **2010**, *29*, 234. [\[Crossref\]](#)
- [7] Paxton, J. W. *J. Pharmacol. Methods* **1981**, *5*, 203. [\[Crossref\]](#)
- [8] Ferraro, G.; Pica, A.; Krauss, I. R. *J. Biol. Inorg. Chem.* **2016**, *21*, 433. [\[Crossref\]](#)

- [9] Kaur, R.; Chaudhary, S.; Kumar, K.; Gupta, M. K.; Rawal, R. K. *Eur. J. Med. Chem.* **2017**, *132*, 108. [\[Crossref\]](#)
- [10] Vasconcelos, A.; Oliveira, P. S.; Ritter, M.; Freitag, R. A.; Romano, R. L. *J. Biochem. Mol. Toxicol.* **2012**, *26*, 155. [\[Crossref\]](#)
- [11] Atwal, K. S.; Swanson, B. N.; Unger, S. E.; Floyd, D. M. *J. Med. Chem.* **1991**, *34*, 806. [\[Link\]](#)
- [12] Najmeh, E.; Ahmad, R. M. *Drug Discovery Today* **2009**, *14*, 1058. [\[Crossref\]](#)
- [13] Gupta, Y. K.; Gupta, V.; Singh, S. *J. Pharm. Res. (Mohali, India)* **2013**, *7*, 491. [\[Crossref\]](#)
- [14] Wanke, R.; Harjivan, S. G.; Pereira, S. A.; Marques, M. M. *Int. J. Antimicrob. Agents* **2013**, *42*, 443. [\[Crossref\]](#)
- [15] Fielding, L.; Rutherford, S.; Fletcher, D. *Magn. Reson. Chem.* **2005**, *43*, 463. [\[Crossref\]](#)
- [16] Skinner, A. L.; Laurence, J. S. *J. Pharm. Sci. (Philadelphia, PA, U. S.)* **2008**, *97*, 4670. [\[Crossref\]](#)
- [17] Xiangrong, L.; Gongke, W.; Dejun, C.; Yan, L. *Mol. BioSyst.* **2014**, *10*, 326. [\[Crossref\]](#)
- [18] Chaturvedi, S.; Ahmad, E.; Khan, J. M.; Alam, P.; Khan, R. H. *Mol. BioSyst.* **2015**, *11*, 307. [\[Crossref\]](#)
- [19] Baroni, S.; Mattu, M.; Aime, S.; Fasano, M. *The FEBS Journal* **2001**, *268*, 6214. [\[Crossref\]](#)
- [20] Tian, J.; Liu, J.; Chen, X. *Bioorg. Med. Chem.* **2005**, *13*, 4124. [\[Crossref\]](#)
- [21] Bajaj, S. D.; Mahodaya, O. A.; Tekade, P. V. *Pharm. Chem. J.* **2015**, *48*, 681. [\[Crossref\]](#)
- [22] Khan, I. *Thermochim. Acta* **2009**, *483*, 45. [\[Crossref\]](#)



**IN VITRO BINDING STUDY OF 4HDDD TO BSA AT PHYSIOLOGICAL PH:  
ACOUSTICAL AND THERMODYNAMIC STUDY**

**Ajay Pisudde<sup>1</sup>, Pradip Tekade\*<sup>1</sup>, Shrikant Thakare<sup>1</sup>, Pravin Bodkhe<sup>2</sup>, Sandip Petare<sup>3</sup>**

<sup>1</sup>*Department of Chemistry, Jankidevi Bajaj College of Science, Jamnalal Bajaj marg, Civil lines, Wardha (India).*

<sup>2</sup>*Department of Chemistry, Vidyabharti Mahavidyalaya, Amravati, M.S., India 444602.*

<sup>3</sup>*Department of Biotechnology, New Arts Commerce and Science College Wardha, Maharashtra, India 442001.*

*Email: [pradiptekade@gmail.com](mailto:pradiptekade@gmail.com), [pisuddeajay@gmail.com](mailto:pisuddeajay@gmail.com), [shrikantthakare@gmail.com](mailto:shrikantthakare@gmail.com), [pravinbodkhe13@gmail.com](mailto:pravinbodkhe13@gmail.com), [sandypetare@gmail.com](mailto:sandypetare@gmail.com)*

**ABSTRACT:**

The present study showed the binding interaction of diethyl-4-(4-hydroxyphenyl)-2, 6-dimethyl-1, 4-dihydropyridine-3, 5-dicarboxylate in 1, 4-dioxane, DMSO and DMF to the bovine serum albumin (BSA) by acoustical study at physiological pH and its molecular modeling. Findings were interpreted by scatchard plot which showed an increase in association constants with increasing temperature and concentration. Binding supposed to be more in 1, 4-dioxane than DMSO and DMF, which may be due to aprotic and non-polar nature 1, 4-dioxane. The free energy ( $\Delta G$ ), enthalpy ( $\Delta H$ ) and entropy ( $\Delta S$ ) values were calculated from van't Hoff equation. The negative  $\Delta G$  showed the spontaneous process and positive values of  $\Delta H$  and  $\Delta S$  showed endothermic interaction between drug and BSA.  $\Delta G$  becomes more negative with increase in temperature, indicated feasibility of binding interaction at high temperature. The positive value of  $\Delta H$  and  $\Delta S$  also showed specific electrostatic and hydrophobic interaction of drug and BSA. Molecular modeling confirmed the binding interaction showing energy -217.66 kJ/mol, which concluded the stable complex formation between drug and BSA.

**KEYWORDS:** Acoustical study, molecular modeling, Scatchard analysis, association constants, BSA.

**1. INTRODUCTION:**

Human serum albumin (HSA) is the most abundant protein in blood serum with the concentration of 0.63 mM. It is single polypeptide chain of 585 amino acids with a large helical triple domain structure that forms heart shaped molecule. HSA binds a relatively a number of insoluble endogenous drugs such as fatty acids, billirubin, etc. and it facilitates their transport to target tissues. Human serum albumin shows various pharmacological importances, because of its broad interactions and abundance. The structure of HSA explains numerous physiological phenomena and provides further insight in pharmacokinetics<sup>1</sup>. A

variation in temperature is found to be a key factor in binding affinities of HSA<sup>ii</sup>, as evident from the drugs Ligustrazine<sup>iii</sup>, Ciprofloxacin<sup>iv</sup>, methotrexate<sup>v</sup> and cisplatin<sup>vi</sup>. 1, 4-dihydropyridine derivatives shows a wide range of biological activities and medicinal properties<sup>vii,viii</sup>. Diethyl -4-(4-hydroxyphenyl) -2, 6- dimethyl-1, 4-dihydropyridine-3, 5-dicarboxylate (4HDDD) is one of the pyridine derivatives showing antimicrobial and anticonvulsant activities<sup>ix</sup>. A drug binding influences the metabolic activity of target tissues so the binding interactions between drugs and plasma protein are important to understand the pharmacokinetics and pharmacodynamics. Functional and physiological properties of these proteins extensively studied over decades<sup>x</sup>. In BSA varying binding sites are available for ligands<sup>xi, xii</sup>. Various techniques are available to monitor the binding interactions of ligands to protein like NMR<sup>xiii</sup>, isothermal titration calorimetry<sup>xiv</sup>, U.V. visible absorbance<sup>xv</sup>, fluorescence<sup>xvi</sup>, equilibrium and FT-IR<sup>xvii</sup> and CD spectroscopy<sup>xviii</sup>. Molecular modeling also shows important aspects about protein-drug interaction<sup>xix, xx,xxi</sup>. It is difficult to obtain HSA for experimental purposes. As HSA and BSA exhibit similar chemical properties, BSA in lieu of HSA was used in this study because of low cost and easy availability. In the view of above considerations, present study demonstrate the effect of drug concentrations, different temperatures and polar/non polar solvent on binding interaction of 4HDDD to BSA at physiological pH by acoustical properties along with thermodynamic parameters like free energy, enthalpy, entropy and molecular modeling study.

## 2. EXPERIMENTAL:

**Materials and Methods:** Ultrasonic interferometer (VI Microsystems, Chennai, India). BSA procured from Chemsworth Chemicals Ltd (India), drug 4HDDD, software HEX 8.0, basic buffer (7.4). For the synthesis, all the reagents used were of A.R. grade purchased from Merck India Limited.

### **Optimization study:**

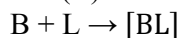
4HDDD was insoluble in basic buffer at physiological pH. Hence mixture of buffer with non aqueous solvent such as 1, 4-dioxane, DMF and DMSO were used to dissolve 4HDDD. Different ratio of buffer: non-aqueous solvents were tried, but the complete solubility of 4HDDD was obtained at optimum ratio 30: 70:: non-aqueous solvent: buffer.

### **Preparation of 4HDDD:**

Diethyl-4-(4-hydroxyphenyl)-2, 6-dimethyl-1, 4-dihydropyridine-3, 5-dicarboxylate (4HDDD) synthesized by known method<sup>xxii</sup>. The purity of the synthesized compound was ascertain by thin layer chromatography on silica gel G in petroleum ether and ethyl acetate (7:3) mixture, Melting point recorded using digital melting point apparatus Equiptronics (EQ 730). <sup>1</sup>H NMR spectrum of the compound recorded in CDCl<sub>3</sub> on NMR instrument (500MHz) using TMS as an internal standard from SAIF, CDRI Lucknow, India. UV spectra recorded on BioEra's spectrophotometer and FT-IR spectra on Brukers alpha at Jankidevi Bajaj college of science wardha, MS., India.

### **Measurement of binding affinity:**

For the Scatchard analysis, binding affinity of BSA and 4HDDD is expressed as an equilibrium constant or association constant which is derived from the law of mass action. BSA (B) interacts with the 4HDDD (L) to form the complex is given as



Hence, association constant  $K_a = \frac{[BL]}{[BL]+[B]}$

Binding strength of the ligand to BSA is a measure of association constants.

### **Ultrasonic study**

Ultrasonic is a versatile non-destructive and highly investigatory technique. Ultrasonic absorption in a medium provides important tools for evaluation of the structural, chemical and physical properties of medium<sup>xxiii</sup>. Initially ultrasonic interferometer set at 1MHz. Different concentrations ( $1 \times 10^{-3}$  to  $3.5 \times 10^{-3}$  M) of 4-HDDD in different solvents (1, 4-dioxane, DMSO, DMF (30:70:: solvent: buffer) were prepared at physiological pH. 0.15 $\mu$ M BSA also prepared at same pH and its ultrasonic velocity was measured. Different concentrations of 4HDDD mixed with BSA at 298K and allowed to stand for 1 hr for maximum binding. The ultrasonic velocities of complex solutions were recorded. Similar steps were performed at 303 and 308K and specific binding along with association constants were determined using Scatchard plot.

#### **Molecular modeling study**

Molecular modeling of BSA with 4HDDD was carried out on Hex 8.0 software. This gives value of an efficient energy. PDB file of the crystal structure of BSA obtained from the RCSB data bank having ID 4F5S and 3D structure for 4HDDD was developed. Initially, the structure of 4HDDD has been drawn using Chem Draw and its 3D structure is developed. The obtained 3D structure arranged in a minimized energy form. The PDB files runs on Hex 8.0 which gave the energy value of the newly formed complex showing its stability.

### **3. RESULT AND DISCUSSION:**

#### **Ultrasonic study:**

In present study, ultrasonic velocities of 0.15  $\mu$ M BSA in 1, 4- dioxane was measured at temperature 298, 303 and 308K. The ultrasonic velocities are 1496.899, 1503.163 and 1505.189 m/s respectively. Ultrasonic velocity of 4HDDD-BSA complex was also measured at varying concentrations and temperatures (Table 1). The scatchard graph is plotted for specific binding versus percent ligand fraction and from this plot binding parameters of 4HDDD to BSA have been determined. The Scatchard analysis gives different association constants at different temperatures. The association constants in 1, 4-dioxane are 0.5011 ( $\pm 0.0005$ ), 0.5018 ( $\pm 0.0005$ ) and 0.5027 ( $\pm 0.0005$ ) at temperature 298, 303 and 308K respectively. Similar analyses were also carried out in DMSO and DMF and association constants have been calculated. The association constants in DMSO and DMF are 0.5011 ( $\pm 0.0005$ ), 0.5008 ( $\pm 0.0005$ ), 0.5007 ( $\pm 0.0005$ ) and 0.5006 ( $\pm 0.0005$ ), 0.5007 ( $\pm 0.0005$ ), 0.5008 ( $\pm 0.0005$ ) at temperature 298, 303 and 308 K respectively. The association constants for 4HDDD-BSA binding increases as the temperature increases. This increase association constants clearly indicates the exothermic nature of reaction. This supports the interaction of 4HDDD with BSA by means of van der Waals interactions and hydrogen bonds in the hydrophobic packet of binding sites. It is also observed that the binding affinity increases with increase in concentration of the drug; this probably enhances the pharmacological activity of the drug. The scatchard plot given below represents binding affinities of 4HDDD with BSA at different temperatures. Figures 1 to 3 shows the Scatchard plots of BSA-4HDDD binding in 1, 4-dioxane, DMSO and DMF respectively. The effect of temperature on BSA-4HDDD binding is summarized in van't Hoff equation.

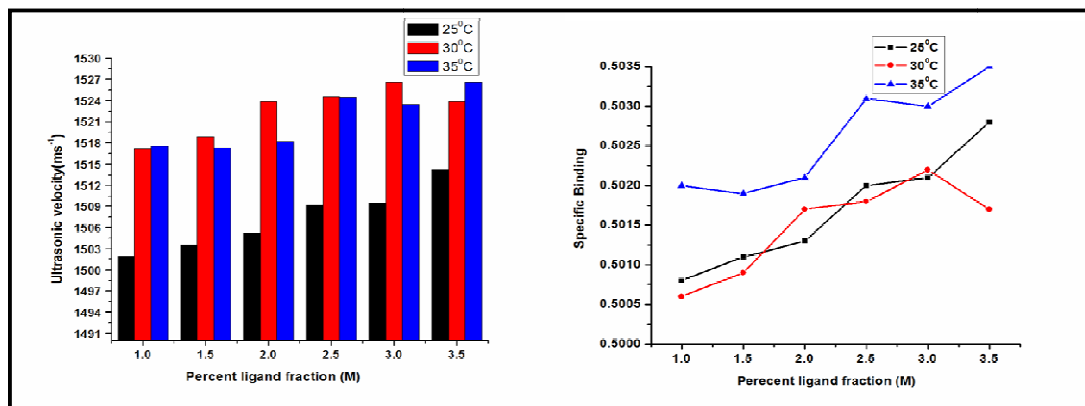


Figure 1: Graph of ultrasonic velocities and specific binding vs. conc. of 4HDDD in 1, 4-dioxane.

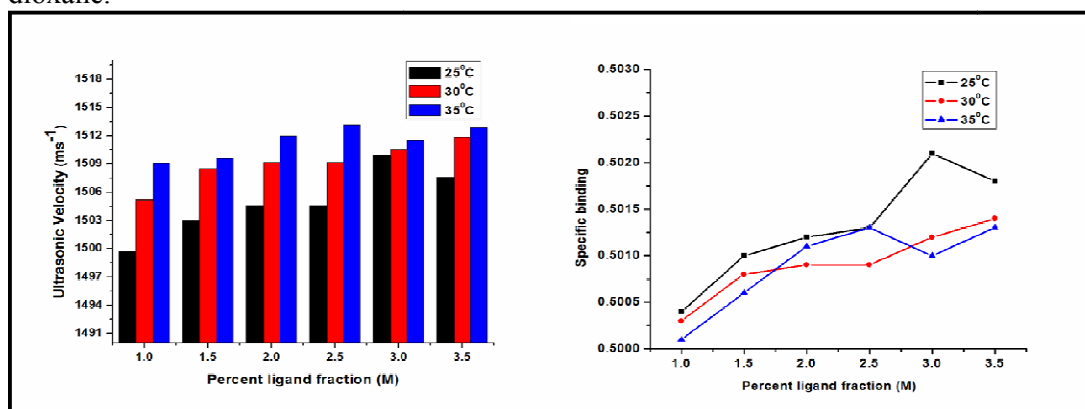


Figure 2: Graph of ultrasonic velocities and specific binding vs. conc. of 4HDDD in DMSO.

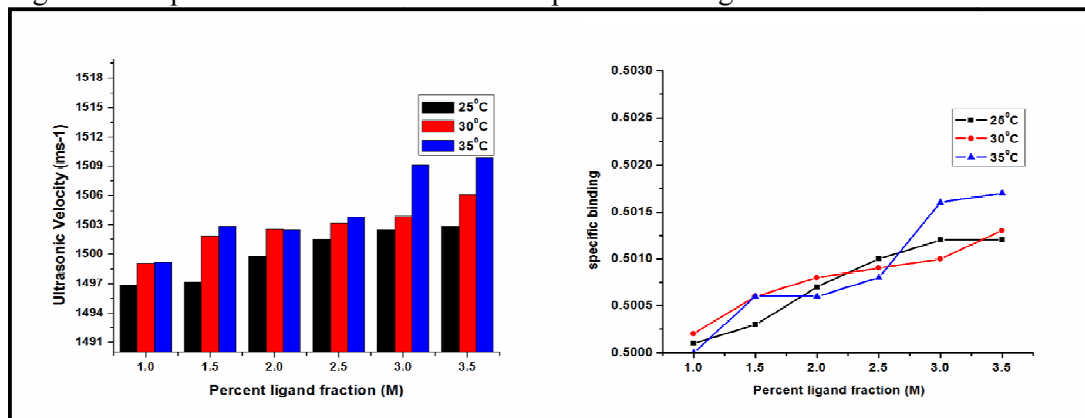


Figure 3: Graph of ultrasonic velocities and specific binding vs. conc. of 4HDDD in DMF.

Table 1: Ultrasonic velocities of 4HDDD-BSA complexes at different conc. and temperatures

Tem p Con c.	1,4 Dioxane			DMSO			DMF		
	25°C	30°C	35°C	25°C	30°C	35°C	25°C	30°C	35°C
1	1496.89	1499.0	1499.1	1499.6	1505.1	1506.0	1501.9	1517.1	1517.56
4	83	87	96	89	91	21	67	6	
1.5	1497.17	1501.8	1502.8	1502.9	1508.5	1509.6	1503.5	1518.8	1517.27

	3	76	60	59	29	14	66	60	7
2	1499.85 0	1502.5 76	1502.5 59	1504.6 14	1509.1 89	1511.9 59	1505.2 77	1523.8 60	1518.21 1
2.5	1501.49 9	1503.2 77	1503.8 35	1504.6 14	1509.1 89	1513.1 63	1509.2 11	1524.5 34	1524.50 3
3	1502.52 9	1503.8 76	1509.1 67	1509.9 59	1510.5 12	1511.5 19	1509.5 03	1526.5 59	1523.50 3
3.5	1502.87 0	1506.0 85	1509.8 76	1507.5 94	1511.8 36	1512.8 76	1514.1 91	1523.8 60	1526.53 4
BSA	1495.22 9	1497.6 97	1499.0 85	1496.8 99	1503.2 69	1505.1 89	1496.8 99	1503.1 63	1517.56 6

### Thermodynamic study

In order to elucidate the interaction of 4HDDD with the BSA, the thermodynamic parameters ( $\Delta G$ ,  $\Delta H$  and  $\Delta S$ ) have been calculated from van't Hoff equation at the temperatures 298, 303 and 308 K. The enthalpy change is calculated from the slope of the van't Hoff relationship.

$$\ln k = -\frac{\Delta H}{RT} + \frac{\Delta S}{R} \quad \text{————— (1)}$$

Graph plotted between  $\ln k$  vs  $1/T$  shows straight line with positive slope (figure 4).

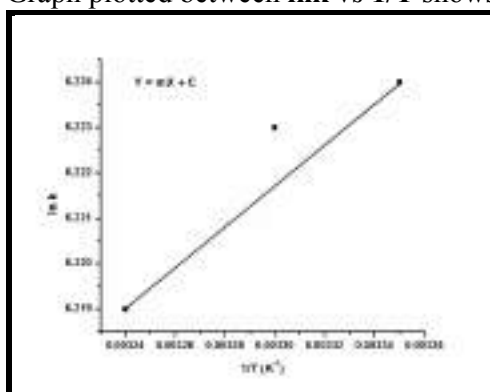


Figure 4: Graph of  $\ln k$  vs  $1/T$  in 1,4-dioxane

Table 2: Thermodynamic parameters at different temperature in 1, 4-dioxane.

Sr. No.	Temp. (k)	$\Delta H$ J/mol	$\Delta G$ kJ/mol	$\Delta S$ J/mol
1	298 k	332	-14.735	50.56
2	303 k		-14.988	
3	308 k		-15.240	

Positive values of  $\Delta H$  and  $\Delta S$  indicates that drug interaction with BSA are enthalpy and entropic driven. Positive value of entropy indicates that there is unfolding of BSA. For unfolding, process must be endothermic which is indicated by positive values of enthalpy and entropy (table 2). The specific electrostatic interaction is also characterized by the positive values of enthalpy and entropy. The negative value of  $\Delta G$  indicates that the 4HDDD-BSA complexation is a spontaneous process. As the temperature increases the negative value of  $\Delta G$  is also increases, which concluded the 4HDDD-BSA interaction is more feasible at high temperature. So, the hydrogen bonding, electrostatic and hydrophobic interactions are supposed to be possible factors contributing binding of 4HDDD to BSA. The thermodynamic parameters in DMSO and DMF are found to be close but not significant with respect to 1, 4 dioxane.

### **Molecular modeling study**

Molecular modeling is also an efficient method for measurement of interaction between protein and drug. The binding interaction between BSA and 4HDDD was also studied by molecular modeling. The obtained energy is a measure of binding of 4HDDD to BSA. The energy obtained is -217.66 kJ/mol, shows an efficient binding of 4HDDD with BSA. Diagrammatic representation of interaction between BSA and 4HDDD is as shown in figure 5.

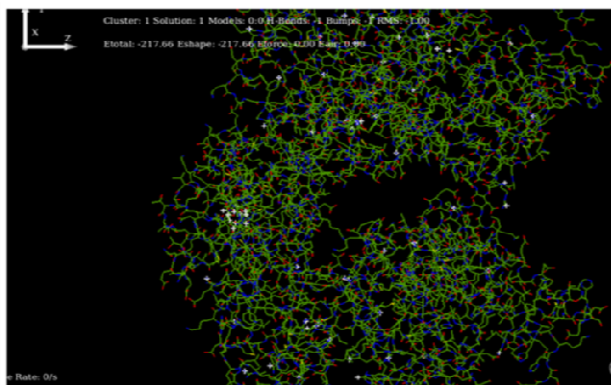


Figure 5: Molecular modeling interaction between BSA and 4HDDD.

### **4. CONCLUSION:**

Current investigation was an attempt to study the interaction of diethyl-4-(4-hydroxyphenyl)-2, 6-dimethyl-1, 4-dihydropyridine-3, 5-dicarboxylate in 1, 4-dioxane, DMSO and DMF to BSA by acoustical method at physiological pH and molecular modeling. It is found that binding is more significant in 1, 4-dioxane as compared to DMSO and DMF. It may be due to aprotic and non polar nature of the 1, 4-dioxane. The scatchard plot at all temperatures found to be a non-linear indicating the presence of at least two binding sites on BSA. The values of thermodynamic parameters indicate that hydrogen bonding, electrostatic and hydrophobic interactions induce alterations in secondary structure of the BSA. Molecular docking also supports the binding having energy -217.66 kJ/mol, concluding the stable binding of 4HDDD with BSA.

### **5. ACKNOWLEDGEMENT:**

We thanks to department of chemistry, Jankidevi Bajaj College of science for providing necessary research facilities. No funding was received for this study.

### **REFERENCES:**

- i. M.X. He, C.D. Carter, Nature, 358, 209(1992). **DOI:** 10.1038/358209a0
- ii. M. Lenka, Journal of separation science, 38(2), (325)2015. **DOI:** 10.1002/jssc.201400914
- iii. Li. Shuai, Z. Chen, Z. Tan, Spectroscopic letters, 46, 211(2013). **DOI:** 10.1080/00387010.2012.702292
- iv. Y.J. Hu, Y.O. Yang, Y. Zhang and Y. Liu, Protein J., 29, 234(2010). **DOI:** 10.1007/s10930-010-9244-6
- v. J. Paxton, Journal of Pharmacological Methods, 5(3), 203(1981). **DOI:** 10.1016/0160-5402(81)90088-7
- vi. G. Ferraro, A. Pica and I.R. Krauss, Journal of Biological Inorganic Chemistry, 21(4), 433(2016). **DOI:** 10.1007/s00775-016-1352-0

- vii. M. Nikoorazm, *Scientia Iranica*, 20(3), 603(2013). **DOI:** [10.1016/j.scient.2012.11.008](https://doi.org/10.1016/j.scient.2012.11.008)
- viii. P. Mehta, P. Verma, *Journal of Chemistry*, 2013, 4 pages(2013), **DOI:** [10.1155/2013/865128](https://doi.org/10.1155/2013/865128)
- ix. H.S. Sohal, M. Kaur, R. Khare and K. Singh, *American Journal of Organic Chemistry*, 4(2), 21(2014). **DOI:** [10.5923/j.ajoc.20140402.01](https://doi.org/10.5923/j.ajoc.20140402.01)
- x. A. Gaudio, A. Korolkovas, Y. Takahata, *J. Pharm. Sci.*, 83(8), 1110(1994). **DOI:** [10.1002/jps.2600830809](https://doi.org/10.1002/jps.2600830809)
- xi. R. Wanke, S.G. Harjivan, S.A. Pereira and M.M. Marques, *International journal of antimicrobial agents*, 42(5), 443(2013). **DOI:** [10.1016/j.ijantimicag.2013.06.023](https://doi.org/10.1016/j.ijantimicag.2013.06.023)
- xii. L. Fielding, S. Rutherford, D. Fletcher, *Magnetic resonance in Chemistry*, 43(6), 463 (2005). **DOI:** [10.1002/mrc.1574](https://doi.org/10.1002/mrc.1574)
- xiii. A.L. Skinner, J.S. Laurence, *J. Pharm. Sci.*, 97(11), 4670(2008). **DOI:** [10.1002/jps.21378](https://doi.org/10.1002/jps.21378)
- xiv. L. Xiangrong, W. Gongke, C. Dejun and L. Yan, *Mol. BioSystem.*, 10, 326 (2014). **DOI:** [10.1039/C3MB70373H](https://doi.org/10.1039/C3MB70373H)
- xv. S. Chaturvedi, E. Ahmad, J.M. Khan, P. Alam, R.H. Khan, *Mol. Biosystem.*, 11, 307 (2015). **DOI:** [10.1039/C4MB00548A](https://doi.org/10.1039/C4MB00548A)
- xvi. S. Baroni, M. Mattu, S. Aime and M. Fasano, *Eur. J. Biochem.*, 268, 6214 (2001). **DOI:** [10.1046/j.0014-2956.2001.02569.x](https://doi.org/10.1046/j.0014-2956.2001.02569.x)
- xvii. A.M. Pisudde, P.V. Tekade, S.D. Bajaj and S.B. Thakare, *Heterocyclic Letters*, 6(4), 679(2016).
- xviii. J. Tian, J. Liu, X. Chen, *FEBS Letters*, 347, 995(2005). **DOI:** [10.1016/j.bmc.2005.02.065](https://doi.org/10.1016/j.bmc.2005.02.065)
- xix. M. Hartshorn, *J. Med. Chem.*, 50, 726(2007). **DOI:** [10.1021/jm061277y](https://doi.org/10.1021/jm061277y)
- xx. M. Taufer, *Concurr. Comput.*, 17, 1627(2005). **DOI:** [10.1002/cpe.949](https://doi.org/10.1002/cpe.949)
- xxi. S. Sousa, *Comb. Chem. High throughput Screen*, 13, 442(2010).
- xxii. S.D. Bajaj, O.A. Mahodaya, P.V. Tekade, and V.B. Patil, *Russian journal of general chemistry*, 87(3), 546(2017). **DOI:** [10.1134/S1070363217030264](https://doi.org/10.1134/S1070363217030264)
- xxiii. I. Khan, *Thermochimica Acta*, 483(1), 45(2009). **DOI:** [org/10.1016/j.tca.2008.10.023](https://doi.org/10.1016/j.tca.2008.10.023)

Received on February 1, 2018.



Tree Physiology 38, 52–65  
doi:10.1093/treephys/tpx117



## Research paper

# Carbon allocation and partitioning in *Populus tremuloides* are modulated by ectomycorrhizal fungi under phosphorus limitation

Shalaka Shinde<sup>1,2</sup>, Dhiraj Naik<sup>1,3</sup> and Jonathan R. Cumming<sup>1,4</sup>

<sup>1</sup>Department of Biology, 53 Camps Drive, West Virginia University, Morgantown, WV 26506, USA; <sup>2</sup>Present address: Biosciences Division, Argonne National Laboratory, Argonne, IL 60439, USA; <sup>3</sup>Present address: Department of Botany, Jankidevi Bajaj College of Science, Jankidevi Bajaj Marg, Wardha 442001, Maharashtra, India; <sup>4</sup>Corresponding author (jcumming@wvu.edu)

Received March 7, 2017; accepted August 30, 2017; published online October 3, 2017; handling Editor Torgny Näsholm

The fate of carbon (C) captured by forest trees during photosynthesis is influenced by the supply of other resources. Fixed C may be partitioned among biomolecules within the leaf and/or allocated throughout the tree to growth, storage and maintenance activities. Phosphorus (P) availability often limits tree productivity due to its high biological demand and strong interactions with soil minerals. As ectomycorrhizal (ECM) fungi play critical roles in enhancing phosphate (P<sub>i</sub>) acquisition by their hosts, these symbioses will influence the fate of C within trees and forested ecosystems. Using *Populus tremuloides* Michx. (trembling aspen) in symbiosis with *Laccaria bicolor* (Marie) P.D. Orton or *Paxillus involutus* (Batsch) Fr., we assessed C acquisition, allocation and partitioning under P<sub>i</sub> limitation, specifically focusing on primary and secondary C compounds. Both ECM fungi moderated the effects of low P on photosynthesis and C partitioning among carbohydrates and secondary metabolites by sustaining P<sub>i</sub> uptake and translocation in *P. tremuloides* under P<sub>i</sub> limitation. As leaf P declined, reductions in photosynthesis were accompanied by significant shifts in C partitioning from nonstructural carbohydrates (NSCs) to phenolic glycosides and tannins. Carbon partitioning in roots exhibited more complex patterns, with distinct increases in NSCs in nonmycorrhizal (NM) plants under P<sub>i</sub> limitation that were not evident in plants colonized by either ECM symbiont. In general, aspen colonized by *L. bicolor* exhibited C partitioning patterns intermediate between those of NM and *P. involutus* aspen. The C cost of symbiosis was pronounced for plants supporting *P. involutus*, where ECM plants exhibited maintenance of photosynthesis yet reduced biomass in comparison with NM and *L. bicolor* aspen under P<sub>i</sub> replete conditions. Our results indicate that the ECM symbiosis affects the disposition of C in forest trees in part by altering the acquisition of other limiting resources from soils, but also through ECM species-specific influences on host physiology. This modulation of C partitioning will have broad implications for forest ecosystem C capture, storage and cycling where nutrient resources may be limited.

**Keywords:** aspen, carbohydrates, *Laccaria bicolor*, *Paxillus involutus*, phenolic glycosides, stress physiology.

## Introduction

Forest ecosystem productivity is often limited by mineral nutrient availability (LeBauer and Treseder 2008, St Clair et al. 2008, Hou et al. 2012). Phosphorus (P) is a major mineral nutrient required by forest trees in significant amounts (Elser et al. 2007), yet P availability is limited in soils due to high biological demand and the chemical binding of inorganic phosphate (P<sub>i</sub>) and organic phosphorus (P<sub>o</sub>) sources to aluminum, iron (Fe)

and/or calcium (Ca) ions/compounds prevalent in many natural soils (von Uexküll and Mutert 1995, Batjes 1997).

To overcome P<sub>i</sub> limitation, plants have developed a suite of phosphate starvation responses (PSR) that moderate internal P homeostasis, maximize P acquisition from the environment and acclimate plants to low P environments (Vance et al. 1995, Raghothama and Karthikeyan 2005, Plaxton and Tran 2011, Zhang et al. 2014). Increases in the root-to-shoot ratio and changes in root architecture

increase soil exploration and P acquisition (Lynch 2011). Root exudation, increased  $P_i$  uptake capacity and metabolic pathway changes increase P acquisition from soils and P-use efficiency within the plant (López-Arredondo et al. 2014).

In addition to PSR systems, plant–mycorrhizal symbioses significantly alter plant–soil interactions and enhance P uptake (Plassard and Dell 2010). The colonization of roots by ectomycorrhizal (ECM) fungi alters root architecture, and hyphal ramification of the soil increases the volume of soil exploited for mineral uptake by the host plant (Hetrick 1991, Schack-Kirchner et al. 2000, Agerer 2001, Hagerberg et al. 2003). Ectomycorrhizal fungal uptake systems often have higher affinity for  $P_i$ , increasing  $P_i$  acquisition from the soil solution (Cumming 1996, Colpaert et al. 1999, Desai et al. 2014). Increased carbon (C) inputs to the soil in the form of exudates and enzymes may alter the chemistry of the rhizosphere and the subsequent availability of P from a broad spectrum of P-containing compounds for ECM fungi and root uptake (Cumming 1993, Leyval and Berthelin 1993, Wallander 2000, Casarin et al. 2004, Liu et al. 2008, Courty et al. 2010).

Depending on the effectiveness of nutrient limitation responses and mycorrhizal nutrient scavenging, photosynthesis, biochemical pathways and plant tissue composition may change when nutrient resources are limiting (Keski-Saari and Julkunen-Tiitto 2003, Hale et al. 2005, Donaldson et al. 2006, Baum et al. 2009). The production of C-based secondary compounds (CBSCs) in plants depends on the balance between C and nutrient availability (Bryant et al. 1983). In leaves of *Populus alba* × *P. grandidentata*, for example, the concentrations of tannins and salicylates were elevated under low nitrogen (N) (Kleiner et al. 1998). Indeed, many plant species accumulate anthocyanins and other phenolic compounds under nutrient limitation, indicating that CBSCs may also contribute to the acclimation of plants to stressful environments (Dixon and Paiva 1995, Donaldson et al. 2006, Chen et al. 2009).

Although plant responses involving CBSCs under environmental stress are well studied (Koricheva et al. 1998, Gayler et al. 2008, Caretto et al. 2015), considerably less is known about changes in secondary C metabolism in plants in the ECM association. In the *Larix decidua*–*Suillus tridentinus* symbiosis, higher levels of major secondary C-containing compounds were observed in the root apices of young mycorrhizas (Weiss et al. 1997) and concentrations of CBSCs in the foliage of *Salix* spp. depended on fungal partner and host species (Baum et al. 2009). However, little is known of the interactions between nutrient limitation and ECM fungi on the accumulation of CBSCs in plants.

In the current study, we assessed the influences of *Laccaria bicolor* and *Paxillus involutus* colonization on  $P_i$  limitation responses of *Populus tremuloides* (trembling aspen), specifically investigating photosynthesis and partitioning of C between carbohydrates and secondary metabolites. Trembling aspen is widely distributed across North America and fills both early and late successional niches. The root microbiome is diverse, including a wide

variety of ectomycorrhizal associates (Kaldorf et al. 2004, Fox et al. 2013, Bonito et al. 2016). *Laccaria bicolor* and *P. involutus*, common ECM symbionts of poplars that have been used extensively in tree physiology research, were used in this study because of this knowledge base as well as their known divergence in affecting  $P_i$  acquisition in their hosts (Cumming 1996).

We hypothesized that: (i) photosynthesis would be reduced due to  $P_i$  limitation, but increased in ECM plants in response to stimulated C demand in the root system by the fungal partners; (ii) nonmycorrhizal aspen would allocate more C to secondary compounds than to the production of plant biomass under  $P_i$  limitation; (iii) changes in photosynthesis, partitioning and growth would be more pronounced in nonmycorrhizal plants than in plants colonized by *L. bicolor* and *P. involutus* due to enhanced  $P_i$  acquisition by these symbionts; and (iv) differences between ECM symbionts would reflect fungal-specific changes in  $P_i$  acquisition or C demand induced by each symbiont.

## Materials and methods

### Fungal inoculation and plant culture

The *L. bicolor* (Marie) P.D. Orton fungal strain S238N (Institut National de la Recherche Agronomique, Nancy, France) and *P. involutus* (Batsch) Fr. fungal strain ATCC 200,175 (American Type Culture Collection) were used as symbionts to colonize seedlings of *P. tremuloides* Michx. (trembling aspen, ‘aspen’) (seed source from the Canadian Natural Resources, National Tree Seed Center, Fredericton NB, Canada). Fungal cultures were maintained on a modification of modified Melin Norkrans (MMN) agar medium (Cumming et al. 2001). For inoculum production, cultures were grown aseptically in liquid MMN medium for 3 weeks at 25 °C in the dark in static culture. Cultures were macerated by blending briefly (three pulses for 3 s each in a common blender) to produce fungal mycelial slurries to serve as inoculum (Molina et al. 1982).

The experimental system for the production of ECM aspen consisted of CP512 treepots (Stuewe and Sons, Corvallis, OR, USA) each containing ~5 l of a mixture (2:1) of sterile acid-washed sand and vermiculite. For establishing mycorrhizal seedlings, aliquots of fungal slurry (equal to ~0.2 g dry weight fungal tissue) were added ~2 cm below the surface of the sand (Desai et al. 2014). For nonmycorrhizal (NM) plants, only MMN liquid medium was added instead of fungal slurry.

Seeds of *P. tremuloides* were planted ~0.5 cm deep in the pots and were kept moist by watering four-times daily with d. H<sub>2</sub>O. Seedlings were thinned to one seedling per pot 10 days after germination. Thereafter, seedlings were watered with 160 ml of nutrient solution daily (40 ml per pot every 4 h of the light period). The nutrient solution contained 1.0 mM NO<sub>3</sub>, 0.4 mM NH<sub>4</sub>, 0.5 mM K, 0.2 mM Ca, 0.1 mM Mg and SO<sub>4</sub>, 50.5 μM Cl, 20 μM Fe-EDTA, 20 μM B, 2 μM Mn and Zn, and 0.5 μM Cu, Na, Co and Mo. This watering regime was sufficient

to maintained pots near field capacity and, we assume, the concentrations of nutrients near these basal setpoints. Solution pH was adjusted to 5.6 with 0.1 N NaOH. After an additional 2 weeks, P<sub>i</sub> treatments in the form of KH<sub>2</sub>PO<sub>4</sub> were added to the baseline nutrient solution to deliver treatment solutions containing 5 μM (P<sub>i</sub> limitation) or 100 μM (control). These levels were selected based concentrations where limited (100 μM) and elevated (5 μM) stress responses (antioxidant enzyme and organic acid exudation) were reported by Desai et al. (2014). Eight replicate seedlings per P<sub>i</sub>/ECM fungal treatment combination were established. Seedlings were maintained in a climate-controlled greenhouse with supplemental lighting (mixed metal halide sources) providing a 14-h photoperiod and day/night temperatures of 24/19 ± 3 °C. Seedlings were grown for 46 days after the commencement of P<sub>i</sub> treatments (days after treatment, DAT).

### Photosynthesis and photosystem measurements

Net photosynthesis was measured on 15, 35 and 45 DAT using a Li-COR 6400 portable photosynthesis system with a 6-cm<sup>2</sup> chamber with red/blue LED light sources (Li-COR Biosciences, Lincoln, NE, USA). Photosynthetic measurements were made between 09:00 h and 16:00 h daily on the most fully expanded leaf of each plant (fourth to fifth leaf from the top). Net CO<sub>2</sub> assimilation rate (*A*), transpiration rate (*E*), stomatal conductance (*g<sub>s</sub>*) and intercellular CO<sub>2</sub> concentration (*C<sub>i</sub>*) were measured at 380 μmol mol<sup>-1</sup> CO<sub>2</sub>. Measurements were made at saturating light intensity of 1500 μmol m<sup>-2</sup> s<sup>-1</sup> and a chamber temperature of 24 °C. A–C<sub>i</sub> curves were generated using a sequence of 380, 50, 100, 150, 250, 580, 800, 1000, 1200 and 1500 μmol mol<sup>-1</sup> CO<sub>2</sub> mole fraction. The maximum rate of electron transport (*J<sub>max</sub>*) and the maximum rate of Rubisco-mediated carboxylation (*V<sub>cmax</sub>*) were derived from these measurements (Sharkey et al. 2007).

### Growth measurements, tissue P concentration and mycorrhizal colonization

Leaf P concentration was measured using four 5-mm leaf discs sampled from the leaves used during photosynthetic measurements, above. Leaf punches were flash frozen in liquid nitrogen and stored at –20 °C. Leaf discs were ashed at 475 °C for 1 h, dissolved in 1 ml 50% HCl, and crucibles rinsed with 1 ml d. H<sub>2</sub>O. The resulting 2 ml digests were vortexed until clear. Root P concentration was determined on a sample of root tissue (roots <1 mm) collected at the final harvest. The sample was dried, ground in a cyclonic sample mill and an aliquot digested as above. Tissue P in leaf and root digests was analyzed using the malachite green method (Martin et al. 1999).

At harvest, plants were separated into roots and shoots and roots were washed thoroughly with d.H<sub>2</sub>O to remove adhering substrate. Root samples (~1 g) from the center of root systems were stored in sterile distilled water at 4 °C to determine root colonization. The remaining shoot and root tissues were dried at 60 °C for 48 h to determine dry weight. Percent ECM fungal

colonization was quantified using the gridline intercept method (Giovannetti and Mosse 1980). Aspen roots were well colonized by each ECM fungus, and ranging from 72% to 77% for *L. bicolor* and from 77% to 82% for *P. involutus*; there was no evidence of short root formation in NM plants.

### Tissue C-based compounds

Tissue samples for carbohydrate and CBSC assays were flash frozen in liquid nitrogen and stored at –80 °C. Metabolites were analyzed for three plant tissues: young leaves representing the four youngest leaves from top; mature leaves, which were the remaining fully expanded leaves below young leaves; and fine root tissue representing pooled roots with diameter <1 mm.

For glucose, fructose, sucrose and starch measurements, frozen leaf and root tissues were ground cryogenically using a cryobath and ball mill equipped with a cryo-block (2600 Cryo-Station, 2650 Cryo-Block and 2000 Geno Grinder, SPEX SamplePrep, Metuchen, NJ, USA). Frozen powdered leaf and root material (20 mg) was transferred to microcentrifuge tubes to which was added 375 μl of a mixture containing 80% (v/v) ethanol and 10 mM 2-(*N*-morpholino)ethanesulphonic acid (MES), pH 6. The tubes were mixed thoroughly and incubated at 80 °C for 30 min. Extracts were clarified by centrifugation (4500g, 10 min), and the supernatant was transferred into a 96-well, deep-well microplate, stored at 4 °C. The pellets were further extracted with 225 μl of 80% (v/v) ethanol, 10 mM MES pH 6, and 375 μl of 50% (v/v) ethanol, 10 mM MES pH 6, and supernatants pooled in the cooled deep-well plate. Leaf starch remaining in the pellets was converted to glucose by incubation with amylase and amyloglucosidase (Sigma-Aldrich, St Louis, MO, USA). The glucose resulting from starch degradation and the glucose, fructose and sucrose in the ethanolic extracts were assayed using a continuous enzymatic substrate assay (Rogers et al. 2004).

For CBSC analyses, plant tissue samples (~1 g) were pulverized in liquid nitrogen using a mortar and pestle and ground in the dark in 10 ml of 80% ice-cold methanol. Ground samples were sonicated for 15 min in an ice bath and centrifuged (1700g, 5 min). Sample extracts were stored at –20 °C and the following CBSC analyses were done on each.

Total condensed tannins were measured according to Porter et al. (1985). Methanolic extracts (250 μl) were mixed 1:1 v/v with 70% acetone, 1:3 with *n*-butanol plus 0.1 ml ferric reagent (2% w/v NH<sub>4</sub>Fe(SO<sub>4</sub>)<sub>2</sub>·12 H<sub>2</sub>O in 2 M HCl), heated at 100 °C for 1 h, cooled to room temperature, and optical density (OD) taken at 550 nm. Total phenolic glycosides in the methanolic extracts were assessed following Waterhouse (2002). Methanolic extracts (100 μl) were diluted with 400 μl of 80% methanol and 2.5 ml of 10% Folin-Ciocalteu phenol reagent and 2 ml 700 mM Na<sub>2</sub>CO<sub>3</sub> were added and OD at 725 nm was determined following a 60-min incubation at room temperature. Total condensed tannins and phenolic glycosides were expressed as gallic acid equivalents per gram of plant material on fresh weight basis.

Specific CBSCs in the extracts were separated by high-performance liquid chromatography (HPLC (Varian, Walnut Creek, CA, USA) using a Luna 5  $\mu\text{m}$  C18 column (250  $\times$  4.60 mm) (Phenomenex 519,880-40, Torrance, CA, USA) and detection at 254 nm. The mobile phase consisted of a gradient of solvent A (0.5% MeOH in phosphoric acid) and solvent B (100% acetonitrile) that increased stepwise over 45 min. The elution steps were (%B) 0:30:50:65:80 each step for 5 min, followed by column cleaning with 100% MeOH for 15 min and re-equilibration for 5 min with 0.5% MeOH in phosphoric acid while maintaining a constant flow rate of 1.0 ml min<sup>-1</sup> (Mellway et al. 2009). The HPLC standards for secondary metabolites were (+)-catechin, chlorogenic acid, p-OH-cinnamic acid, myricetin, quercetin, kaempferol and procyanidin B2 obtained from Sigma Chemical Company (St Louis, MO, USA). Isorhamnetin, salicin, salicortin and tremulacin standards were kindly provided by Dr Richard Lindroth (University of Wisconsin, Madison, WI, USA).

### Statistical analysis

The experiment was established as a randomized two-way factorial design, with two  $P_i$  treatments (5  $\mu\text{M}$  and 100  $\mu\text{M}$   $P_i$ ) and three ECM fungal treatments (nonmycorrhizal (NM) control, *L. bicolor* (Lb), *P. involutus* (Pax)) with eight replicates of each combination. Samples taken on the same plants at 15, 30 and 45 DAT during the experiment (photosystem function and leaf P concentration,  $n = 3$ ) were analyzed as a repeated measures (DAT) two-way factorial analysis of variance (ANOVA). While DAT was often important in influencing photosynthesis responses, few higher-level interactions containing DAT led to presentation of effects for the  $P_i \times \text{Myc}$  interactions only in the results. The effects of  $P_i$  concentration and ECM fungal colonization on plant variables at the end of the experiment (biomass and tissue P,  $n = 5$ ; tissue secondary metabolites,  $n = 3$ ) were analyzed using two-way ANOVA ( $P_i \times \text{Myc}$ ). Data were log-transformed as needed to meet the assumptions of ANOVA. Tukey's HSD tests were utilized to identify significant differences among treatment means. Metabolite profiles were evaluated using Pearson correlation coefficients and ANOVA-simultaneous component analysis (ASCA). ASCA is designed to evaluate data matrices containing complex multi-group and multivariate data, such as those generated in metabolomics studies (Smilde et al. 2005). ASCA builds an orthogonal model through which total variation of the dataset is separated into parts corresponding to different factors, and both the covariance between the multiple variables and the design of the experiment are taken into account (Jansen et al. 2005, Smilde et al. 2005). Principal component analyses (PCAs) are then performed on centered data to obtain information on variable contribution to the ASCA component scores. Factor loadings for these components provide insight into the variables most strongly influencing aspen metabolic profiles. Statistical analysis was carried out using SAS JMP 7.0 (SAS Institute, Cary, NC, USA) and the MetStat protocol in R (Dorscheidt 2013).

## Results

### Colonization and tissue P concentrations

The concentration of P in aspen leaves was significantly reduced by  $P_i$  limitation and this effect was dependent on mycorrhizal status/symbiont ( $P < 0.001$  for the  $P_i \times \text{Myc}$  interaction) (Table 1). At 100  $\mu\text{M}$   $P_i$ , the leaf P concentration of aspen colonized by *P. involutus* was 81% and 57% greater than that of NM plants or plants colonized by *L. bicolor*, respectively. At 5  $\mu\text{M}$   $P_i$ , leaf P of aspen colonized by *L. bicolor* and *P. involutus* was 2.8- and 2.1-fold greater than that of NM plants. Comparing symbionts, leaf P concentration of aspen colonized by *L. bicolor* was unaffected by  $P_i$  limitation, whereas leaf P of plants colonized by *P. involutus* was reduced by 45% at 5  $\mu\text{M}$   $P_i$ , yet this was as high as that of NM plants grown at 100  $\mu\text{M}$   $P_i$  (Table 1). Root P concentrations in NM aspen were consistently lower than those in roots colonized by either ECM fungus and, as with leaf P concentration, root P was not affected by growth P concentration in *L. bicolor*, but declined in roots colonized by *P. involutus* at the low  $P_i$  treatment (Table 1).

### Photosystem parameters

Photosynthetic CO<sub>2</sub> uptake (*A*) was dependent on both  $P_i$  and Myc treatments and was related to leaf P concentration (Table 2, Figure 1). *A* was 63% lower in NM plants grown at 5 than at 100  $\mu\text{M}$   $P_i$ , but was not affected by low  $P_i$  in plants colonized by *L. bicolor* or *P. involutus* due to the maintenance of leaf P concentrations under  $P_i$  limitation (regression slopes for *L. bicolor* and *P. involutus* in Figure 1 were nonsignificant). Across ECM fungal treatments, stomatal conductance ( $g_s$ ) was reduced by 27% at low  $P_i$  (Table 2). While this effect was consistent across mycorrhizal treatments, plants colonized by *L. bicolor* and *P. involutus* had greater  $g_s$  in comparison with NM plants (Table 2). Rates of transpiration (*E*) of aspen followed those of  $g_s$ , where rates at 5  $\mu\text{M}$   $P_i$  were 25% less than that of plants grown at 100  $\mu\text{M}$  and were consistent across all mycorrhizal treatments (Table 2). No

Table 1. Tissue P concentrations of nonmycorrhizal (NM) aspen seedlings and seedlings colonized by *L. bicolor* (Lb) and *P. involutus* (Pax) as affected by  $P_i$  treatment. Means  $\pm$  standard errors followed by the same letter within a column are not statistically different at  $P \leq 0.05$  by Tukey's HSD.

$P_i$	ECM	Leaf P (mg P gdw <sup>-1</sup> )	Root P
5 $\mu\text{M}$	NM	0.89 $\pm$ 0.08c	0.45 $\pm$ 0.05c
	Lb	2.45 $\pm$ 0.32ab	1.34 $\pm$ 0.22ab
	Pax	1.88 $\pm$ 0.28b	0.78 $\pm$ 0.16bc
100 $\mu\text{M}$	NM	1.90 $\pm$ 0.17b	0.74 $\pm$ 0.07bc
	Lb	2.19 $\pm$ 0.26b	1.08 $\pm$ 0.14ab
	Pax	3.43 $\pm$ 0.11a	1.42 $\pm$ 0.18a
$P_{P_i}^1$		<0.001	0.022
$P_{\text{ECM}}$		<0.001	<0.001
$P_{P_i \times \text{ECM}}$		<0.001	0.027

<sup>1</sup>Probability of the  $P_i$ , ECM and  $P_i \times \text{ECM}$  treatment effects.

Table 2. Leaf photosynthetic parameters of nonmycorrhizal (NM) aspen seedlings and seedlings colonized by *L. bicolor* (Lb) and *P. involutus* (Pax) as affected by  $P_i$  treatment. Means  $\pm$  standard errors followed by the same letter within a column are not statistically different at  $P \leq 0.05$  by Tukey's HSD.

$P_i$	ECM	$A^1$	$g_s^2$	$E^3$	$C_i^4$	$V_{cmax}^5$	$J_{max}^6$
5 $\mu$ M	NM	6.1 $\pm$ 0.8b	0.137 $\pm$ 0.052b	3.14 $\pm$ 0.41	189 $\pm$ 29	36.9 $\pm$ 2.4c	41.3 $\pm$ 5.1c
	Lb	13.6 $\pm$ 1.4a	0.239 $\pm$ 0.052ab	3.07 $\pm$ 0.47	212 $\pm$ 28	53.5 $\pm$ 3.1b	67.0 $\pm$ 9.6b
	Pax	15.8 $\pm$ 1.5a	0.227 $\pm$ 0.046ab	3.56 $\pm$ 0.51	242 $\pm$ 18	58.1 $\pm$ 4.6b	73.9 $\pm$ 10.4b
100 $\mu$ M	NM	13.5 $\pm$ 1.0a	0.223 $\pm$ 0.054ab	3.51 $\pm$ 0.53	224 $\pm$ 21	72.8 $\pm$ 2.3a	94.5 $\pm$ 4.8a
	Lb	17.3 $\pm$ 1.3a	0.317 $\pm$ 0.049a	4.61 $\pm$ 0.27	235 $\pm$ 23	56.0 $\pm$ 4.6b	69.4 $\pm$ 8.9b
	Pax	14.9 $\pm$ 1.7a	0.262 $\pm$ 0.046ab	4.23 $\pm$ 0.26	261 $\pm$ 33	63.8 $\pm$ 4.4ab	70.0 $\pm$ 8.1b
$P_{P_i}^7$		0.004	0.011	0.014	0.162	<0.001	<0.001
$P_{ECM}$		<0.001	0.009	0.322	0.139	0.120	0.626
$P_{P_i \times ECM}$		0.009	0.668	0.346	0.941	<0.001	<0.001
$P_{DAT}$		0.110	<0.001	0.113	<0.001	0.004	<0.001

<sup>1</sup>Steady-state photosynthesis ( $\mu$ mol CO<sub>2</sub> m<sup>-2</sup> s<sup>-1</sup>).

<sup>2</sup>Stomatal conductance (mol m<sup>-2</sup> s<sup>-1</sup>).

<sup>3</sup>Transpiration (mmol m<sup>-2</sup> s<sup>-1</sup>).

<sup>4</sup>Leaf intracellular CO<sub>2</sub> ( $\mu$ mol mol<sup>-1</sup>).

<sup>5</sup>Maximum carboxylation rate of rubisco ( $\mu$ mol CO<sub>2</sub> m<sup>-2</sup> s<sup>-1</sup>).

<sup>6</sup>Maximum electron transport rate ( $\mu$ mol electrons m<sup>-2</sup> s<sup>-1</sup>).

<sup>7</sup>Probability of the  $P_i$ , ECM,  $P_i \times$  ECM and DAT treatment effects, respectively.

significant changes in intercellular CO<sub>2</sub> concentration ( $C_i$ ) were observed due to  $P_i$  limitation or mycorrhizal colonization (Table 2).

Changes in  $A$  were a reflection of altered photochemistry in aspen. The maximum rate of carboxylation of RuBP ( $V_{cmax}$ ) and light saturated rate of electron transport ( $J_{max}$ ) both varied with  $P_i$  treatment and ECM fungal colonization (Table 2). Nonmycorrhizal aspen exhibited the highest  $V_{cmax}$  at 100  $\mu$ M  $P_i$  with a 50% reduction at 5  $\mu$ M  $P_i$  (Table 2) and  $V_{cmax}$  declined as leaf P declined (Figure 1). As colonization by with ECM fungi sustained plant leaf P concentrations under  $P_i$  limitation,  $V_{cmax}$  was unaffected by  $P_i$  treatment in ECM aspen (Figure 1). Similarly, NM aspen exhibited the greatest  $J_{max}$  at 100  $\mu$ M  $P_i$  and the greatest inhibition at 5  $\mu$ M  $P_i$  (-59%), whereas  $J_{max}$  was unaffected by  $P_i$  treatment in plants colonized by *L. bicolor* or *P. involutus* (Table 2).

### Growth parameters

Plant biomass declined with limiting foliar P concentrations in non-mycorrhizal aspen, but this response was modulated by *L. bicolor* and *P. involutus*, with an abrupt threshold of  $\sim 1.5$  mg P g<sup>-1</sup> (Figure 2). Shoot growth of aspen did not differ among mycorrhizal treatments at 100  $\mu$ M  $P_i$ , however reductions in shoot biomass at 5  $\mu$ M  $P_i$  in NM plants (-74%) were substantially greater than reduction in plants colonized by *L. bicolor* (-48%) or *P. involutus* (-45%) (Table 3). Patterns of root allocation under  $P_i$  limitation and among mycorrhizal treatments were more complex than shoot responses. At 100  $\mu$ M  $P_i$ , plants colonized by *P. involutus* allocated 55% less C to roots than NM plants and 46% less than plants colonized by *L. bicolor* (Table 3). Root growth was reduced by 91% in NM plants at 5  $\mu$ M  $P_i$ , whereas reductions in plants colonized by *L. bicolor* and *P. involutus* were not statistically different from their corresponding root masses at 100  $\mu$ M  $P_i$  (Table 3).

### Tissue C partitioning

Phosphate ( $P_i$ ) availability and ECM symbionts significantly altered C partitioning in young and mature leaves of aspen (Table 4). Across ECM treatments, young leaves of plants grown with 5  $\mu$ M  $P_i$  exhibited lower leaf starch (-42%), sucrose (-41%), glucose (-30%) and sucrose (-35%) concentrations and higher phenol (+38%) and tannin (+38%) concentrations (Table 4). However, the extent of these reductions was differentially modulated by *L. bicolor* and *P. involutus*, with partitioning in aspen colonized by *L. bicolor* exhibiting patterns intermediate between NM aspen and aspen colonized by *P. involutus* (Table 4). Phenolic glycoside and tannin concentrations in young leaves were also higher in NM aspen compared with mycorrhizal aspen grown at 100  $\mu$ M  $P_i$ , suggesting that the ECM associations increase resource availability under this treatment as well as under  $P_i$  limitation. Mature leaf nonstructural carbohydrate (NSC, starch + soluble sugars) partitioning was similarly affected by  $P_i$  availability, and increases in phenolic glycoside and tannin accumulation were also noted in NM aspen under  $P_i$  limitation (Table 4).

Across all treatments, total NSC accumulation was negatively correlated with the accumulation of total CBSCs (phenolic glycosides + tannins) in young leaves ( $r = -0.624$ ,  $P = 0.006$ ), but not in mature leaves ( $r = -0.169$ ,  $P = 0.518$ ). In young leaves, NSC and total CBSC accretion were positively and negatively correlated, respectively, with leaf P concentration (Figure 3). A similar relationship was noted for NSCs and total CBSCs in mature leaves ( $r = 0.563$ ,  $P = 0.019$ ) (data not presented). Both ECM fungi modulated these C partitioning relationships, maintaining higher NSCs and lower total CBSCs in leaves primarily by maintaining leaf P concentrations under  $P_i$  limitation (Figure 3, Table 4).

In contrast to leaves, NSC and total CBSC concentrations in roots of aspen were not correlated ( $r = 0.145$ ,  $P = 0.566$ ) and

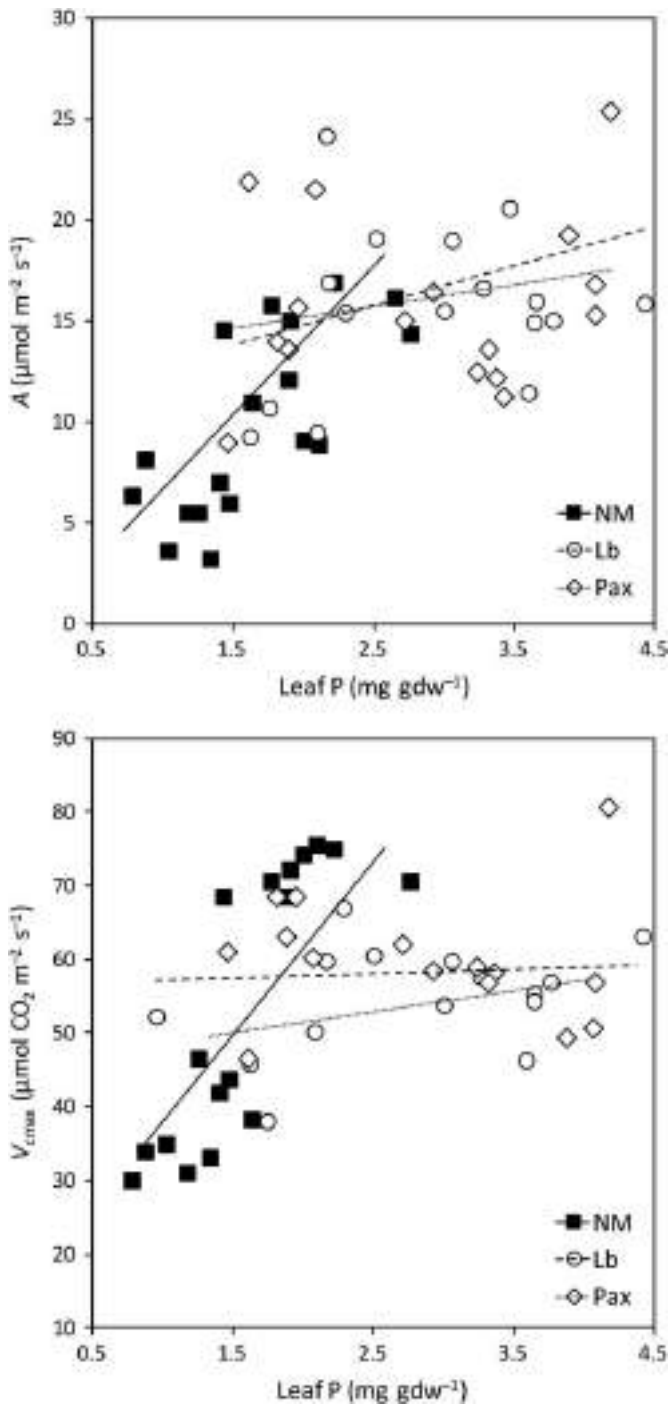


Figure 1. Steady-state photosynthetic  $\text{CO}_2$  uptake ( $A$ ) (top) and the maximum rate of RuBP carboxylation ( $V_{c\max}$ ) (bottom) in relation to leaf P concentrations for nonmycorrhizal (NM) aspen seedlings and seedlings colonized by *L. bicolor* (Lb) and *P. involutus* (Pax).

there were no relationships with root P concentration ( $r = 0.001$  and  $0.044$  for NSCs and CBSCs, respectively). However, C partitioning in roots was significantly altered by the treatment factors. In NM aspen,  $\text{P}_i$  limitation increased the accumulation of starch (3.9-fold), sucrose (2.9-fold), glucose (1.5-fold) and fructose

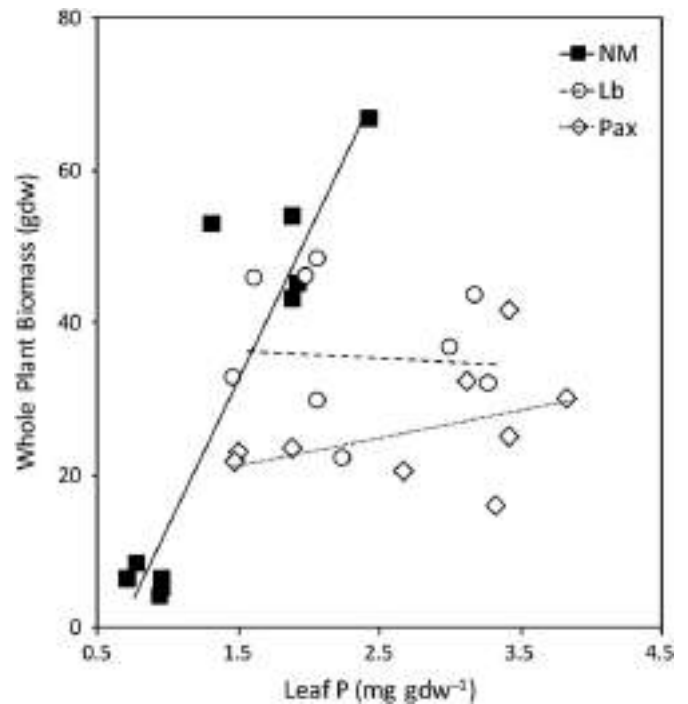


Figure 2. Whole plant biomass in relation to leaf P concentrations for nonmycorrhizal (NM) aspen seedlings and seedlings colonized by *L. bicolor* (Lb) and *P. involutus* (Pax).

(1.7-fold), whereas only sucrose increased in roots colonized *L. bicolor* (+29%) and *P. involutus* (+49%) (Figure 4, Table 4). In addition to these fundamental C shifts due to  $\text{P}_i$  limitation, there were fundamental shifts in C partitioning in aspen roots resulting from mycorrhizal colonization. Both *L. bicolor* and *P. involutus* increased root starch (3.3- and 5.7-fold, respectively) and sucrose (2.7- and 2.8-fold), but decreased glucose and fructose concentrations, compared with NM roots (Figure 4, Table 4). In addition, roots of aspen colonized by *P. involutus* exhibited greater concentrations of tannins when  $\text{P}_i$  was not limiting (Figure 4, Table 4).

Across all treatments, the accumulation of specific CBSCs in young leaves was negatively correlated with leaf P, starch, glucose, fructose and sucrose accumulation and, in general, all positively correlated among themselves and with phenolic glycosides, but less so with tannins (Table 5; see Table S1 available as Supplementary Data at *Tree Physiology* Online). For example, young leaf catechin concentration declined  $\sim 8$ -fold across the range of leaf P concentrations (Figure 5), with leaves of plants colonized by *L. bicolor* and *P. involutus* maintaining catechin concentrations at or well below concentrations of NM plants, especially those grown at  $5 \mu\text{M} \text{P}_i$  (Figure 5). Other CBSCs exhibited similar patterns in young leaves (Table 5; see Table S1 available as Supplementary Data at *Tree Physiology* Online). These patterns were also evident in mature leaves, although correlations between CBSCs and NSCs were minimal (Table 5; see Table S1 available as Supplementary Data at *Tree*

Table 3. Biomass of nonmycorrhizal (NM) aspen seedlings and seedlings colonized by *L. bicolor* (Lb) and *P. involutus* (Pax) as affected by  $P_i$  treatment. Means  $\pm$  standard errors followed by the same letter within a column are not statistically different at  $P \leq 0.05$  by Tukey's HSD.

$P_i$	ECM	Shoot (gdw)	Root (gdw)	Root:shoot	Total plant (gdw)
5 $\mu$ M	NM	1.76 $\pm$ 0.28c	4.0 $\pm$ 0.91d	2.75 $\pm$ 0.91b	5.76 $\pm$ 0.71c
	Lb	3.82 $\pm$ 0.27b	25.0 $\pm$ 2.8bc	6.51 $\pm$ 0.47a	28.8 $\pm$ 2.9b
	Pax	4.10 $\pm$ 0.4b	18.0 $\pm$ 0.6c	4.52 $\pm$ 0.48ab	22.1 $\pm$ 0.7b
100 $\mu$ M	NM	6.88 $\pm$ 0.27a	45.1 $\pm$ 4.4a	6.71 $\pm$ 0.95a	52.0 $\pm$ 4.2a
	Lb	7.34 $\pm$ 0.9a	37.1 $\pm$ 5.3ab	5.58 $\pm$ 0.96ab	46.4 $\pm$ 5.4a
	Pax	7.50 $\pm$ 0.8a	21.4 $\pm$ 4.3c	2.99 $\pm$ 0.68b	28.9 $\pm$ 4.2b
$P_{P_i}^1$		<0.001	<0.001	0.450	<0.001
$P_{ECM}$		<0.001	<0.001	<0.029	<0.001
$P_{P_i \times ECM}$		<0.001	<0.001	0.003	<0.001

<sup>1</sup>Probability of the  $P_i$ , ECM and  $P_i \times ECM$  treatment effects, respectively.

Table 4. Partitioning of C among nonstructural carbohydrates, total phenolic glycosides, and tannins (mg gfw<sup>-1</sup>) in young leaves, mature leaves and fine roots of nonmycorrhizal (NM) aspen seedlings and seedlings colonized by *L. bicolor* (Lb) and *P. involutus* (Pax) as affected by  $P_i$  treatment. Means  $\pm$  standard errors followed by the same letter within a column are not statistically different at  $P \leq 0.05$  by Tukey's HSD.

$P_i$	ECM	Starch	Glucose	Fructose	Sucrose	Phenols	Tannins
Young leaf							
5 $\mu$ M	NM	17.9 $\pm$ 0.7d	4.78 $\pm$ 0.36d	4.27 $\pm$ 0.32c	10.4 $\pm$ 0.1d	23.00 $\pm$ 1.43a	10.71 $\pm$ 0.58a
	Lb	26.0 $\pm$ 2.5c	5.95 $\pm$ 0.15c	5.08 $\pm$ 0.28c	10.6 $\pm$ 0.2d	11.06 $\pm$ 1.05bc	6.81 $\pm$ 0.52ab
	Pax	22.2 $\pm$ 1.9c	7.12 $\pm$ 0.84bc	6.41 $\pm$ 0.16b	13.8 $\pm$ 0.1c	8.75 $\pm$ 1.37 cd	7.33 $\pm$ 1.42ab
100 $\mu$ M	NM	33.9 $\pm$ 0.3b	7.53 $\pm$ 0.28b	7.60 $\pm$ 0.17b	17.5 $\pm$ 0.2b	16.06 $\pm$ 1.88ab	9.75 $\pm$ 0.94a
	Lb	36.7 $\pm$ 2.1ab	7.30 $\pm$ 0.38b	7.42 $\pm$ 0.15b	17.3 $\pm$ 0.1b	8.95 $\pm$ 1.47 cd	7.03 $\pm$ 2.04ab
	Pax	41.6 $\pm$ 1.3a	10.13 $\pm$ 0.23a	9.06 $\pm$ 0.02a	24.1 $\pm$ 0.1a	6.26 $\pm$ 0.57d	4.30 $\pm$ 0.75b
$P_{P_i}^1$		<0.001	<0.001	<0.001	<0.001	0.007	0.136
$P_{ECM}$		<0.001	<0.001	<0.001	<0.001	<0.001	0.011
$P_{P_i \times ECM}$		0.553	0.164	0.013	0.021	0.842	0.401
Mature leaf							
5 $\mu$ M	NM	18.7 $\pm$ 0.3c	4.06 $\pm$ 0.15d	4.23 $\pm$ 0.15d	11.2 $\pm$ 0.6d	13.45 $\pm$ 5.14a	10.56 $\pm$ 3.34a
	Lb	19.7 $\pm$ 0.7c	5.02 $\pm$ 0.45d	4.92 $\pm$ 0.45 cd	11.9 $\pm$ 0.6d	7.09 $\pm$ 1.23b	7.00 $\pm$ 3.04ab
	Pax	22.8 $\pm$ 0.4c	5.93 $\pm$ 0.12c	6.19 $\pm$ 0.12bc	14.0 $\pm$ 0.1c	6.37 $\pm$ 0.88b	6.41 $\pm$ 2.41b
100 $\mu$ M	NM	36.8 $\pm$ 1.6b	7.72 $\pm$ 0.14b	8.71 $\pm$ 0.14ab	16.8 $\pm$ 0.8b	7.31 $\pm$ 0.24b	6.68 $\pm$ 0.15ab
	Lb	36.3 $\pm$ 0.5b	7.78 $\pm$ 0.23b	7.71 $\pm$ 0.23ab	18.1 $\pm$ 1.1ab	6.69 $\pm$ 0.29b	7.42 $\pm$ 0.20ab
	Pax	48.4 $\pm$ 2.5a	9.93 $\pm$ 0.13a	8.44 $\pm$ 0.13a	20.9 $\pm$ 0.2a	7.12 $\pm$ 0.98b	6.88 $\pm$ 2.60b
$P_{P_i}^1$		<0.001	<0.001	<0.001	<0.001	0.013	0.313
$P_{ECM}$		<0.001	<0.001	0.010	<0.001	0.123	0.007
$P_{P_i \times ECM}$		0.491	0.158	0.060	0.071	0.013	0.211
Fine root							
5 $\mu$ M	NM	7.34 $\pm$ 0.47b	6.05 $\pm$ 0.22a	6.33 $\pm$ 0.10a	7.34 $\pm$ 0.21c	2.92 $\pm$ 0.33	3.28 $\pm$ 0.52ab
	Lb	5.54 $\pm$ 0.31c	1.92 $\pm$ 0.01c	1.97 $\pm$ 0.03c	9.10 $\pm$ 0.39b	2.61 $\pm$ 0.52	3.01 $\pm$ 0.41ab
	Pax	9.54 $\pm$ 0.53a	1.19 $\pm$ 0.15d	1.14 $\pm$ 0.17d	10.64 $\pm$ 0.12a	2.27 $\pm$ 0.34	2.26 $\pm$ 0.27b
100 $\mu$ M	NM	1.86 $\pm$ 0.09d	3.99 $\pm$ 0.15b	3.80 $\pm$ 0.06b	2.57 $\pm$ 0.09d	2.56 $\pm$ 0.65	2.20 $\pm$ 0.54b
	Lb	6.13 $\pm$ 0.08 c	1.73 $\pm$ 0.18c	2.30 $\pm$ 0.15c	7.05 $\pm$ 0.09c	2.86 $\pm$ 0.61	2.46 $\pm$ 0.51b
	Pax	9.97 $\pm$ 0.12a	1.58 $\pm$ 0.08 cd	1.34 $\pm$ 0.01d	7.10 $\pm$ 0.04c	4.21 $\pm$ 0.31	6.42 $\pm$ 0.70a
$P_{P_i}^1$		<0.001	<0.001	<0.001	<0.001	0.242	0.353
$P_{ECM}$		<0.001	<0.001	<0.010	<0.001	0.635	0.080
$P_{P_i \times ECM}$		<0.001	<0.001	<0.001	<0.001	0.112	0.002

<sup>1</sup>Probability of the  $P_i$ , ECM and  $P_i \times ECM$  treatment effects, respectively.

Physiology Online). In roots, in contrast, specific CBSCs exhibited positive correlations with glucose and fructose concentration, but not with starch, sucrose, phenolic glycosides or tannins (Table 5; see Table S1 available as Supplementary Data at *Tree Physiology* Online).

ANOVA-simultaneous component analysis (ASCA) was applied to the combined NSC and CBSC data. ASCA decomposes this data matrix into effect matrices (e.g., ECM and  $P_i$ ) and residual matrices to evaluate variation among treatment effects within the multivariate data (Zwanenburg et al. 2011). Similar to

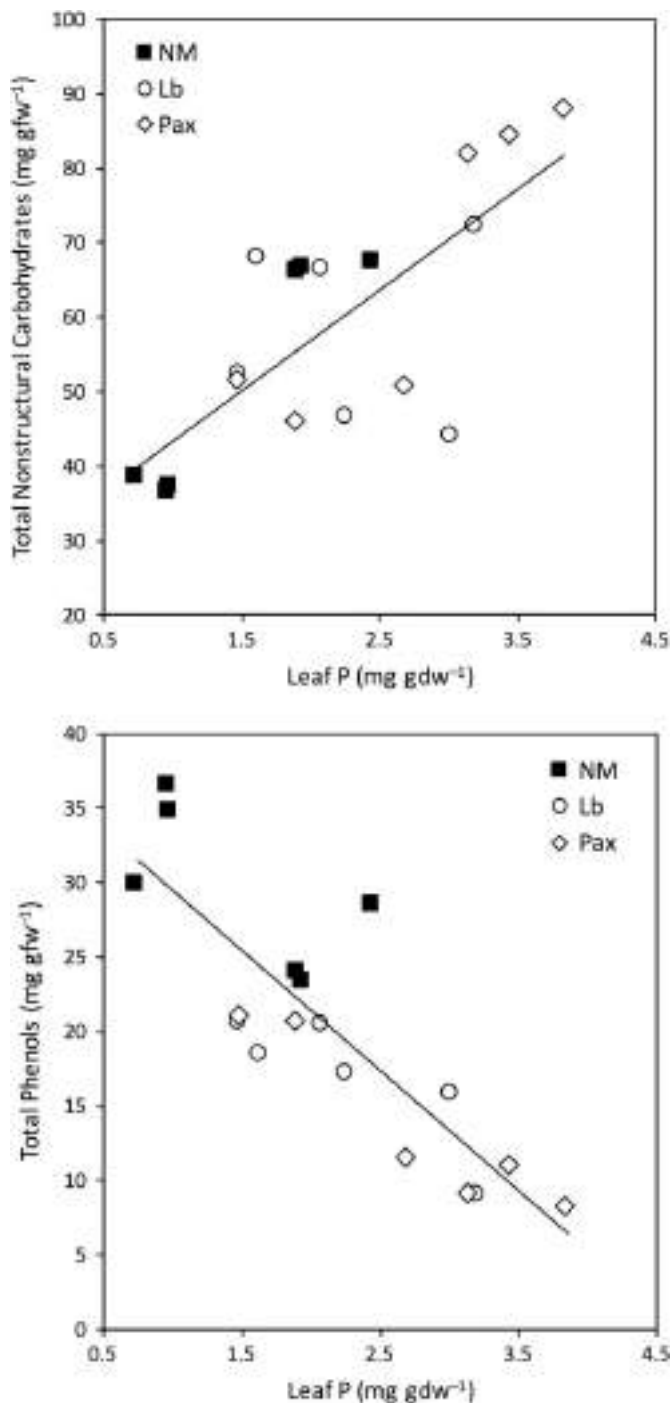


Figure 3. The accumulation of total nonstructural carbohydrates (top) and total phenols (bottom) in relation to leaf P concentrations in young leaves for nonmycorrhizal (NM) aspen seedlings and seedlings colonized by *L. bicolor* (Lb) and *P. involutus* (Pax).

PCA, ASCA provides PCs and loading scores that reflect data dispersion, but these take into account structured treatments.

In young leaves, distinct differences in the fate of C in aspen seedlings were evident among ECM treatments. Nonmycorrhizal aspen and aspen colonized by *L. bicolor* or *P. involutus* fell into three distinct clusters (Figure 6), with 90% of that variation

between mycorrhizal treatments accounted for in PC1 that reflected trade-offs between NSCs and CBSCs primarily separating NM from the two ECM fungal treatments (Figure 6). A further separation in C partitioning was evident in PC2, separating *P. involutus* from NM and *L. bicolor* aspen based on soluble sugars and kaempferol. Seedlings colonized by *P. involutus* accumulated between 25% and 41% more sugars than other ECM treatments, whereas kaempferol concentrations in young leaves from NM and *L. bicolor* aspen were twofold greater than those from *P. involutus* seedlings (Table 4). Separation of mature leaves was also evident via ASCA and similar to that of young leaves, with NSCs and CBSCs separating NM and the two ECM treatments on PC1 and NSCs and kaempferol on PC2 (data not presented).

The three ECM treatments were also clearly separated based on root chemistry (Figure 7). In this case, the accumulation of starch and sucrose and reduced monosaccharides, tremulacin and myricetin separated roots colonized by *L. bicolor* or *P. involutus* from NM roots along PC1, while starch and phenolic glycosides, specifically catechin and kaempferol, contributed to separation of the three mycorrhizal treatments along PC2 (Figure 7).

## Discussion

Soil nutrient limitation, especially N and P, limits the productivity of many natural and planted forests (Kirkman et al. 2001, Wardle et al. 2004, St Clair et al. 2008, Hou et al. 2012). Under such conditions, trees depend on integrated physiological adjustments as well as symbiotic mycorrhizal fungi to enhance nutrient acquisition and increase nutrient-use efficiency, and together these will influence C capture, allocation and partitioning in trees and the fate of C in forested ecosystems.

### Phosphate limitation and ECM alter C fixation and allocation in aspen

Phosphorus limitation often reduces the rate of photosynthesis and plant productivity (Wissuwa et al. 2005, Boyce et al. 2006, Thomas et al. 2006). Under  $P_i$  limitation, photosynthetic  $CO_2$  uptake was reduced in NM aspen, but remained unaffected in plants colonized by either symbiont (Table 2). This maintenance of photosynthesis at low  $P_i$  was related to the maintenance of leaf P concentrations above a limiting threshold of  $\sim 1.5 \text{ mg g}^{-1}$  (Figure 1). Reductions in  $A$  were accompanied by parallel reductions in  $J_{\text{max}}$  and  $V_{\text{cmax}}$  (Table 2), indicating that low leaf P concentration in NM aspen constrained the biochemistry of C fixation (Loustau et al. 1999, Bown et al. 2007). In contrast, enhanced  $P_i$  acquisition by *L. bicolor* or *P. involutus* at low  $P_i$  sustained the reactions of  $CO_2$  fixation at the whole plant and biochemical levels.

Although ECM colonization moderated reductions in plant growth under  $P_i$  limitation, the two ECM symbionts differentially influenced host plant growth, C allocation and growth-tissue P concentration relationships (Table 3, Figure 3). The C cost of sustaining *P. involutus* in symbiosis was significant, with aspen

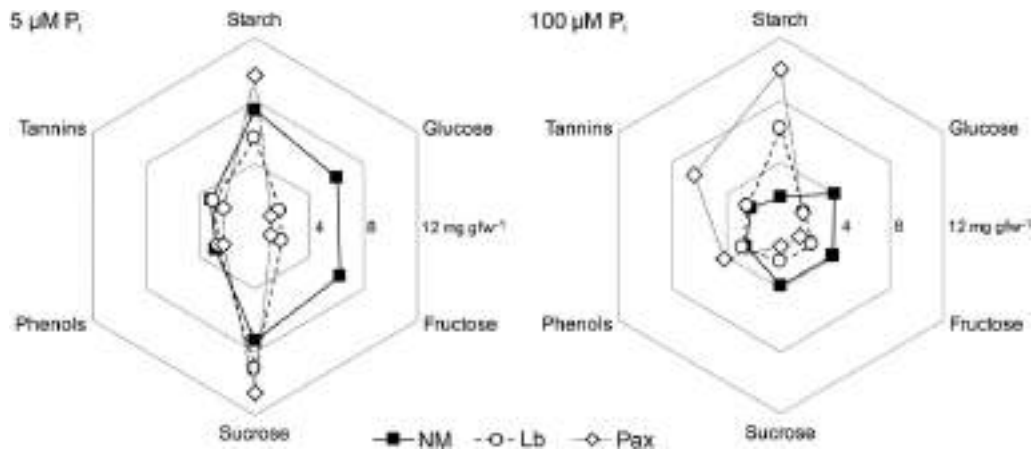


Figure 4. Partitioning of C between starch, sugars, total phenolic glycosides and total tannins in fine roots of nonmycorrhizal (NM) aspen seedlings and seedlings colonized by *L. bicolor* (Lb) and *P. involutus* (Pax) grown at 5  $\mu\text{M}$  (left) and 100  $\mu\text{M}$  (right)  $P_i$ .

Table 5. Partitioning of C among phenolic glycosides and flavonoids ( $\text{mg gfw}^{-1}$ ) in young leaves, mature leaves and fine roots of nonmycorrhizal (NM) aspen seedlings and seedlings colonized by *L. bicolor* (Lb) and *P. involutus* (Pax) as affected by  $P_i$  treatment. Means  $\pm$  standard errors followed by the same letter within a column are not statistically different at  $P \leq 0.05$  by Tukey's HSD.

$P_i$	ECM	Salicin	Catechin	Kaempferol	Salicortin	Procyanidin	Tremulacin	Myricitin
Young leaf								
5 $\mu\text{M}$	NM	2.84 $\pm$ 0.15a	4.35 $\pm$ 0.77a	0.251 $\pm$ 0.098ab	5.46 $\pm$ 2.15a	7.01 $\pm$ 1.00a	2.09 $\pm$ 0.14a	2.06 $\pm$ 0.03a
	Lb	2.47 $\pm$ 0.68a	2.08 $\pm$ 0.39ab	0.249 $\pm$ 0.046a	3.35 $\pm$ 0.17a	2.32 $\pm$ 0.15bc	0.78 $\pm$ 0.01abc	0.44 $\pm$ 0.05bc
	Pax	2.04 $\pm$ 0.20a	2.44 $\pm$ 0.15ab	0.186 $\pm$ 0.043ab	3.35 $\pm$ 1.23a	2.50 $\pm$ 0.35bc	0.83 $\pm$ 0.31abc	0.51 $\pm$ 0.08abc
100 $\mu\text{M}$	NM	3.11 $\pm$ 0.64a	2.42 $\pm$ 0.30ab	0.297 $\pm$ 0.066a	5.22 $\pm$ 1.15a	4.62 $\pm$ 1.30ab	1.35 $\pm$ 0.37ab	1.54 $\pm$ 0.64ab
	Lb	1.47 $\pm$ 0.26ab	1.44 $\pm$ 0.44bc	0.204 $\pm$ 0.029ab	2.02 $\pm$ 0.42a	2.04 $\pm$ 0.29bc	0.54 $\pm$ 0.07bc	0.26 $\pm$ 0.03c
	Pax	0.81 $\pm$ 0.16b	0.82 $\pm$ 0.14c	0.077 $\pm$ 0.016b	1.43 $\pm$ 0.31a	1.30 $\pm$ 0.25c	0.32 $\pm$ 0.06c	0.16 $\pm$ 0.02c
$P_i^1$	0.007	<0.001	0.183	0.174	0.016	0.012	0.006	
$P_{\text{ECM}}$	0.001	<0.001	0.016	0.073	<0.001	<0.001	<0.001	
$P_i \times \text{ECM}$	0.046	0.203	0.114	0.369	0.425	0.662	0.553	
Mature leaf								
5 $\mu\text{M}$	NM	1.41 $\pm$ 0.15a	2.79 $\pm$ 0.23a	0.080 $\pm$ 0.003ab	2.36 $\pm$ 0.20a	2.07 $\pm$ 0.08a	0.466 $\pm$ 0.052a	0.436 $\pm$ 0.078a
	Lb	1.18 $\pm$ 0.13a	1.45 $\pm$ 0.09a	0.078 $\pm$ 0.007ab	1.52 $\pm$ 0.11b	1.49 $\pm$ 0.23ab	0.322 $\pm$ 0.036ab	0.290 $\pm$ 0.029a
	Pax	1.06 $\pm$ 0.14a	3.17 $\pm$ 0.86a	0.066 $\pm$ 0.018ab	1.76 $\pm$ 0.08ab	1.30 $\pm$ 0.12b	0.281 $\pm$ 0.009b	0.250 $\pm$ 0.017a
100 $\mu\text{M}$	NM	1.47 $\pm$ 0.20a	1.94 $\pm$ 0.43a	0.122 $\pm$ 0.001a	2.26 $\pm$ 0.08ab	2.02 $\pm$ 0.10ab	0.414 $\pm$ 0.028ab	0.299 $\pm$ 0.003a
	Lb	1.10 $\pm$ 0.03a	2.12 $\pm$ 0.40a	0.098 $\pm$ 0.018ab	1.90 $\pm$ 0.16ab	1.41 $\pm$ 0.10ab	0.342 $\pm$ 0.031ab	0.281 $\pm$ 0.027a
	Pax	1.15 $\pm$ 0.12a	1.97 $\pm$ 0.47a	0.051 $\pm$ 0.008b	2.09 $\pm$ 0.24ab	1.41 $\pm$ 0.14ab	0.336 $\pm$ 0.025ab	0.268 $\pm$ 0.026a
$P_i^1$	0.787	0.346	0.339	0.147	0.958	0.659	0.293	
$P_{\text{ECM}}$	0.078	0.305	0.008	0.017	0.003	0.006	0.053	
$P_i \times \text{ECM}$	0.800	0.128	0.169	0.389	0.814	0.314	0.258	
Fine root								
5 $\mu\text{M}$	NM	0.370 $\pm$ 0.089	1.31 $\pm$ 0.21	0.300 $\pm$ 0.046	0.607 $\pm$ 0.122	0.880 $\pm$ 0.132a	0.107 $\pm$ 0.015a	1.28 $\pm$ 0.27a
	Lb	0.130 $\pm$ 0.046	0.80 $\pm$ 0.10	0.157 $\pm$ 0.020	0.343 $\pm$ 0.039	0.363 $\pm$ 0.030b	0.037 $\pm$ 0.007b	0.17 $\pm$ 0.023c
	Pax	0.103 $\pm$ 0.050	0.96 $\pm$ 0.25	0.210 $\pm$ 0.055	0.320 $\pm$ 0.052	0.347 $\pm$ 0.024b	0.027 $\pm$ 0.003b	0.23 $\pm$ 0.01bc
100 $\mu\text{M}$	NM	0.143 $\pm$ 0.020	0.87 $\pm$ 0.07	0.180 $\pm$ 0.017	0.337 $\pm$ 0.020	0.223 $\pm$ 0.026b	0.040 $\pm$ 0.005b	0.56 $\pm$ 0.24ab
	Lb	0.163 $\pm$ 0.012	0.84 $\pm$ 0.19	0.197 $\pm$ 0.044	0.353 $\pm$ 0.047	0.387 $\pm$ 0.038b	0.033 $\pm$ 0.007b	0.28 $\pm$ 0.04bc
	Pax	0.097 $\pm$ 0.047	1.21 $\pm$ 0.04	0.243 $\pm$ 0.034	0.350 $\pm$ 0.057	0.410 $\pm$ 0.098b	0.040 $\pm$ 0.010b	0.29 $\pm$ 0.04bc
$P_i^1$	0.604	0.877	0.809	0.233	0.005	0.125	0.7052	
$P_{\text{ECM}}$	0.053	0.237	0.263	0.115	0.417	0.004	<0.001	
$P_i \times \text{ECM}$	0.249	0.192	0.145	0.085	<0.001	0.009	0.009	

<sup>1</sup>Probability of the  $P_i$ , ECM and  $P_i \times \text{ECM}$  treatment effects, respectively.

total plant mass being 44% less than NM plants grown at 100  $\mu\text{M}$   $P_i$ , primarily reflecting significantly less C allocation to root biomass (Table 3). Biomass of aspen colonized by *L. bicolor*

was intermediate between NM aspen and aspen colonized by *P. involutus* at 100  $\mu\text{M}$   $P_i$ . Although there was evidence of a significant cost to aspen of maintaining the ECM symbioses,

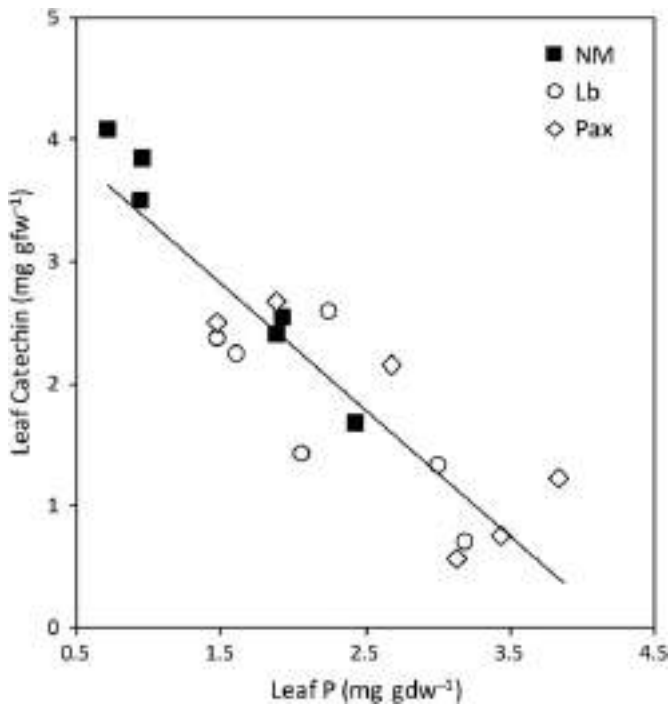


Figure 5. The accumulation of catechin in young leaves in relation to leaf P concentrations for nonmycorrhizal (NM) aspen seedlings and seedlings colonized by *L. bicolor* (Lb) and *P. involutus* (Pax).

photosynthesis was not stimulated (Table 2), although the highest individual rates were recorded in mycorrhizal plants (Figure 1). Ectomycorrhizal fungi may or may not stimulate CO<sub>2</sub> assimilation when growth is limited due to sink demand (e.g., Conjeaud et al. 1996, Wright et al. 2000, Heinonsalo et al. 2010), but variation among ECM and differences in experimental systems makes generalization difficult.

These changes in allocation belowground may reflect C allocation shifts from roots to the fungal partners. Although we did not assess hyphal biomass in this study, mycorrhizal colonization alters C allocation through the construction of hyphae, fungal respiration, and other fungal metabolic demands (Conjeaud et al. 1996, Choi et al. 2008, Makita et al. 2012). These changes may greatly increase the nutrient capture capacity of the plant and lead to reduced need for root surface area under P replete conditions, yet sustained P<sub>i</sub> acquisition under P<sub>i</sub> limitation (Lopéz-Bucio et al. 2002).

These differences between *L. bicolor* and *P. involutus* are supported by other reports of ECM-species variation in P acquisition and C allocation/partitioning (Cumming 1996, van Tichelen and Colpaert 2000, Heinonsalo et al. 2010). For example, significant variation in C allocation occurs in ectomycorrhizal *Pinus sylvestris*, with *P. involutus* allocating less C to roots than *L. bicolor*, which maintained a more even balance between root and shoot (Fransson et al. 2007), patterns noted here for aspen. Similarly, *P. involutus* exerted a significant C cost on *Betula pedula* (Wright et al. 2000), aligning with patterns noted for aspen in the current

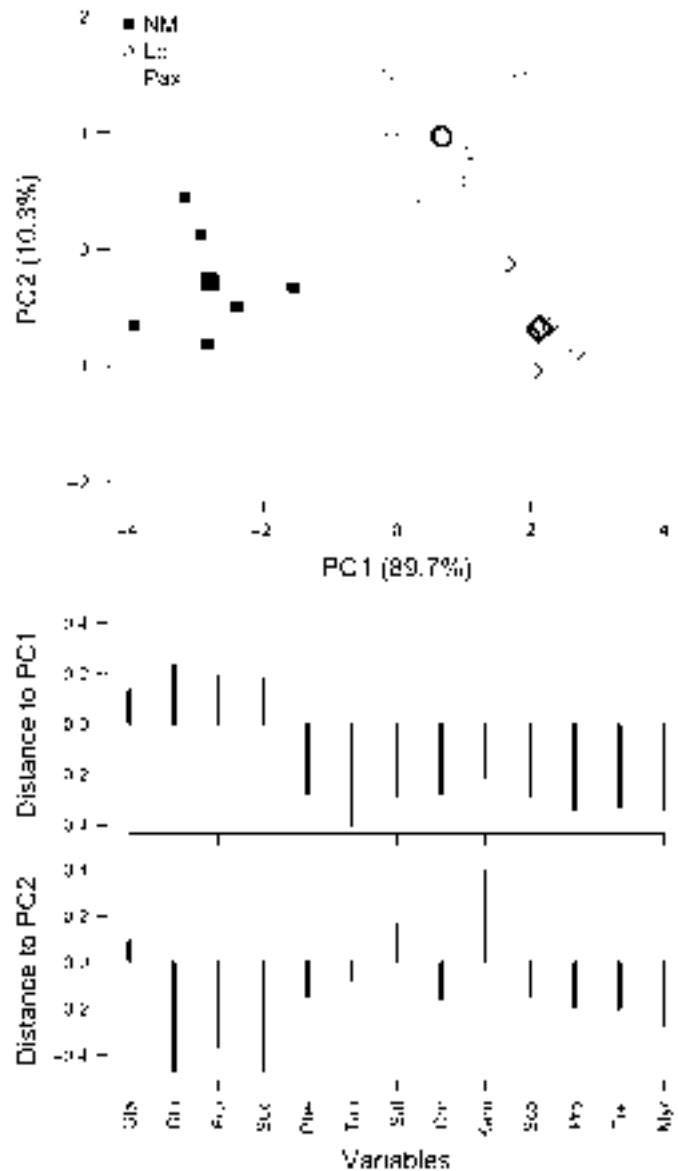


Figure 6. ASCA separation of nonmycorrhizal (NM) aspen seedlings and seedlings colonized by *L. bicolor* (Lb) and *P. involutus* (Pax) based on variation among primary and secondary carbon metabolites in young leaves (top) and the relative influences of each on the principal components (bottom). Bold/larger symbols in upper figure are the multivariate mean responses for each mycorrhizal treatment. Abbreviations at bottom: Sta = starch, Glu = glucose, Fru = fructose, Suc = sucrose, Phe = phenolics, Tan = tannins, Sal = salicin, Cat = catechin, Kae = kaempferol, Sco = salicortin, Pro = procyanidin B2, Tre = tremulacin, Myr = myricetin.

experiment. Thus, the interplay between fungal C-use efficiency, the acquisition of nutrient resources such as P, and plant acclimation to symbiont C demand and P exchange will ultimately influence the growth and C allocation outcomes in the ECM symbiosis.

### Phosphate limitation and ECM change tissue chemistry and C partitioning in aspen

Plant C partitioning changes under nutrient stress (Kleiner et al. 1998, Hale et al. 2005, Yin et al. 2009, Kleczewski et al. 2012)

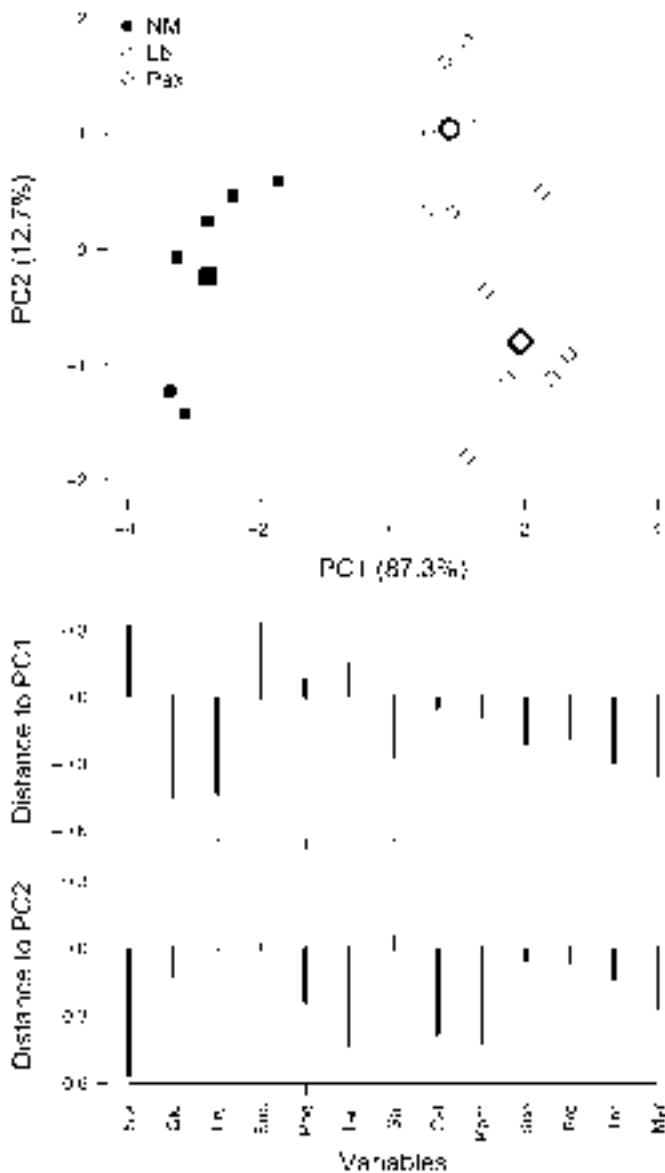


Figure 7. ASCA separation of nonmycorrhizal (NM) aspen seedlings and seedlings colonized by *L. bicolor* (Lb) and *P. involutus* (Pax) based on variation among primary and secondary carbon metabolites in fine roots (top) and the relative influences of each on the principal components (bottom). Bold/larger symbols in upper figure are the multivariate mean responses for each mycorrhizal treatment. Abbreviations as in Figure 6.

and such changes may be further modified during mycorrhizal symbiosis (Baum et al. 2009, Sanchez-Zabala et al. 2013). In the current experiment, NSC concentrations declined in young and mature leaves of aspen under  $P_i$  limitation (Figure 3). These changes were mitigated in plants colonized by *P. involutus* while plants colonized by *L. bicolor* exhibited carbohydrate profiles more similar to NM plants. In roots, NSC patterns were more complex, as starch, sucrose and monosaccharides increased in NM aspen under  $P_i$  limitation, whereas only sucrose increased in roots colonized by *L. bicolor* or *P. involutus* (Figure 4). Elevated monosaccharide concentrations in NM roots at low  $P_i$  may reflect part of the PSR signaling system designed to initiate

$P_i$ -deprivation acclimation pathways (Zhang et al. 2014). Patterns of elevated sucrose and generally lower monosaccharide concentrations in ECM roots may reflect the preferential use of glucose and fructose by the symbionts and the sink stimulation of sucrose transport to ECM roots (Nehls and Hampp 2000, Wright et al. 2000, Nehls 2008).

In the current study, CBSC concentrations were typically higher in NM aspen, and the CBSC profiles of young leaves, mature leaves and roots delineated ECM species-specific influences on aspen metabolism. The accumulation of CBSCs in tissues may reflect partitioning of C to storage under  $P_i$  limitation or physiological acclimation pathways associated with free radical production under nutrient limitation (Hale et al. 2005, Baum et al. 2009, Abdel-lateif et al. 2016) as well as changes in host physiology in support of colonization (Weiss et al. 1997, Jung and Tamai 2012, Sanchez-Zabala et al. 2013). In aspen leaves, the accumulation of catechin and kaempferol were major responses of aspen to  $P_i$ -ECM treatments, with these and other CBSCs accumulating under  $P_i$  limitation (Figure 6, Table 4). *Paxillus involutus* was more effective at mediating these perturbations to C partitioning in aspen than *L. bicolor*, which may reflect the influence of this symbiont in constraining plant growth compared with NM and *L. bicolor* aspen. In another study on *P. tremuloides*, foliar tannins increased up to 5-fold under N limitation and relative growth rates of plants were negatively correlated with C partitioned to foliar tannins and phenolic glycosides (Donaldson et al. 2006). In *Eucalyptus*, low  $P_i$  affected metabolites of the phenylpropanoid pathway, with quinic acid and catechin increasing in leaves as  $P_i$  declined from 100 to 5  $\mu\text{M}$  (Warren 2011). Thus, these shifts of C from growth and NSC pools to CBSCs under  $P_i$  limitation in aspen reflect fundamental shifts in metabolism resulting from nutrient stress.

In aspen roots, there were also distinct shifts in C partitioning induced by  $P_i$  limitation and by colonization by ECM. Notable were lower concentrations of glucose and sucrose under all  $P_i$  conditions and shifts to sucrose under  $P_i$  limitation in ECM roots, whereas large increases in all NSCs and several CBSCs were induced by low  $P_i$  in NM aspen roots (Figure 4). These increases in sugars, especially sucrose, may reflect integrated PSR systems response to  $P_i$  limitation (López-Arredondo et al. 2014). In roots colonized by *P. involutus*, the large reduction in tannins, which are present in hyphae of this species (Gafur et al. 2004, Jacob et al. 2004), grown at low  $P_i$  may reflect diversion of C away from tannins to fungal hyphal growth or other PSR systems, and not a response of the aspen host per se. This is supported by the lack of correlations between phenols or tannins and any of the specific CBSC in roots (see Table S1 available as Supplementary Data at *Tree Physiology* Online).

#### Variation between ECM for $P_i$ acquisition, C relations and stress responses in aspen

Ectomycorrhizal fungus species vary greatly in their influences on tree root physiology and response to  $P_i$  availability in the

environment (Plassard and Dell 2010, Cumming et al. 2015). There are differences among fungi in their capacity to transport  $P_i$  (Cumming 1996, Van Tichelin and Colpaert 2000), produce mineral-dissolving exudates (Casarin et al. 2004, Johansson et al. 2009) and exude enzymes to alter  $P_o$ - $P_i$  equilibria in the rhizosphere (Ali et al. 2009, Alvarez et al. 2012). In the current study, *L. bicolor* and *P. involutus* were used as model ECM species. *Laccaria bicolor* is a cosmopolitan species frequently associating with *Populus* in forest ecosystems (Martin et al. 1999, Ostry et al. 2011); *P. involutus* is equally far-ranging (Lamaison and Polese 2008), and both have been used extensively in mycorrhizal research. Our previous work indicated that these ECM fungi differ in their P starvation responses (Cumming 1996), thus we selected them for use here. The modification of P and C relations of aspen would be expected to vary greatly based on fungal symbiont community, and these two fungi may encompass only a portion of the potential range of aspen C metabolism modification in response to P limitation. Further, although roots of aspen will be, by-and-large, colonized by ECM fungi in nature, we compared NM control aspen responses to aspen colonized by these symbionts to elucidate the capacity of aspen to respond to resource limitation and the fundamental shifts in C and P relations brought about by the two ECM symbionts.

Aspen colonized by *L. bicolor* and *P. involutus* exhibited large differences in C allocation between shoots and roots and, although the responses to  $P_i$  limitation were similar, allocation to roots differed between the symbionts. These fundamental differences may reflect differences in C demand by each partner or complex interactions between aspen roots and the two symbionts. Such differences in C allocation modulated by different ECM fungi are often noted, especially for root:shoot ratios (Karst et al. 2008), and may reflect mycorrhizal species-specific C construction and maintenance costs (Colpaert et al. 1996, Nehls and Hampp 2000, Hobbie 2006).

The two ECM fungal symbionts also differed in their influence on aspen C partitioning. Such differences in NSC partitioning may reflect differential demand and use of carbohydrates in roots, whereas CBSC responses reflect differential alleviation of  $P_i$  limitation stresses in aspen by *L. bicolor* and *P. involutus*. Taken together with patterns of growth, photosynthesis and P concentrations in tissues, it is evident that aspen colonized by *L. bicolor* responds to  $P_i$  limitation in an intermediate manner between NM plants and those colonized by *P. involutus*, and such differences may reflect different ecological niches/roles of these two fungi or unique host–fungal identity interactions.

## Conclusions

Aspen responded to  $P_i$  limitation with reductions in photosynthesis and growth, reductions in carbohydrates in leaves and increases in roots, and increases in secondary metabolite production that reflected altered C allocation and partitioning. These

changes were significantly less or not evident in aspen colonized with *L. bicolor* and *P. involutus* due to the maintenance of  $P_i$  acquisition by ECM under  $P_i$  limitation. However, aspen associated with these two symbionts exhibited fundamental differences in C allocation and partitioning regardless of growth  $P_i$  environment. Aspen colonized by *P. involutus* exhibited less perturbation to growth and tissue NSC and CBSC profiles than plants colonized by *L. bicolor*. The alleviation of these stresses was not related to P acquisition per se, but to slower growth of plants with *P. involutus* reflecting fundamental changes in C–P relations in aspen induced by this ECM fungus. The alleviation of stress responses by *L. bicolor* and *P. involutus* indicates that ECM associations play critical roles in maintaining nutrient homeostasis in aspen. However, differences in C allocation and partitioning among growth and NSC and CBSC pools indicate that ECM symbionts do not uniformly affect host  $P_i$  stress responses, and the diversity of the aspen root microbiome and ECM species-specific changes in C metabolism are important for determining the quantity and quality of C cycling in forested ecosystems.

## Supplementary Data

Supplementary Data for this article are available at *Tree Physiology* Online.

## Acknowledgments

We thank Joshua Smith for his excellent technical support.

## Conflict of interest

None declared.

## Funding

The U.S. Department of Energy (DOE) (FGO2-06ER64148).

## References

- Abdel-lateif KS, Maghrabi IA, Eldeab HA (2016) The plant natural products: their antioxidants, free radical scavengers, DNA protection and antimicrobial activities. *J Bioprocess Biotech* 6:293.
- Agerer R (2001) Exploration types of ectomycorrhizae: a proposal to classify ectomycorrhizal systems according to their patterns of differentiation and putative ecological importance. *Mycorrhiza* 11: 107–114.
- Ali MA, Louche J, Legname E, Duchemin M, Plassard C (2009) *Pinus pinaster* seedlings and their fungal symbionts show high plasticity in phosphorus acquisition in acidic soils. *Tree Physiol* 29:1587–1597.
- Alvarez M, Huygens D, Diaz LM, Villanueva CA, Heyser W, Boeckx P (2012) The spatial distribution of acid phosphatase activity in ectomycorrhizal tissues depends on soil fertility and morphotype, and relates to host plant phosphorus uptake. *Plant Cell Environ* 35:126–135.
- Batjes NH (1997) A world data set of derived soil properties by FAO/ UNESCO soil unit for global modeling. *Soil Use Manage* 1:9–16.

- Baum C, Toljander YK, Eckhardt K-U, Weih M (2009) The significance of host-fungus combinations in ectomycorrhizal symbioses for the chemical quality of willow foliage. *Plant Soil* 323:213–224.
- Bonito G, Hameed K, Ventura R, Krishnan J, Schadt CW, Vilgalys R (2016) Isolating a functionally relevant guild of fungi from the root microbiome of *Populus*. *Fungal Ecol* 22:35–42.
- Bown HE, Watt MS, Clinton PW, Mason EG, Richardson B (2007) Partitioning concurrent influences of nitrogen and phosphorus supply on photosynthetic model parameters of *Pinus radiata*. *Tree Physiol* 27:335–344.
- Boyce RL, Larson JR, Sanford RL Jr (2006) Phosphorus and nitrogen limitations to photosynthesis in Rocky Mountain bristlecone pine (*Pinus aristata*) in Colorado. *Tree Physiol* 26:1477–1486.
- Bryant JP, Chapin FS III, Klein DR (1983) Carbon/nutrient balance of boreal plants in relation to vertebrate herbivory. *Oikos* 40:357–368.
- Caretto S, Linsalata V, Colella G, Mita G, Lattanzio V (2015) Carbon fluxes between primary metabolism and phenolic pathway in plant tissues under stress. *Int J Mol Sci* 16:26378–26394.
- Casarin V, Plassard C, Hinsinger P, Arvieu JC (2004) Quantification of ectomycorrhizal fungal effects on the bioavailability and mobilization of soil P in the rhizosphere of *Pinus pinaster*. *New Phytol* 163:177–185.
- Chen F, Zhao N, Tschaplinski TJ, Liu CJ (2009) Genomics of secondary metabolism in *Populus*: interactions with biotic and abiotic environments. *Crit Rev Plant Sci* 28:375–392.
- Choi DS, Jin HO, Chung DJ, Sasa K, Koike T (2008) Growth and physiological activity in *Larix kaempferi* seedlings inoculated with ectomycorrhizae as affected by soil acidification. *Trees* 22:729–735.
- Colpaert JV, van Laere A, van Assche JA (1996) Carbon and nitrogen allocation in ectomycorrhizal and non-mycorrhizal *Pinus sylvestris* L. seedlings. *Tree Physiol* 16:787–793.
- Colpaert JN, Katiak VT, Assche VJ, van Laere A (1999) Short-term phosphorus uptake rates in mycorrhizal and non-mycorrhizal roots of intact *Pinus sylvestris* seedlings. *New Phytol* 143:589–597.
- Conjeaud C, Scheromm P, Mousain D (1996) Effects of phosphorus and ectomycorrhiza on maritime pine seedlings (*Pinus pinaster*). *New Phytol* 133:345–351.
- Courty PE, Garbaye J, Franc A (2010) Temporal and functional pattern of secreted enzyme activities in an ectomycorrhizal community. *Soil Biol Biochem* 42:2022–2025.
- Cumming JR (1993) Growth and nutrition of nonmycorrhizal and mycorrhizal pitch pine (*Pinus rigida*) seedlings under phosphorus limitation. *Tree Physiol* 13:173–187.
- Cumming JR (1996) Phosphate-limitation physiology in ectomycorrhizal pitch pine (*Pinus rigida*) seedlings. *Tree Physiol* 16:977–983.
- Cumming JR, Swiger TD, Kurnik BS, Panaccione DG (2001) Organic acid exudation by *Laccaria bicolor* and *Pisolithus tinctorius* exposed to aluminum in vitro. *Can J For Res* 31:703–710.
- Cumming JR, Zawaski C, Desai S, Collart FR (2015) Phosphorus disequilibrium in the tripartite plant ectomycorrhiza-plant growth promoting rhizobacterial association. *J Soil Sci Plant Nutr* 15:464–485.
- Desai S, Naik D, Cumming JR (2014) The influence of phosphorus availability and *Laccaria bicolor* symbiosis on phosphate acquisition, antioxidant enzyme activity, and rhizospheric carbon flux in *Populus tremuloides*. *Mycorrhiza* 24:369–382.
- Dixon RA, Paiva NL (1995) Stress-induced phenylpropanoid metabolism. *Plant Cell* 7:1085–1097.
- Donaldson JR, Kruger EL, Lindroth RL (2006) Competition-and resource-mediated tradeoffs between growth and defensive chemistry in trembling aspen (*Populus tremuloides*). *New Phytol* 169:561–570.
- Dorscheidt T (2013) Package 'MetStaT': Statistical metabolomics tools. <https://cran.r-project.org/web/packages/MetStaT/index.html>.
- Elser JJ, Bracken MES, Cleland EE et al. (2007) Global analysis of nitrogen and phosphorus limitation of primary producers in freshwater, marine and terrestrial ecosystems. *Ecol Lett* 10:1135–1142.
- Fox MD, Tackaberry LE, Drouin P, Bergeron Y, Bradley R, Massicotte HB, HYH Chen (2013) Microbial community structure of soils under four productivity classes of aspen forests in northern British Columbia. *Ecoscience* 20:264–275.
- Fransson PMA, Anderson IC, Alexander JJ (2007) Does carbon partitioning in ectomycorrhizal pine seedlings under elevated CO<sub>2</sub> vary with fungal species? *Plant Soil* 291:323–333.
- Gafur A, Schützendübel A, Langenfeld-Heysler R, Fritz E, Polle A (2004) Compatible and incompetent *Paxillus involutus* isolates for ectomycorrhiza formation in vitro with poplar (*Populus × canescens*) differ in H<sub>2</sub>O<sub>2</sub> production. *Plant Biol* 6:91–99.
- Gayler S, Grams TEE, Heller W, Treutter D, Priesack E (2008) A dynamical model of environmental effects on allocation to carbon-based secondary compounds in juvenile trees. *Ann Bot* 101:1089–1098.
- Giovannetti M, Mosse B (1980) An evaluation of techniques for measuring vesicular arbuscular mycorrhizal infection in roots. *New Phytol* 84:489–500.
- Hagerberg D, Thelin G, Wallander H (2003) The production of ectomycorrhizal mycelium in forests: relation between forest nutrient status and local mineral sources. *Plant Soil* 252:279–290.
- Hale BK, Herms DA, Hansen RC, Clausen TP, Arnold D (2005) Effects of drought stress and nutrient availability on dry matter allocation, phenolic glycosides, and rapid induced resistance of poplar to two Lymantriid defoliators. *J Chem Ecol* 31:2601–2620.
- Heinonsalo J, Pumpanen J, Rasilo T, Hurme K-R, Ilvesniemi H (2010) Carbon partitioning in ectomycorrhizal Scots pine seedlings. *Soil Biol Biochem* 42:1614–1623.
- Hetrick BAD (1991) Mycorrhizas and root architecture. *Experientia* 47:355–362.
- Hobbie EA (2006) Carbon allocation to ectomycorrhizal fungi correlates with belowground allocation in culture studies. *Ecology* 87:563–569.
- Hou E, Chen C, McGroddy ME, Wen D (2012) Nutrient limitation on ecosystem productivity and processes of mature and old-growth subtropical forests in China. *PLoS One* 12:1–12.
- Jacob C, Courbot M, Martin F, Bruna A, Chalota M (2004) Transcriptomic responses to cadmium in the ectomycorrhizal fungus *Paxillus involutus*. *FEBS Lett* 576:423–427.
- Jansen JJ, Hoefsloot HJ, van der Greef J, Timmerman ME, Westerhuis JA, Smilde AK (2005) ASCA: analysis of multivariate data obtained from an experimental design. *J Chemometrics* 19:469–481.
- Johansson EM, Fransson PMA, Finlay RD, van Hees PAW (2009) Quantitative analysis of soluble exudates produced by ectomycorrhizal roots as a response to ambient and elevated CO<sub>2</sub>. *Soil Biol Biochem* 41:1111–1116.
- Jung NC, Tamai Y (2012) Anatomical observation of polyphenol changes in epidermal cells during the development of *Quercus acutissima-Scleroderma verrucosum* ectomycorrhizae. *Trees* 26:301–310.
- Kaldorf M, Renker C, Fladung M, Buscot F (2004) Characterization and spatial distribution of ectomycorrhizas colonizing aspen clones released in an experimental field. *Mycorrhiza* 14:295–306.
- Karst J, Marczak L, Jones MD, Turkington R (2008) The mutualism-parasitism continuum in ectomycorrhizas: a quantitative assessment using meta-analysis. *Ecology* 89:1032–1042.
- Keski-Saari S, Julkunen-Tiitto R (2003) Early developmental responses of mountain birch (*Betula pubescens* subsp. *czerepanovii*) seedlings to different concentrations of phosphorus. *Tree Physiol* 23:1201–1208.
- Kirkman K, Mitchell RJ, Helton R, Drew MB (2001) Productivity and species richness across an environmental gradient in a fire-dependent ecosystem. *Am J Bot* 88:2119–2128.
- Kleczewski NM, Herms DA, Bonello P (2012) Nutrient and water availability alter belowground patterns of biomass allocation, carbon partitioning, and ectomycorrhizal abundance in *Betula nigra*. *Trees* 26:525–533.

- Kleiner KW, Raffa KF, Ellis DD, McCown BH (1998) Effect of nitrogen availability on the growth and phytochemistry of hybrid poplar and the efficacy of the *Bacillus thuringiensis* cry1A(a) d-endotoxin on gypsy moth. *Can J For Res* 28:1055–1067.
- Koricheva J, Larsson S, Haukioja E, Keinanen M (1998) Regulation of woody plant secondary metabolism by resource availability: hypothesis testing by means of meta-analysis. *Oikos* 83:212–226.
- Lamaison J-L, Polese J-M (2008) The great encyclopedia of mushrooms. HF Ullmann, Königswinter, Germany, p 240.
- LeBauer DS, Treseder KK (2008) Nitrogen limitation of net primary productivity in terrestrial ecosystems is globally distributed. *Ecology* 89:371–379.
- Leyval C, Berthelin J (1993) Rhizodeposition and net release of soluble organic compounds by pine and beech seedlings inoculated with rhizobacteria and ectomycorrhizal fungi. *Biol Fertil Soils* 15:259–267.
- Liu Q, Grace LJ, Hedley MJ, Loganathan P (2008) Effect of mycorrhizal inoculation on rhizosphere properties, phosphorus uptake and growth of pine seedlings treated with and without a phosphate rock fertilizer. *J Plant Nutr* 31:137–156.
- López-Arredondo DL, Leyva-González MA, González-Morales SI, López-Bucio J, Herrera-Estrella L (2014) Phosphate nutrition: improving low-phosphate tolerance in crops. *Annu Rev Plant Biol* 65:95–123.
- Loépez-Bucio J, Hernández-Abreu E, Sánchez-Calderón L, Nieto-Jacobo MF, Simpson J, Herrera-Estrella L (2002) Phosphate availability alters architecture and causes changes in hormone sensitivity in the Arabidopsis root system. *Plant Physiol* 129:244–256.
- Loustau D, Ben P, Brahim M, Gaudillere J, Dreyer E (1999) Photosynthetic responses to phosphorus nutrition in two-year-old maritime pine seedlings. *Tree Physiol* 19:707–715.
- Lynch JP (2011) Root phenes for enhanced soil exploration and phosphorus acquisition: tools for future crops. *Plant Physiol* 156:1041–1049.
- Makita N, Hirano Y, Yamanaka T, Yoshimura K, Kosugi Y (2012) Ectomycorrhizal-fungal colonization induces physio-morphological changes in *Quercus serrata* leaves and roots. *J Plant Nutr Soil Sci* 175: 900–906.
- Martin M, Barberis E, Celi L (1999) Determination of low concentrations of organic phosphorus in soil solution. *Commun Soil Sci Plant Anal* 30: 1909–1917.
- Mellway RD, Tran LT, Prouse MB, Campbell MM, Constabel CP (2009) The wound-, pathogen-, and ultraviolet B-responsive MY134 gene encodes an R2R3 MYB transcription factor that regulates proanthocyanidin synthesis in poplar. *Plant Physiol* 150:924–941.
- Molina R, Palmer JG, Schenck NC, Paul MN (1982) Isolation, maintenance and pure culture manipulation of ectomycorrhizal fungi. In: Schenck N (ed) *Methods and principles of mycorrhizal research*. American Phytopathological Society, St Paul, MN, pp 115–129.
- Nehls U (2008) Mastering ectomycorrhizal symbiosis: the impact of carbohydrates. *J Exp Bot* 59:1097–1108.
- Nehls U, Hampp RD (2000) Carbon allocation in ectomycorrhizas. *Physiol Mol Plant Pathol* 57:95–100.
- Ostry ME, Anderson NA, O'Brien JG (2011) Field guide to common macrofungi in eastern forests and their ecosystem functions. USDA-Forest Service General Technical Report NRS-79, Newtown Square, PA, 82 pp.
- Plassard C, Dell B (2010) Phosphorus nutrition of mycorrhizal trees. *Tree Physiol* 30:1129–1139.
- Plaxton WC, Tran HT (2011) Metabolic adaptations of phosphate-starved plants. *Plant Physiol* 156:1006–1015.
- Porter LJ, Hrstich LN, Chan BG (1985) The conversion of procyanidins and prodelphinidins to cyanidin and delphinidin. *Phytochemistry* 25: 223–230.
- Raghothama KG, Karthikeyan AS (2005) Phosphate acquisition. *Plant Soil* 274:37–49.
- Rogers A, Allen DJ, Davey PA et al. (2004) Leaf photosynthesis and carbohydrate dynamics of soybeans grown throughout their life-cycle under free-air carbon dioxide enrichment. *Plant Cell Environ* 27:449–458.
- Sanchez-Zabala J, Majada J, Martín-Rodríguez N, Gonzalez-Murua C, Ortega U, Alonso-Graña M, Arana O, Duñabeitia MK (2013) Physiological aspects underlying the improved outplanting performance of *Pinus pinaster* Ait. seedlings associated with ectomycorrhizal inoculation. *Mycorrhiza* 23:627–640.
- Schack-Kirchner H, Wilpert KV, Hildebrand EF (2000) The spatial distribution of soil hyphae in structured spruce-forest soil. *Plant Soil* 224: 195–205.
- Sharkey TD, Bernacchi CJ, Farquhar GD, Singsaas EL (2007) Fitting photosynthetic carbon dioxide response curves for C3 leaves. *Plant Cell Environ* 30:1035–1040.
- Smilde AK, Jansen JJ, Hoefsloot HCl, Lamers R-JAN, van der Greef J, Timmerman ME (2005) ANOVA-simultaneous component analysis (ASCA): a new tool for analyzing designed metabolomics data. *Bioinformatics* 21:3043–3048.
- St Clair SB, Sharpe WE, Lynch JP (2008) Key interactions between nutrient limitation and climatic factors in temperate forests: a synthesis of the sugar maple literature. *Can J For Res* 38:401–414.
- Thomas DS, Montagu KD, Conroy JP (2006) Leaf inorganic phosphorus as a potential indicator of phosphorus status, photosynthesis and growth of *Eucalyptus grandis* seedlings. *For Ecol Manage* 223:267–274.
- Vance CP, Uhde-Stone C, Allan DL (1995) Phosphorus acquisition and use: critical adaptations by plants for securing a nonrenewable resource. *New Phytol* 157:423–447.
- van Tichelen KK, Colpaert JV (2000) Kinetics of phosphate absorption by mycorrhizal and non-mycorrhizal Scots pine seedlings. *Physiol Plant* 110:96–103.
- von Uexküll HR, Mutert E (1995) Global extent, development and economic impact of acid soils. *Plant Soil* 171:1–15.
- Wallander H (2000) Uptake of P from apatite by *Pinus sylvestris* seedlings colonized by different ectomycorrhizal fungi. *Plant Soil* 218: 249–256.
- Wardle DA, Walker LR, Bardgett RD (2004) Ecosystem properties and forest decline in contrasting long-term chronosequences. *Science* 305:509–513.
- Warren CR (2011) How does P affect photosynthesis and metabolite profiles of *Eucalyptus globulus*? *Tree Physiol* 31:727–739.
- Waterhouse A (2002) Determination of total phenolics. *Curr Protoc Food Anal Chem* 11.1.1–11.1.8.
- Weiss M, Mikolajewski S, Peipp H, Schmitt U, Schmidt J, Wray V, Strack D (1997) Tissue-specific and development-dependent accumulation of phenylpropanoids in larch mycorrhizas. *Plant Physiol* 114:15–27.
- Wissuwa M, Gamat G, Ismail AM (2005) Is root growth under phosphorus deficiency affected by source or sink limitations? *J Exp Bot* 56: 1943–1950.
- Wright DP, Scholes JD, Read DJ, Rolfe SA (2000) Changes in carbon allocation and expression of carbon transporter genes in *Betula pendula* Roth. colonized by the ectomycorrhizal fungus *Paxillus involutus* (Batsch) Fr. *Plant Cell Environ* 23:39–49.
- Yin C, Pang X, Chen K (2009) The effects of water, nutrient availability and their interaction on the growth, morphology and physiology of two poplar species. *Environ Exp Bot* 67:196–203.
- Zhang Z, Liao H, Lucas WJ (2014) Molecular mechanisms underlying phosphate sensing, signaling, and adaptation in plants. *J Integr Plant Biol* 56:192–220.
- Zwanenburg G, Hoefsloot HCl, Westerhuis JA, Jansen JJ, Smilde AK (2011) ANOVA-principal component analysis and ANOVA-simultaneous component analysis: a comparison. *J Chemometrics* 25: 561–567.

## Kinetic Resolution

International Edition: DOI: 10.1002/anie.201709844  
German Edition: DOI: 10.1002/ange.201709844Double Catalytic Kinetic Resolution (DoCKR) of Acyclic *anti*-1,3-Diols: The Additive Horeau Amplification

Jérémy Merad, Prashant Borkar, Frédéric Caijo, Jean-Marc Pons, Jean-Luc Parrain, Olivier Chuzel,\* and Cyril Bressy\*

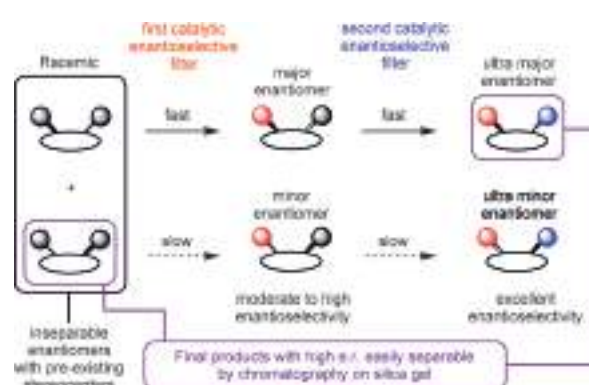
**Abstract:** The concept of a synergistic double catalytic kinetic resolution (DoCKR) as described in this article was successfully applied to racemic acyclic *anti*-1,3-diols, a common motif in natural products. This process takes advantage of an additive Horeau amplification involving two successive enantioselective organocatalytic acylation reactions, and leads to diesters and recovered diols with high enantiopurities. It was first developed with  $C_2$ -symmetrical diols and then further extended to non- $C_2$ -symmetrical *anti* diols to prepare useful chiral building blocks. The protocol is highly practical as it only requires 1 mol% of a commercially available organocatalyst and leads to easily separable products. This procedure was applied to the shortest reported total synthesis of (+)-cryptocaryalactone, a natural product with anti-germinative activity.

How can one improve the enantioselectivity outcome of a reaction on a wide scope? This question arises during the development of any given catalytic enantioselective transformation. The indispensable optimization stage improves the enantiomeric ratio (e.r.) of a reaction through the variations of the chemical and/or physical parameters of the transformation. Usually, e.r. enhancement is rapidly accompanied by a narrowing of the reaction scope. Most of the time, the rational design of the catalyst structure is the only option to improve reactivity and selectivity. This fine-tuning is nonetheless time consuming because of the difficulty of considering all the parameters involved in the enantiodetermining transition state, even though it can result in negligible improvements.

In contrast, the Horeau principle<sup>[1]</sup> is responsible for the improvement of enantioselectivity in some reactions which rely on polyfunctionalized substrates. By applying at least two identical successive enantioselective transformations, the second reaction can act as an additional stereocontrolling filter to improve the enantiopurity of the final product. Since the pioneering works of Horeau in the 70's, such amplification of enantioselectivity was observed in several catalytic trans-

formations.<sup>[2,3,5e]</sup> In enantioselective catalysis, the Horeau amplification can be divided into two main categories:

- 1) In the subtractive Horeau amplification, the minor enantiomer obtained after the first transformation is the substrate of the second transformation. The polyfunctionalized substrates involved in this first category are either prochiral<sup>[3,4]</sup> or *meso* compounds.<sup>[3,5]</sup>
- 2) In the additive Horeau amplification, the major enantiomer formed after the first reaction is rapidly consumed in the second enantioselective (or diastereoselective) transformation.<sup>[6]</sup> However, in contrast to the subtractive processes, examples of additive amplifications involving starting materials with pre-existing stereocenters are extremely scarce (Scheme 1).<sup>[7]</sup>



**Scheme 1.** Additive Horeau amplification applied to substrates bearing pre-existing stereocenters.

Although observed many times, the Horeau amplification is still considered an anecdotal phenomenon. By considering the synthetic potential supported by the Horeau principle in enantioselective catalysis, we supposed that this concept could be used as a synthetic strategy. Indeed, it could constitute an alternative approach to laborious catalyst fine-tuning while keeping high enantioselectivities and broad reaction scopes. In practice, the syntheses designed on this principle would require minimal optimization and remain effective with moderately selective catalysts. To validate this hypothesis we identified the double catalytic kinetic resolution (DoCKR) of acyclic *anti*-1,3-diols as a relevant transformation, complementary to our previous study.<sup>[5d]</sup> Indeed, this widespread stereodefined scaffold is, to a large extent, responsible for the biological activity of numerous polyketides such as dictyostatin, ripostatin B, fostriecin, and peluroside A.<sup>[8]</sup> Consequently, the control of relative and

[\*] Dr. J. Merad, Dr. P. Borkar, Prof. Dr. J.-M. Pons, Dr. J.-L. Parrain, Dr. O. Chuzel, Prof. Dr. C. Bressy  
Aix Marseille Université, CNRS, Centrale Marseille, iSm2  
Marseille (France)  
E-mail: olivier.chuzel@univ-amu.fr  
cyril.bressy@univ-amu.fr

Dr. F. Caijo  
DemetaSAS  
6 rue Pierre Joseph Colin, Biopole, 35500 Rennes (France)

Supporting information and the ORCID identification number(s) for the author(s) of this article can be found under:  
<https://doi.org/10.1002/anie.201709844>.



**Table 1:** DoCKR of C<sub>2</sub>-symmetrical 1,3-diols.<sup>[a]</sup>

Entry	rac-1	Yield [%] <sup>[b]</sup> (e.r.) <sup>[c]</sup> Diol <sup>[e]</sup>	Diester <sup>[e]</sup>	s <sup>[d]</sup>
1		40 <sup>[f]</sup> (98.4:1.6)	41 <sup>[f]</sup> (99.3:0.7)	28
2		40 (97.6:2.4)	40 (98.9:1.1)	16
3		43 (> 99.9:0.1)	44 (99.6:0.4)	51
4		40 (97.1:2.9)	44 (98.3:1.7)	15
5		46 (98.7:1.3)	46 (98.1:1.9)	46
6		44 (> 99.9:0.1)	40 (99.9:0.1)	60
7		43 (> 99.9:0.1)	42 (97.4:2.6)	51
8		45 (> 99.9:0.1)	45 (98.6:1.4)	73
9 <sup>[g]</sup>		21 (99.5:0.5)	19 (61.2:38.8)	7

[a] Typical experiment performed on 0.5 mmol of the racemic diol under the standard reaction conditions. [b] Yield of isolated product.

[c] Determined by HPLC analysis using a stationary chiral phase; for details see the Supporting Information. [d] Based on recovered diol.

[e] d.r. > 20:1 in all cases. [f] Run on 3.5 g of racemic diol with 0.5 mol % of catalyst. [g] Monoester was also produced in 50% yield and 70.6:29.4 e.r..

allylic or benzylic positions (Table 1). Excellent results were obtained for both allylic diols (**1a–d**) and benzylic diols (**1e–h**) series. Indeed, diols were recovered in 40–46% yield in enantiopure form in many cases, and correspond to excellent *s* values between 15 and 73. Similar results were obtained for the diesters with yields greater than 40% and e.r. values of greater than 97:3. Because of the symmetry of the substrates, it does not matter which hydroxy group undergoes the first acylation. It seems reasonable to propose that the two successive acylation reactions on one enantiomer of the *anti*-1,3-diol occur approximately at the same kinetic rate. The efficiency and the scalability of this new method were demonstrated by running the reaction with racemic **1a** on a 3.5 gram scale. Optically active (*R,R*)-**1a** (1.40 g) and (*S,S*)-**2a** (2.03 g) were obtained with comparable excellent yields and selectivities using a reduced amount of catalyst (0.5 mol %; entry 1). To discover the limits of the reaction, we examined the DoCKR of a diol without a  $\pi$ -system nearby the reactive centers (entry 9). Racemic yashabushidiol was tested under the standard reaction conditions, thus giving a monoester and the corresponding diester with poor enantioselectivity, but the recovered diol in 21% yield with a very high e.r. value (> 99:1).

We expected that a significant step forward would be accomplished in terms of synthetic potential if this method-

ology was applicable to unsymmetrical *anti*-1,3-diols. In such cases, the rates of the two successive acylation reactions might be significantly different, thus leading to a more complex kinetic sorting. Different series of substrates were prepared and evaluated in acylative DoCKR: diversely substituted *anti*-hepta-1,6-dien-3,5-diols (**1i–k**), *anti*-1,3-diarylpropan-1,3-diols (**1l–n**), and *anti*-1,5-diaryl-pent-1-en-3,5-diols (**1o–s**; Table 2). With these three series, *s* values between 18 and 79 were obtained. High levels of enantioselectivity were reached with comparable yields for both the recovered diols and the diesters. The transformation tolerates heterocycles such as furan or thiophene derivatives (entries 5, 6, and 11), as well as trisubstituted double bonds (entries 2, 3, 9, and 10). Finally the DoCKR of the *anti*-1,3-diol **1t**, presenting one benzylic alcohol and one secondary hydroxy group without a proximal  $\pi$ -system (e.g. in either the allylic or benzylic position), was examined. The enantioselectivity of the recovered diol was not affected by this structural change and remained at a high level (99.5:0.5 e.r.), whereas the e.r. value of its diester was

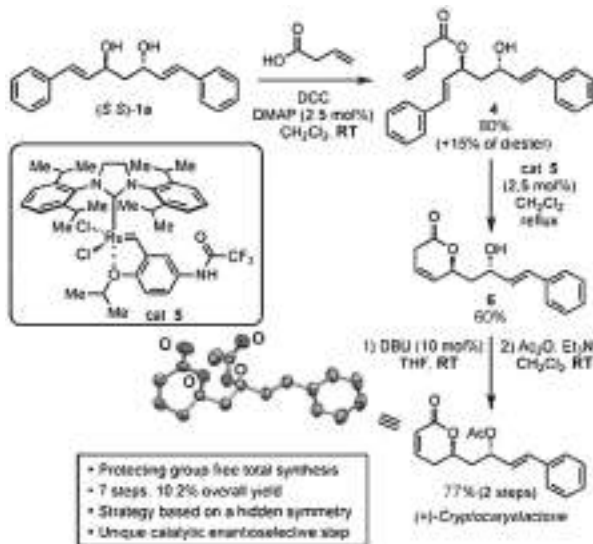
**Table 2:** DoCKR of non-C<sub>2</sub>-symmetrical 1,3-diols.<sup>[a]</sup>

Entry	rac-1	Yield [%] <sup>[b]</sup> (e.r.) <sup>[c]</sup> Diol <sup>[e]</sup>	Diester <sup>[e]</sup>	s <sup>[d]</sup>
1		38 (99.7:0.3)	43 (95.8:4.2)	22
2		38 (99.7:0.3)	43 (98.0:2.0)	22
3		34 (> 99.9:0.1)	33 (88.5:11.5)	21
4		41 (97.7:2.3)	47 (96.5:3.5)	18
5		43 (99.1:0.9)	47 (98.5:1.5)	30
6		49 (97.4:2.6)	38 (98.2:1.8)	79
7		39 (99.9:0.1)	40 (98.2:1.8)	29
8		39 (99.7:0.3)	43 (96.2:3.8)	24
9		40 (99.6:0.4)	40 (97.9:2.1)	25
10		41 (> 99.9:0.1)	43 (98.4:1.6)	39
11		36 (> 99.9:0.1)	38 (90.3:9.7)	24
12		41 (99.5:0.5)	37 (86.9:13.1)	27

[a] Typical experiment performed on 0.5 mmol of racemic diol under the standard reaction conditions. [b] Yield of isolated product. [c] Determined by HPLC analysis using a chiral stationary phase; for details see the Supporting Information. [d] Based on recovered diol. [e] d.r. > 20:1 in all cases.

slightly lower. Its  $s$  value (27 for **1t**) was quite similar to the unsaturated precursor **1o** ( $s = 29$ ). This last example pinpoints the potential of the DoCKR process, to overcome a challenging selective transformation.

We decided to apply this methodology to the total synthesis of (+)-cryptocaryalactone,<sup>[15]</sup> a natural germination inhibitor (Scheme 5). The acylation reaction of the virtually



**Scheme 5.** Total synthesis of (+)-cryptocaryalactone. DBU = 1,8-diazabicyclo[5.4.0]undec-7-ene, DCC = *N,N*-dicyclohexylcarbodiimide, DMAP = 4-(*N,N*-dimethylamino)pyridine, THF = tetrahydrofuran.

enantiopure (*S,S*)-**1a** with vinylacetic acid under classical reaction conditions (DCC, DMAP cat.,  $\text{CH}_2\text{Cl}_2$ , RT) gave the monoester **4** (80%) accompanied by a small amount of diester (15%). The formed triene **4** then underwent a ring-closing metathesis reaction, using the highly active catalyst **5**,<sup>[16]</sup> to afford the lactone **6**. Migration of the internal double bond under DBU catalysis<sup>[17]</sup> and subsequent acylation reaction afforded (+)-cryptocaryalactone.<sup>[18]</sup> This hidden-symmetry strategy<sup>[19]</sup> represents the shortest synthesis of this target reported to date.<sup>[20]</sup> Additionally, no protecting group was required for this synthesis,<sup>[21]</sup> which involved a unique organocatalytic enantioselective step.<sup>[22]</sup>

In conclusion, we described a highly enantioselective synthetic separation of acyclic *anti*-1,3-diols, which are ubiquitous structural motifs in nature. This development was made possible by the design of a synergistic double catalytic kinetic resolution (DoCKR) and by a full exploitation of the additive Horeau principle. This efficient, general, and scalable method using an organocatalyzed acylation (0.5–1 mol% catalyst loading) gives easy access to both enantiomers of a given acyclic *anti*-1,3-diol with high yields and enantioselectivities. The methodology was successfully applied to  $\text{C}_2$ -symmetrical substrates and then further extended to the challenging and unprecedented cases of non- $\text{C}_2$ -symmetrical *anti*-1,3-diols. To the best of our knowledge, the use of such nonsymmetrical substrates bearing pre-existing stereocenters in amplified systems has not yet been reported.

Finally, the effectiveness of the DoCKR was applied to an efficient total synthesis of (+)-cryptocaryalactone using a single catalytic enantioselective step. This flexible approach leads to both enantiomers, which are useful in total synthesis of natural product containing stereocenters with unassigned absolute configuration. All in all, we strongly believe that the concept of DoCKR could be of broader utility for the synthetic community and potentially transposed to other bifunctional substrates.

## Acknowledgements

The authors warmly acknowledge Dr. X. Bugaut (AMU, iSm2) for proof reading, Dr. N. Vanthuyne, M. Jean (HPLC, iSm2), and Dr. M. Giorgi (RX, Spectropole, FR 1739). Aix Marseille Université (AMU), CNRS, COST ORCA Action 0905 (Organocatalysis), the French Research Ministry (Grant to J.M.) and Agence Nationale de la Recherche (Orcademe project ANR-10-JCJC-0710, Grant to P.B.) are also gratefully acknowledged for funding.

## Conflict of interest

The authors declare no conflict of interest.

**Keywords:** diols · enantioselectivity · kinetic resolution · natural products · organocatalysis

**How to cite:** *Angew. Chem. Int. Ed.* **2017**, *56*, 16052–16056  
*Angew. Chem.* **2017**, *129*, 16268–16272

- [1] J.-P. Vigneron, M. Dhaenes, A. Horeau, *Tetrahedron* **1973**, *29*, 1055.
- [2] V. Rautenstrauch, *Bull. Soc. Chim. Fr.* **1994**, *131*, 515.
- [3] For review, see: D. S. Glueck, *Catal. Sci. Technol.* **2011**, *1*, 1099.
- [4] Selected examples: a) S. L. Schreiber, T. S. Schreiber, D. B. Smith, *J. Am. Chem. Soc.* **1987**, *109*, 1525; b) A. C. Spivey, S. J. Woodhead, M. Weston, B. I. Andrews, *Angew. Chem. Int. Ed.* **2001**, *40*, 769; *Angew. Chem.* **2001**, *113*, 791; c) K. Mori, Y. Ichikawa, M. Kobayashi, Y. Shibata, M. Yamanaka, T. Akiyama, *J. Am. Chem. Soc.* **2013**, *135*, 3964; d) R. J. Armstrong, M. D. Smith, *Angew. Chem. Int. Ed.* **2014**, *53*, 12822; *Angew. Chem.* **2014**, *126*, 13036; e) T. Osako, Y. Uozumi, *Org. Lett.* **2014**, *16*, 5866; f) S. Tuong, A. Limouni, Q. Wang, M.-X. Wang, J. Zhu, *Angew. Chem. Int. Ed.* **2017**, *56*, 14192; *Angew. Chem.* **2017**, *129*, 14380.
- [5] Selected examples: a) B. S. Lucas, S. D. Burke, *Org. Lett.* **2003**, *5*, 3915; b) V. B. Birman, H. Jiang, X. Li, *Org. Lett.* **2007**, *9*, 3237; c) C. Roux, M. Candy, J.-M. Pons, O. Chuzel, C. Bressy, *Angew. Chem. Int. Ed.* **2014**, *53*, 766; *Angew. Chem.* **2014**, *126*, 785; d) J. Merad, P. Borkar, T. Bouyon Yenda, C. Roux, J.-M. Pons, J.-L. Parrain, O. Chuzel, C. Bressy, *Org. Lett.* **2015**, *17*, 2118; for a review in the context of total synthesis: e) J. Merad, M. Candy, J.-M. Pons, C. Bressy, *Synthesis* **2017**, *49*, 1938.
- [6] Selected examples: *Alkenes*: a) G. A. Crispino, P. T. Ho, K. B. Sharpless, *Science* **1993**, *259*, 64; b) S. El Baba, K. Sartor, J.-C. Poulin, H. B. Kagan, *Bull. Soc. Chim. Fr.* **1994**, *131*, 525; c) Y. Huang, A. M. Walji, C. H. Larsen, D. W. C. MacMillan, *J. Am. Chem. Soc.* **2005**, *127*, 15051; d) J. Zhou, J. W. Ogle, Y. Fan, V. Banphavichit, Y. Zu, K. Burgess, *Chem. Eur. J.* **2007**, *13*, 7162; e) N. J. Green, A. L. Lawrence, G. Bojase, A. L. Willis, M. N.

- Paddon-Row, M. S. Sherburn, *Angew. Chem. Int. Ed.* **2013**, *52*, 8333; *Angew. Chem.* **2013**, *125*, 8491; *Ketones*: f) M. Kitamura, T. Ohkuma, S. Inoue, N. Sayo, H. Kumobayashi, S. Akutagawa, T. Ohta, H. Takaya, R. Noyori, *J. Am. Chem. Soc.* **1988**, *110*, 629; g) A. K. Dilger, V. Gopalasamuthiram, S. D. Burke, *J. Am. Chem. Soc.* **2007**, *129*, 16273; h) Y. Lu, I. S. Kim, A. Hassan, D. J. Del Vall, M. J. Krische, *Angew. Chem. Int. Ed.* **2009**, *48*, 5018; *Angew. Chem.* **2009**, *121*, 5118; *Enolates*: i) J. A. Enquist, Jr., B. M. Stoltz, *Nature* **2008**, *453*, 1228.
- [7] a) J. C. Ruble, J. Tweddell, G. Fu, *J. Org. Chem.* **1998**, *63*, 2794; b) P. Kumar, P. S. Chowdhury, M. Pandey, *Adv. Synth. Catal.* **2013**, *355*, 1719.
- [8] For a review, see: a) D. Herkommer, B. Schmalzbauer, D. Menche, *Nat. Prod. Rep.* **2014**, *31*, 456; b) M. Kretschmer, D. Menche, *Synlett* **2010**, 2989; c) K.-S. Yeung, I. Paterson, *Chem. Rev.* **2005**, *105*, 4237.
- [9] For a review, see: S. E. Bode, M. Wolberg, M. Müller, *Synthesis* **2006**, 557.
- [10] For the two major reductive methods, see: a) D. A. Evans, K. T. Chapman, E. M. Carreira, *J. Am. Chem. Soc.* **1988**, *110*, 3560; b) D. A. Evans, A. H. Hoveyda, *J. Am. Chem. Soc.* **1990**, *112*, 6447.
- [11] Aldol-Tischenko process : a) C. M. Mascarenhas, S. P. Miller, P. S. White, J. P. Morken, *Angew. Chem. Int. Ed.* **2001**, *40*, 601; *Angew. Chem.* **2001**, *113*, 621; b) V. Gnanadesikan, Y. Horiuchi, T. Ohshima, M. Shibasaki, *J. Am. Chem. Soc.* **2004**, *126*, 7782; Dynamic process: c) B. Martín-Matute, M. Edin, J.-E. Bäckvall, *Chem. Eur. J.* **2006**, *12*, 6053.
- [12] For reviews on non-enzymatic catalytic KR, see: a) R. Gurubrahamam, Y.-S. Cheng, W.-Y. Huang, K. Chen, *ChemCatChem* **2016**, *8*, 86–96; b) H. Pellissier, *Catalytic Kinetic Resolution*, in *Separation of Enantiomers: New Methods and Applications* (Ed.: M. Todd), Wiley-VCH, Weinheim, **2014**, Chap. 3, pp. 75–122; c) S. Arseniyadis, A. Spivey, *Regio- and Position Selective Reactions and Desymmetrizations in Comprehensive Enantioselective Organocatalysis, Vol. 3* (Ed.: P. I. Dalko), Wiley-VCH, Weinheim, **2013**, Chap. 41, pp. 1225–1284; d) C. Müller, P. R. Schreiner, *Angew. Chem. Int. Ed.* **2011**, *50*, 6012; *Angew. Chem.* **2011**, *123*, 6136; e) H. Pellissier, *Adv. Synth. Catal.* **2011**, *353*, 1613.
- [13] a) C. Joannesse, C. P. Johnston, C. Concellon, C. Simal, D. Philp, A. D. Smith, *Angew. Chem. Int. Ed.* **2009**, *48*, 8914; *Angew. Chem.* **2009**, *121*, 9076; for reviews on chiral isothioureas as organocatalysts, see: b) J. Merad, J.-M. Pons, O. Chuzel, C. Bressy, *Eur. J. Org. Chem.* **2016**, 5589 and also c) V. B. Birman, *Aldrichimica Acta* **2016**, *49*, 23.
- [14] H. B. Kagan, J.-C. Fiaud, *Top. Stereochem.* **1988**, *18*, 249.
- [15] Isolation: a) T. R. Govindachari, P. C. Parthasarathy, J. D. Modi, *Ind. J. Chem.* **1972**, *10*, 149; b) G. F. Spencer, R. E. England, R. B. Wolf, *Phytochemistry* **1984**, *23*, 2499–2500.
- [16] H. Clavier, F. Caijo, E. Borré, D. Rix, F. Boeda, S. P. Nolan, M. Mauduit, *Eur. J. Org. Chem.* **2009**, 4254–4265. Unlike catalyst **5**, classical metathesis catalysts lead to a mixture of products for this transformation.
- [17] M.-A. Virolleaud, C. Bressy, O. Piva, *Tetrahedron Lett.* **2003**, *44*, 8081–8084.
- [18] CCDC 1440921 contains the supplementary crystallographic data for this paper. These data can be obtained free of charge from The Cambridge Crystallographic Data Centre.
- [19] For the total synthesis of natural products, involving an economic use of chiral reagents, from our group, see: a) M. Candy, G. Audran, H. Bienaymé, C. Bressy, J.-M. Pons, *J. Org. Chem.* **2010**, *75*, 1354–1359; b) M. Candy, L. Tomas, S. Parat, V. Heran, H. Bienaymé, J.-M. Pons, C. Bressy, *Chem. Eur. J.* **2012**, *18*, 14267–14271 and ref. [5d].
- [20] Previous syntheses: a) H. H. Meyer, *Liebigs Ann. Chem.* **1984**, 977–981 (> 9 steps); b) Y. Mori, H. Furukawa, *Chem. Pharm. Bull.* **1994**, *42*, 2161–2163 (> 16 steps); c) G. Sabitha, V. Bhaskar, S. S. S. Reddy, J. S. Yadav, *Tetrahedron* **2008**, *64*, 10207–10213 (> 13 steps); d) P. R. Krishna, K. Lopinti, K. L. N. Reddy, *Beilstein J. Org. Chem.* **2009**, *5*, 14 (> 11 steps); e) G. Sabitha, B. Vangala, S. S. S. Reddy, J. S. Yadav, *Helv. Chim. Acta* **2010**, *93*, 329–338 (16 steps); f) P. Balasubramanyam, G. C. Reddy, N. Salvanna, B. Das, *Synthesis* **2011**, 3706–3710 (12 steps); g) J. S. Yadav, D. C. Bhunia, B. Ganganna, *Tetrahedron Lett.* **2012**, *53*, 2496–2499 (9 steps).
- [21] For reviews, see: a) R. N. Saicic, *Tetrahedron* **2014**, *70*, 8183–8218; b) I. S. Young, P. S. Baran, *Nat. Chem.* **2009**, *1*, 193–205; c) R. W. Hoffmann, *Synthesis* **2006**, 3531–3541.
- [22] For reviews about total syntheses involving an enantioselective organocatalysis, see: a) M. E. Abbasov, D. Romo, *Nat. Prod. Rep.* **2014**, *31*, 1318–1327; b) E. Marqués-López, R. P. Herrera, M. Christmann, *Nat. Prod. Rep.* **2010**, *27*, 1138–1167; c) R. M. de Figueiredo, M. Christmann, *Eur. J. Org. Chem.* **2007**, 2575–2600.

Manuscript received: September 22, 2017

Accepted manuscript online: October 11, 2017

Version of record online: November 15, 2017

# Microwave Assisted Fast Synthesis of CuO Nanoflakes: Catalytic Application in the Synthesis of 1,4-Dihydropyridine

S.D. BAJAJ<sup>a</sup>, P.V. TEKADE<sup>a,\*</sup>, G.V. LAKHOTIYA<sup>b</sup> AND P.G. BORKAR<sup>a</sup>

<sup>a</sup>Department of Chemistry, Jankidevi Bajaj College of Science, Jammalal Bajaj Marg, Civil Lines, Wardha-442001, India

<sup>b</sup>Department of Physics, Jankidevi Bajaj College of Science, Jammalal Bajaj Marg, Civil Lines, Wardha-442001, India

(Received 13 October 2016; in final form 12 April 2017)

CuO nanoflakes were successfully synthesized by microwave irradiation, using copper(II) sulphate and sodium hydroxide (NaOH) as the starting materials and ethanol as the solvent. The CuO nanoflakes were characterized by using techniques such as X-ray powder diffraction, field emission scanning electron microscopy, and UV-visible absorption spectroscopy, Fourier transform infra-red spectroscopy. The synthesized CuO nanoflakes were found to have morphology like nanoflakes with narrow size distribution and high purity. Moreover, the synthesized CuO nanoflakes were used as an efficient catalyst for synthesis of a series of dihydropyridine derivatives. Optimization studies with different catalysts and solvents reveal that CuO nanoparticle in the water/ethanol mixture is efficient catalyst/solvent system for the synthesis of dihydropyridine derivative.

DOI: [10.12693/APhysPolA.132.1294](https://doi.org/10.12693/APhysPolA.132.1294)

PACS/topics: microwave irradiation, CuO nanoflakes, catalyst, dihydropyridine

## 1. Introduction

In recent years, application of nanoparticles as a catalyst in organic synthesis gained considerable attention because they are reusable and removable from the reaction medium by simple filtration. Moreover, nanocatalysts reported to have high efficiency owing to their large surface to volume ratio, which increases their catalytic activity. Likewise, the supported magnetic nanocatalysts are of considerable interest in organic synthesis because they are feasible alternatives to conventional catalysts, readily obtainable, easily separable by an external magnet and high degree of chemical stability in most of the organic and inorganic solvents [1–10]. The dihydropyridine derivatives are one of the important heterocyclic ring systems because of their extensive pharmacological properties and they are also analogues of NADH coenzymes. Moreover, the dihydropyridyl compounds possess a wide range of biological activity and medicinal properties e.g. smooth muscle selective, antihistamines, cardioselective. The dihydropyridines is a topic of interest for study because they have fascinating heterocyclic nucleus with multiple reaction centers [11, 12].

Furthermore, cytotoxic activity of 4-substituted phenyl dihydropyridines against human oral squamous carcinoma is an important aspect. The well known dihydropyridine compounds such as nifedipine, nitrendipine and nimodipine [13, 14] were reported as commercially useful molecules which are calcium channel blockers. Consequently, a variety of potential drugs are available for the treatment of congestive heart failure [15, 16] and neuroprotective agent [17] which possesses dihydropyridine

nucleus. In addition, various medicinal applications viz. antihypertensive, hepatoprotective, bronchodilators, geroprotective, antiatherosclerotic, antitumour, antiplatelet, antimutagenic, antidiabetic, and aggregation activity were shown by some of the dihydropyridine derivatives [18–21]. These compounds were also found as potential calcium channel blockers in medicinal and bioorganic chemistry [22] and NADH models [23], respectively. Moreover, the 1,4-dihydropyridines also acts as a flexible intermediate in the synthesis of natural products owing to their higher reactivity [24].

Consequently, various synthetic methods were developed owing to a wide range of biological medicinal and pharmacological importance of dihydropyridine derivatives. Some of the synthetic methods are use of microwave irradiation technique [25, 26], refluxing at high temperature [27–31], use of ionic liquid [32], use of catalysts like SiO<sub>2</sub>/HClO<sub>4</sub> [33], SiO<sub>2</sub>/NaHSO<sub>4</sub> [34], I [35], bakers' yeast [36], metal triflates [37], tetrabutylammonium hydrogen sulfate [38], organocatalysts [39], PTSA [40], iron trifluoroacetate [41], TMSCl [42] and Ni nanoparticles [43].

Literature survey reveals that various synthetic methodology for synthesis of 1,4-dihydropyridine derivatives possesses some disadvantages such as costly reagents, lengthy work-up procedures, moisture sensitivity, toxic and harsh reaction conditions. Therefore, development of fast and efficient methodology with an efficient, green solvent/catalyst system for the synthesis of 1,4-dihydropyridine is an important challenge for organic chemists.

Therefore, it is a topic of interest to synthesize nanoparticles with high surface area and to focus their catalytic application in organic synthesis [44–48]. Therefore, we reported herein CuO nanoflakes as a efficient

\*corresponding author; e-mail: [pradiptekade@gmail.com](mailto:pradiptekade@gmail.com)

catalyst for the synthesis of 1,4-dihydropyridine derivatives through one-pot four-component Hantzsch condensation reaction using aromatic aldehyde, ethyl acetoacetate/methyl acetoacetate and ammonium acetate in ethanol as solvent, in excellent yield utilizing microwave assisted technology. The novelty of this proposed method lies in the use of ethanol as a green, less toxic solvent, low-cost catalyst (synthesized in laboratory with readily available starting materials) and simple synthetic methodology, mild reaction conditions, high yields, simple work-up, easy filtration and reusability of catalyst.

## 2. Experimental

### 2.1. General

All solvents, chemicals and reagents procured from Merck and Sigma Aldrich. Melting points were determined on Digital Melting Point apparatus and are uncorrected. The field emission scanning electron microscopy (FESEM) images were obtained on a Seron AIS 2100. The Fourier transform infrared (FT-IR) spectra were recorded on a Bruker alpha FTIR spectrometer and UV-vis spectroscopy was studied on Shimadzu 1800 setup at J.B. Science College, Wardha. The  $^1\text{H}$  NMR spectra were recorded on Bruker DRX-300 Avance spectrometer at 300.13 MHz at SAIF, Chandigarh, Punjab University, and Punjab. The elemental analyses were done with an Elemental Analyser system at SAIF, Chandigarh, Punjab University, and Punjab. All the reagents used in this synthesis are of analytical grade and used without further purification. The X-ray diffraction (XRD), FESEM analyses were carried out at SAIF, IIT Bombay. BET surface area analysis was studied at Material Science Center, IIT Kharapur.

### 2.2. CuO nanomaterial preparation

25 ml ethanolic solution of 0.5 M  $\text{CuSO}_4 \cdot 5\text{H}_2\text{O}$  (copper(II) sulfate 5-hydrate, 99.95%) stirred for 5 min on magnetic stirrer and 25 ml ethanolic solution of 0.5 M NaOH added dropwise to the ethanolic solution of copper sulphate with vigorous stirring for about 15 min. The resulting mixture placed in the scientific microwave oven with the specification of 650 W for about 10 min. During the reflux the change in color of the solution varies from sky blue to colorless and then slowly turns to brick red. This indicates the formation of CuO nanomaterial. The solution were cooled to room temperature and the obtained precipitate was centrifuged, washed first with distilled water and then with absolute ethanol and with acetone in sequence and dried in oven at  $100^\circ\text{C}$  for 3 h. The final product was collected and used for characterization.

### 2.3. Synthesis of diethyl 2,6-dimethyl-4-(4-nitrophenyl)-1,4-dihydropyridine-3,5-dicarboxylate

A mixture of an aromatic aldehyde (1 mmol), ethyl acetoacetate (2 mmol), and ammonium acetate

(1.3 mmol) and copper oxide nanoflakes (CuO), vigorously agitated in water (2 mL) at  $70^\circ\text{C}$  for the stipulated period of time, till the completion of the reaction (checked by TLC). After completion of the reaction, few drops of ethanol were added to the reaction mixture (to assist granulation of the products). The catalyst, being insoluble in ethanol/water, was separated by centrifugation. The catalyst was removed by filtration and the filtrate was added to crushed ice. A solid product was obtained, which was filtered, washed with water, and crystallized from aqueous ethanol, if needed (Fig. 1).

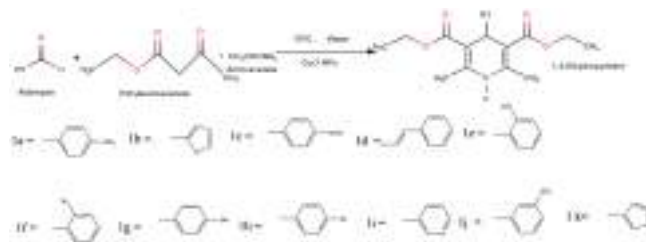


Fig. 1. Scheme of one pot four component synthesis of 1,4-dihydropyridine.

### 2.4. Recycling of catalyst

To examine the reusability, the catalyst was recovered by filtration from the reaction mixture after dilution with ethanol, washed with methanol, and reused as such for subsequent experiments (up to three cycles) under similar reaction conditions. The observed fact that yields of the product remained comparable in these experiments established (Table I) the recyclability and reusability of the catalyst without any significant loss of activity.

TABLE I  
Recyclability of catalyst.

Number of cycle	% Yield
1st	93
2nd	90
3rd	89

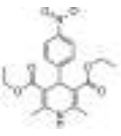
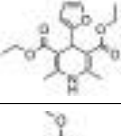
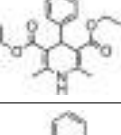
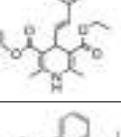
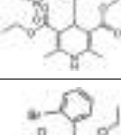
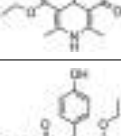
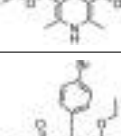
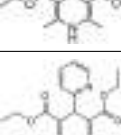
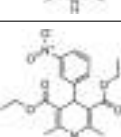
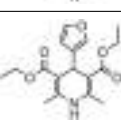
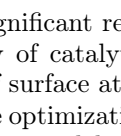
### 2.5. Optimization studies of synthesis of 1,4-dihydropyridine

In the present work, the reaction conditions optimized with respect to the catalyst, solvent and reactants for carbon-carbon (C-C) and carbon-heteroatom (C-N) bond formation. The physical characterization is given in Table II.

In continuation of this research, the reaction conditions were optimized on the basis of the catalyst, solvent and reactants for carbon-carbon and carbon-heteroatom bond formation. To test the efficiency of the catalytic activity, we chose to focus our initial studies on the cyclization reaction of aldehydes, ammonium acetate and ethylacetoacetate in the presence of different catalysts such as  $\text{Al}_2\text{O}_3$ ,  $\text{TiO}_2\text{SiO}_2$ , CuO and also in the presence of regular CuO (purchased from Sigma Aldrich).

TABLE II

Physical characterization of the synthesized compounds.

SN	Code	Structure	M.F.	M.W.	Time [min]	M.P [°C]	Yield [%]	$R_f$
1	1a		C <sub>19</sub> H <sub>22</sub> N <sub>2</sub> O <sub>6</sub>	374.38	120	169 ÷ 171	93	0.54
2	1b		C <sub>17</sub> H <sub>21</sub> NO <sub>5</sub>	319.35	115	165 ÷ 168	90	0.57
3	1c		C <sub>20</sub> H <sub>25</sub> NO <sub>5</sub>	359.41	100	160 ÷ 162	85	0.65
4	1d		C <sub>21</sub> H <sub>25</sub> NO <sub>4</sub>	355.43	105	223 ÷ 225	85	0.70
5	1e		C <sub>19</sub> H <sub>22</sub> N <sub>2</sub> O <sub>6</sub>	374.38	105	172 ÷ 174	75	0.65
6	1f		C <sub>19</sub> H <sub>22</sub> BrNO <sub>4</sub>	408.29	95	210 ÷ 213	65	0.65
7	1g		C <sub>19</sub> H <sub>23</sub> NO <sub>5</sub>	345.39	80	241 ÷ 242	93	0.60
8	1h		C <sub>19</sub> H <sub>22</sub> BrNO <sub>4</sub>	408.29	95	210 ÷ 213	65	0.65
9	1i		C <sub>18</sub> H <sub>22</sub> N <sub>2</sub> O <sub>4</sub>	330.38	60	211 ÷ 212	90	0.60
10	1j		C <sub>19</sub> H <sub>22</sub> N <sub>2</sub> O <sub>6</sub>	374.39	102	223 ÷ 225	88	0.70
11	1k		C <sub>17</sub> H <sub>21</sub> NO <sub>5</sub>	319.35	115	165 ÷ 168	90	0.57

The significant results of Table III corresponds to the reactivity of catalytic nanoparticles determined by the energy of surface atoms on surface of nanoparticle.

For the optimization of the reaction conditions, we proceeded the model reaction using CuO nanoparticles in various solvents.

TABLE III

One-pot synthesis of diethyl 2,6-dimethyl-4-(4-nitrophenyl)-1,4-dihydropyridine-3,5-dicarboxylate in various catalysts.

Entry	Catalyst	Time [min]	Yields <sup>a</sup> [%]
1	SiO <sub>2</sub>	100	35
2	Al <sub>2</sub> O <sub>3</sub>	120	50
3	TiO <sub>2</sub>	140	70
4	CuO	160	60
5	CuONps	120	85–90

<sup>a</sup>isolated yields

TABLE IV

One-pot synthesis of diethyl 2,6-dimethyl-4-(4-nitrophenyl)-1,4-dihydropyridine-3,5-dicarboxylate in various solvents<sup>a</sup>.

Entry	Solvent	Time [min]	Yields [%] <sup>b</sup>
1	toluene	240	35
2	acetonitrile	180	50
3	ethanol	120	70
4	ethanol/water mixture (30:70)	140	80–90

<sup>a</sup>reflux conditions, <sup>b</sup>isolated yields.

The results in Table IV show that a mixture of water/ethanol is the most efficient solvent for this multi-component reaction. This is not surprising, insight of the fact that the hydrogen bonding between water/ethanol and the substrate can promote the nucleophilic attack of the reactants.

### 3. Results and discussion

The CuO nanocatalyst was synthesized by a modified precipitation method in which the reaction was carried out under scientific microwave oven using an ethanol/water mixture (30:70) as a green medium. Then, it was characterized by powder X-ray diffraction (PXRD), scanning electron microscopy (SEM), and FTIR spectral analysis. The SEM analysis was done to study particle size and the CuO nanoparticle morphology was identified based on the analysis of SEM images.

#### 3.1. Characterization of CuO nanoparticles

##### 3.1.1. XRD

The structural property of as-synthesized CuO nanomaterial is analyzed by the powder XRD. Figure 2 illustrates the XRD patterns of as-synthesized CuO nanostructures. The XRD pattern is the replica of the JCPDS pattern with reference code 00-044-0706. No characteristic peaks of impure phases, such as Cu(OH)<sub>2</sub> or Cu<sub>2</sub>O were detected. This indicates the formation of single phase pure monoclinic CuO nanomaterial.

##### 3.1.2. FESEM

Figure 3 shows the morphology and size of the synthesized nanomaterial investigated by FESEM. FESEM images of as synthesized CuO reveal the growth of nanoparticles from the nucleating center whose maximum diameter is around 400 nm (Fig. 3). Morphology and size of the

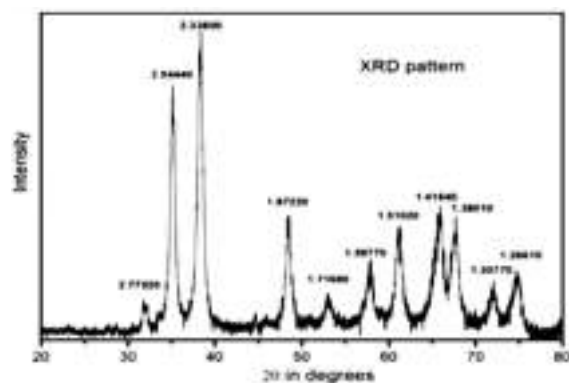


Fig. 2. Powder X-ray diffraction pattern of as synthesized CuO nanomaterial.

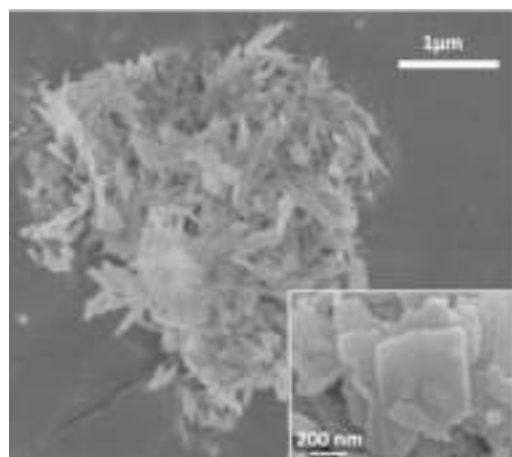


Fig. 3. FESEM image for CuO nanoflakes.

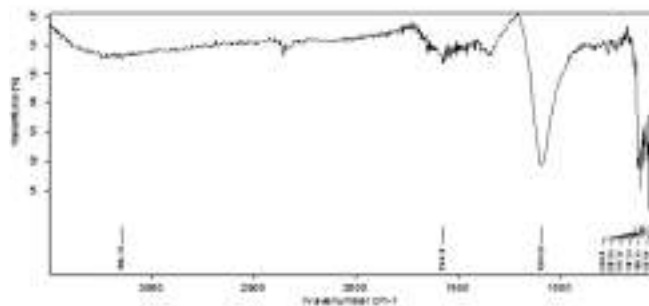


Fig. 4. FTIR spectrum of CuO nanoflakes.

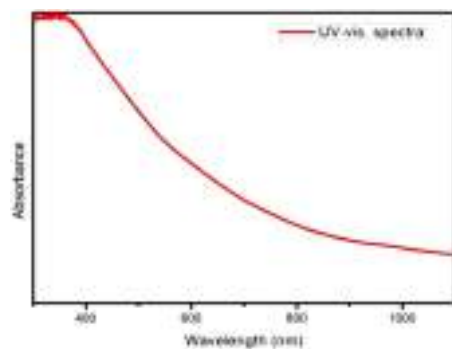


Fig. 5. UV-vis spectra of CuO nanoflakes.

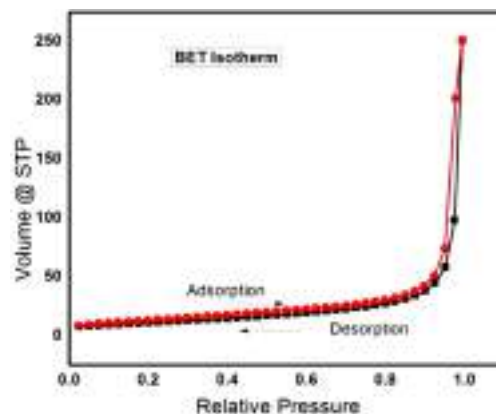


Fig. 6. BET isotherm of as synthesized CuO nanoflakes.

nanoparticles can be confirmed from the inset containing magnified image of the same.

### 3.1.3. FTIR

The synthesized nanostructure subjected to FTIR investigation (Fig. 4). The spectrum exhibited several strong bands below  $700\text{ cm}^{-1}$  i.e. at  $633, 607, 598, 587, 570, 557\text{ cm}^{-1}$  (Cu–O link stretch and O–Cu–O asymmetric vibrations) which confirmed the formation of monoclinic CuO phase. The characteristic band at  $607\text{ cm}^{-1}$  is due to Cu–O stretching.

### 3.1.4. UV-vis spectroscopy

Figure 5 depicts the UV-vis spectra of as synthesized CuO nanomaterial which shows the wide absorption in visible region which is in well agreement with the CuO nanostructures.

### 3.1.5. BET surface area

The effective Brunauer–Emmett–Teller (BET) surface area of the as-synthesized samples was measured using a Quantachrome ChemBET TPR/TPD analyzer. Figure 6 shows the isotherm of  $\text{N}_2$  adsorption of the nanoparticles. The effective BET specific surface area of as synthesized nanoparticles is found to be  $17.09\text{ m}^2/\text{g}$ .

## 3.2. Spectroscopic data of synthesized compounds

IR,  $^1\text{H}$  NMR,  $^{13}\text{C}$  NMR and mass spectral data of compounds 1a–1f are given below. The spectral data are in good correlation to the suggested structure of the compounds.

### 1. Diethyl 2,6-dimethyl-4-(4-nitrophenyl)-1,4-dihydropyridine-3,5-dicarboxylate (1a):

% Yield: 85; m.p.  $169\text{--}171\text{ }^\circ\text{C}$ .

IR,  $\nu_{\text{max}}/\text{cm}^{-1}$ :  $3342$  (NH),  $1703$  (CO),  $1643$  (CO),  $1523$  (=C–H and ring C=C),  $1485$  (C=C),  $1369$  (sym.  $\text{CH}_3$  in O– $\text{CH}_2$ – $\text{CH}_3$ ),  $1345$  (CN),  $1299\text{--}1258$  (C–O–C).  $^1\text{H}$  NMR ( $500.1\text{ MHz}$ ,  $\text{CDCl}_3$ ),  $\delta$ :  $1.23$  (3 H, Me),  $2.40$  (3 H,  $\text{CH}_3$ ),  $4.09$  (2 H,  $\text{CH}_2$ ),  $5.09$  (1 H, CH),  $5.80$  (1 H, NH),  $7.27\text{--}8.13$  (4 H, Ar–H).  $^{13}\text{C}$  NMR ( $125.8\text{ MHz}$ ,  $\text{CDCl}_3$ ),  $\delta$ :  $14.88$  ( $\text{CH}_3$ ),  $18.66$  ( $\text{CH}_3$ ),  $59.35$  ( $\text{CH}_2$ ),

167.56 (C=O), 102–154 (Ar–C). LCMS (m/z): calculated (M<sup>+</sup>+Na): 397, found 397.18.

**2. Diethyl 4-(furan-2-yl)-2,6-dimethyl-1,4-dihydropyridine-3,5-dicarboxylate (1b):**

% Yield, 90; m.p. 165–168 °C.

IR,  $\nu_{max}/\text{cm}^{-1}$ : 3334 (NH), 2978 (C–H), 1686 (C=O), 1639 (C=O), 1529 (=C–H and ring C=C), 1487 (C=C in furan), 1371 (CH<sub>3</sub> in O–CH<sub>2</sub>–CH<sub>3</sub>), 1325 (C–N in C<sub>Ar</sub>–N), 1296 (C–O–C). <sup>1</sup>H NMR (500.1 MHz, CDCl<sub>3</sub>),  $\delta$ : 1.26 (3 H, CH<sub>3</sub>), 2.33 (2 H, CH<sub>2</sub>), 4.14 (3 H, CH<sub>3</sub>), 5.20 (1 H, CH), 5.81 (1 H, NH), 5.94–7.27 (3 H, Ar–H).

**3. Diethyl 4-(4-methoxyphenyl)-2,6-dimethyl-1,4-dihydropyridine-3,5-dicarboxylate (1c):**

% Yield, 85; m.p. 160–162 °C.

IR  $\nu_{max}/\text{cm}^{-1}$ : 3324 (N–H), 2974 (C–H), 1696 (C=O), 1649 (C=O), 1529 (=C–H and ring C=C), 1487 (C=C), 1371 (CH<sub>3</sub> in O–CH<sub>2</sub>–CH<sub>3</sub>), 1326 (C–N in C<sub>Ar</sub>–N), 1295 (C–O–C). <sup>1</sup>H NMR (500.1 MHz, CDCl<sub>3</sub>),  $\delta$ : 0.88 (3 H, CH<sub>3</sub>), 1.23 (2 H, CH<sub>2</sub>), 2.33 (3 H, CH<sub>3</sub>), 3.90 (1 H, CH), 4.07 (1 H, NH), 6.74–7.26 (4 H, Ar–H).

**4. Diethyl 2,6-dimethyl-4-(2-phenylethylene)-1,4-dihydropyridine-3,5-dicarboxylate (1d):**

% Yield, 85; m.p. 223–225 °C.

IR  $\nu_{max}/\text{cm}^{-1}$ : 3334 (N–H), 2978 (C–H), 1686 (C=O), 1639 (C=O), 1487 (C=C), 1214 (C–O–C). LCMS (m/z): calculated (M<sup>+</sup>+Na): 378, found 378.31.

**5. Diethyl 2,6-dimethyl-4-(2-nitrophenyl)-1,4-dihydropyridine-3,5-dicarboxylate (1e):**

% Yield 75; m.p. 172–174 °C.

IR  $\nu_{max}/\text{cm}^{-1}$ : 3343 (N–H), 2888 (C–H), 1702 (C=O), 1642 (C=O), 1523 (=C–H and ring C=C), 1485–1433 (C=C), 1369 (CH<sub>3</sub> in O–CH<sub>2</sub>–CH<sub>3</sub>), 1346 (C–N in –N), 1298–1248 (C–O–C). <sup>1</sup>H NMR (500.1 MHz; CDCl<sub>3</sub>),  $\delta$ : 1.193 (3 H, CH<sub>3</sub>), 2.466 (3 H, CH<sub>3</sub>), 2.42 (2 H, CH<sub>2</sub>), 5.09 (1 H, CH), 5.84–7.27 (4 H, Ar–H), 6.46 (1 H, NH).

**6. Diethyl 4-(2-bromophenyl)-2,6-dimethyl-1,4-dihydropyridine-3,5-dicarboxylate (1f):**

% Yield 65; m.p. 210–213 °C.

<sup>1</sup>H NMR (500.1 MHz, CDCl<sub>3</sub>),  $\delta$ : 1.05 (3 H, CH<sub>3</sub>), 2.12 (3 H, CH<sub>3</sub>), 2.30 (2 H, CH<sub>2</sub>), 5.00 (1 H, CH), 6.77–7.58 (4 H, Ar–H), 5.82 (1 H, NH).

**7. Diethyl 4-(4-hydroxyphenyl)-2,6-dimethyl-1,4-dihydropyridine-3,5-dicarboxylate (1g):**

*R<sub>f</sub>*: 0.60; % Yield: 93; m.p. 241 °C.

IR spectrum ( $\nu_{max}/\text{cm}^{-1}$ ): 3344 (N–H), 2986 (C–H), 1792 (C=O), 1716 (C=O), 1540 (=C–H and ring C=C), 1218 (C–O–C).

Mass (m/z): calculated (M<sup>+</sup>+Na): 368, found 368.28.

UV (absorption): 400 nm.

**8. Diethyl 4-(4-bromophenyl)-2,6-dimethyl-1,4-dihydropyridine-3,5-dicarboxylate (1h):**

*R<sub>f</sub>*: 0.70; % Yield: 60; m.p. 211 °C.

<sup>1</sup>H NMR: (500.1 MHz; CDCl<sub>3</sub>; Me<sub>4</sub>Si): 1.41 (t, 3 H, CH<sub>3</sub>), 2.32 (s, 3 H, CH<sub>3</sub>), 2.41 (q, 2 H, CH<sub>2</sub>), 5.19 (s, 1 H, CH), 5.93–6.20 (m, 4 H, Ar–H), 4.41 (s, 1 H, NH).

**9. Diethyl 2',6'-dimethyl-1',4'-dihydro-2,4'-bipyridine-3',5'-dicarboxylate (1i):**

IR ( $\nu_{max}/\text{cm}^{-1}$ ): 3100 (N–H), 2927 (C–H), 1685 (C=O), 1632 (C=O), 1504 (=C–H and ring C=C), 1428 (C=C), 1377 (CH<sub>3</sub> in O–CH<sub>2</sub>–CH<sub>3</sub>), 1300 (C–N in C<sub>Ar</sub>–N); 1266 (C–O–C). <sup>1</sup>H NMR (500.1 MHz, CDCl<sub>3</sub>; Me<sub>4</sub>Si), 1.12 (3 H, CH<sub>3</sub>), 2.32 (2 H, CH<sub>2</sub>), 2.48 (3 H, CH<sub>3</sub>), 4.15 (1 H, CH), 4.721 (1 H, NH), 6.50–8.71 (4 H, Ar–H). MS (m/z): calculated (M<sup>+</sup>+K): 369, found 368.28.

**10. Diethyl 2,6-dimethyl-4-(3-nitrophenyl)-1,4-dihydropyridine-3,5-dicarboxylate(1j):**

IR ( $\nu_{max}/\text{cm}^{-1}$ ): 3343 (N–H), 2888 (C–H), 1702 (C=O), 1642 (C=O), 1523 (=C–H and ring C=C), 1485–1433 (C=C), 1369 (CH<sub>3</sub> in O–CH<sub>2</sub>–CH<sub>3</sub>), 1346 (C–N in –N), 1298–1248 (C–O–C). <sup>1</sup>H NMR (500.1 MHz, CDCl<sub>3</sub>, Me<sub>4</sub>Si), 1.193 (3 H, CH<sub>3</sub>), 2.466 (3 H, CH<sub>3</sub>), 2.42 (2 H, CH<sub>2</sub>), 5.09 (1 H, CH), 5.84–7.27 (4 H, Ar–H), 6.46 (1 H, NH).

**11. Diethyl 4-(furan-3-yl)-2,6-dimethyl-1,4-dihydropyridine-3,5-dicarboxylate (1k):**

IR ( $\nu_{max}/\text{cm}^{-1}$ ): 3344 (N–H), 2960 (C–H), 1697 (C=O), 1644 (C=O), 1539 (=C–H and ring C=C), 1475 (C=C), 1369 (CH<sub>3</sub> in O–CH<sub>2</sub>–CH<sub>3</sub>), 1320 (C–N in C<sub>Ar</sub>–N), 1296 (C–O–C). <sup>1</sup>H NMR (500.1 MHz, CDCl<sub>3</sub>, Me<sub>4</sub>Si): 1.23 (3 H, CH<sub>3</sub>), 2.32 (3 H, CH<sub>3</sub>), 2.18 (2 H, CH<sub>2</sub>), 5.19 (1 H, CH), 5.94–6.20 (3 H, Ar–H), 4.30 (1 H, NH).

**3.3. Spectral representation for representative compound — diethyl 2,6-dimethyl-4-(4-nitrophenyl)-1,4-dihydropyridine-3,5-dicarboxylate (1a)**

Diethyl 2,6-dimethyl-4-(4-nitrophenyl)-1,4-dihydropyridine-3,5-dicarboxylate (1a) was characterized by <sup>1</sup>H NMR (Fig. 7), LC-MS (Fig. 8), FTIR (Fig. 9), and <sup>13</sup>C DEPT NMR (Fig. 10) spectral analysis.

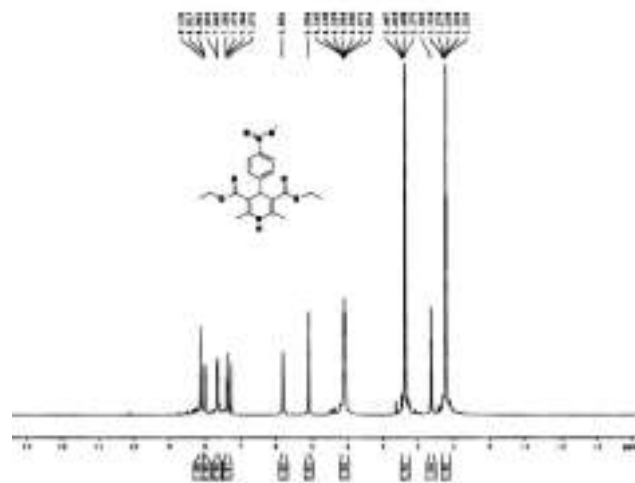


Fig. 7. <sup>1</sup>H NMR spectrum of 1a.

Diethyl 2,6-dimethyl-4-(4-nitrophenyl)-1,4-dihydropyridine-3,5-dicarboxylate (1a) was additionally characterized by <sup>13</sup>C distortionless enhancement by polarization transfer (DEPT).



Fig. 8. LC-MS spectrum of 1a.

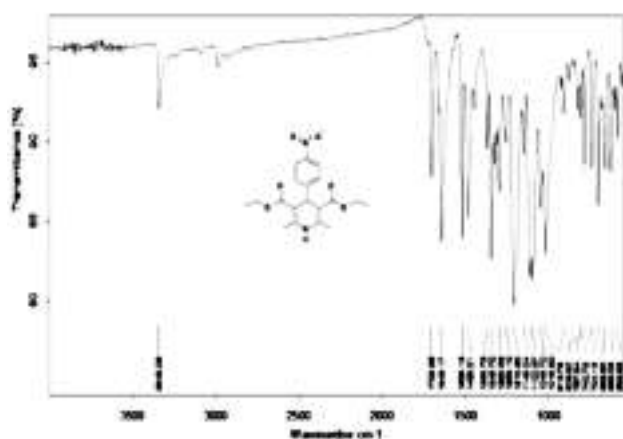


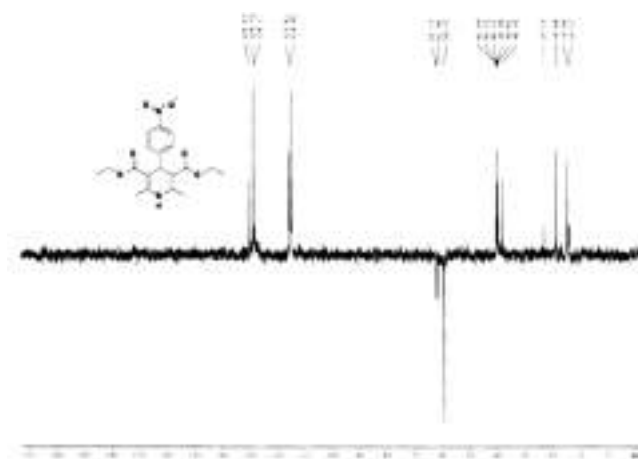
Fig. 9. FTIR spectrum of 1a.

The DEPT spectral analysis is a useful spectroscopic method for determination of different types of primary, secondary and tertiary carbon atoms. The DEPT spectroscopic method gives different signals for CH, CH<sub>2</sub> and CH<sub>3</sub> groups by variation of the selection angle parameter. The DEPT spectrum of 1a (Fig. 8) shows the signals for CH and CH<sub>3</sub> in an upward direction while the signal of CH<sub>2</sub> in the opposite direction. So the structure is confirmed by <sup>13</sup>C DEPT spectra.

The spectral data confirm the structure of synthesized compounds. The optimization study reveals that the CuO nanoparticle as an effective catalyst for synthesis of 1,4-dihydropyridine derivative, i.e. 2,6-dimethyl-4-(4-nitrophenyl)-1,4-dihydropyridine-3,5-dicarboxylate (1a). Moreover, the proposed protocol is microwave assisted, environmental benign, proficient, and fast method for synthesis of bio-inspired dihydropyridine derivative.

#### 4. Conclusion

A competent, simplistic and economical method for the synthesis of functionalized dihydropyridine derivatives was reported here, using CuO nanoflakes as a catalyst in an ethanol/water mixture green media. The products were obtained in remarkable yields and the reaction

Fig. 10. <sup>13</sup>C DEPT spectrum of 1a.

times were considerably low. The present protocol represents an easy and a remarkable method for the three-component reactions to synthesize some dihydropyridine derivatives using unique nanoscale materials. Moreover, the reusability of this CuO nanocatalyst is one of its important character and also this potency inspired us to use it for commercial and industrial organic synthesis applications.

#### References

- [1] M.B. Gawande, R. Luque, R. Zboril, *ChemCatChem* **6**, 3312 (2014).
- [2] M.B. Gawande, P.S. Brancoa, R.S. Varma, *Chem. Soc. Rev.* **42**, 3371 (2013).
- [3] D. Wang, D. Astruc, *Chem. Rev.* **114**, 6949 (2014).
- [4] Q.M. Kainz, R. Linhardt, R.N. Grass, *Adv. Funct. Mater.* **24**, 2020 (2014).
- [5] S.N. Shelke, S.R. Bankar, G.R. Mhaske, S.S. Kadam, D.K. Murade, *ACS Sustain. Catal. Eng.* **2**, 1699 (2014).
- [6] S. Sá, M.B. Gawande, A. Velhinho, J.P. Veiga, N. Bundaleski, *Green Chem.* **16**, 3494 (2014).
- [7] M.B. Gawande, I. Rathi, D. Nogueira, *Green Chem.* **15**, 1895 (2013).
- [8] M. Shokouhimehr, Y. Piao, J. Kim, Y. Jang, T. Hyeon, *Angew. Chem. Int. Ed.* **46**, 7039 (2007).
- [9] F. Shirini, M. Abedini, *J. Nanosci. Nanotechnol.* **13**, 4838 (2013).
- [10] H. Montazeri, A. Amani, H.R. Shahverdi, E. Haratifar, A.R. Shahverdi, *J. Nanostruct. Chem.* **3**, 25 (2013).
- [11] P. Arumugam, P.T. Perumal, *Ind. J. Chem. Sect. B Org. Incl. Med.* **47**, 1084 (2008).
- [12] A.W. Bauer, W.M.M. Kirby, J.C.T. Sherris, M. Turck, *Am. J. Clin. Pathol.* **45**, 493 (1966).
- [13] R.A. Janis, D.J. Triggler, *J. Med. Chem.* **26**, 775 (1983).
- [14] R.H. Boecker, F.P. Guengerich, *J. Med. Chem.* **29**, 1596 (1986).

- [15] M.F. Gordeev, D.V. Patel, E.M. Gordon, *J. Org. Chem.* **61**, 924 (1996).
- [16] C.E. Sunkel, M. Fau de Casa-Juana, L. Santos, A.G. Garcia, C.R. Artalejo, M. Villarroya, J. Cillero, *J. Med. Chem.* **35**, 2407 (1992).
- [17] D. Vo, W.C. Matowe, M. Ramesh, N. Iqbal, M.W. Wolowyk, S.E. Howlett, E.E. Knaus, *J. Med. Chem.* **38**, 2851 (1995).
- [18] S.A. Sadeek, W.A. Zordok, M.S. El-Attar, M.S. Ibrahim, *Bull. Chem. Soc. Ethiopia* **29**, 75 (2015).
- [19] Z. Luo, F. He, J. Luo, W. Zhang, *Am. J. Life Sci.* **3**, 1 (2015).
- [20] V. Klusa, *Drugs Fut.* **20**, 135 (1995).
- [21] T. Godfraind, R. Miller, M. Wibo, *Pharmacol. Rev.* **38**, 321 (1986).
- [22] A. Sausins, G. Duburs, *Heterocycles* **27**, 269 (1988).
- [23] A.C. Gaudio, A. Korolkovas, Y. Takahata, *J. Pharm. Sci.* **83**, 1110 (1994).
- [24] K. Cooper, M.J. Fray, M.J. Parry, K. Richardson, J. Steele, *J. Med. Chem.* **35**, 3115 (1992).
- [25] A. Agarwal, P.M.S. Chauhan, *Tetrahedron Lett.* **46**, 1345 (2005).
- [26] L. Ohberg, J. Westman, *Synlett* **8**, 1296 (2001).
- [27] J.G. Breitenbucher, G. Figliozzi, *Tetrahedron Lett.* **41**, 4311 (2000).
- [28] J.C. Liang, J.L. Yeh, C.S. Wang, S.F. Liou, C.H. Tasi, I. Chen, *J. Bioorg. Med. Chem. Lett.* **10**, 719 (2002).
- [29] R. Miri, H. Niknahad, G. Vesal, A. Shafiee, *Farmaco* **57**, 123 (2002).
- [30] A. Dondoni, A. Massi, E. Minghini, S. Sabbatini, V. Bertoasi, *J. Org. Chem.* **68**, 6172 (2002).
- [31] A. Dondoni, A. Massi, E. Minghini, V. Bertoasi, *Tetrahedron* **60**, 2311 (2004).
- [32] S.J. Ji, Z.Q. Jiang, J. Lu, T.P. Loh, *Synlett* **5**, 831 (2004).
- [33] M. Maheswara, V. Siddaiah, G.L. Damu, C. Venkata Rao, *Arkivoc* **2**, 201 (2006).
- [34] M.A. Chari, K. Syamasundar, *Catal. Commun.* **6**, 624 (2005).
- [35] S. Ko, M.N.V. Sastry, C. Lin, C.F. Yao, *Tetrahedron Lett.* **46**, 5771 (2005).
- [36] A. Kumar, R.A. Maurya, *Tetrahedron Lett.* **48**, 3887 (2007).
- [37] L.M. Wang, J. Sheng, L. Zhang, J.W. Han, Z. Fan, H. Tian, C.T. Qian, *Tetrahedron* **61**, 1539 (2005).
- [38] N. Tewari, N. Dwivedi, R.P. Tripathi, *Tetrahedron Lett.* **45**, 9011 (2004).
- [39] A. Kumar, R.A. Maurya, *Tetrahedron* **63**, 1946 (2007).
- [40] S.R. Cherkupally, R. Mekalan, *Chem. Pharm. Bull.* **56**, 1002 (2008).
- [41] H. Adibi, H.A. Samimi, M. Beygzadeh, *Catal. Commun.* **8**, 2119 (2007).
- [42] G. Sabitha, G.S.K. Reddy, C.S. Reddy, J.S. Yadav, *Tetrahedron Lett.* **44**, 4129 (2003).
- [43] S.B. Sapkal, K.F. Shelke, B.B. Shingate, M.S. Shingare, *Tetrahedron Lett.* **50**, 1754 (2009).
- [44] A. Maleki, *Tetrahedron* **68**, 7827 (2012).
- [45] A. Maleki, *Tetrahedron Lett.* **54**, 2055 (2013).
- [46] A. Maleki, N. Ghamari, M. Kamalzare, *RSC Adv.* **4**, 9416 (2014).
- [47] A. Maleki, M. Kamalzare, *Catal. Commun.* **53**, 67 (2014).
- [48] A. Maleki, R. Rahimi, S. Maleki, N. Hamidi, *RSC Adv.* **4**, 29765 (2014).



## Enhanced catalytic activity without the use of an external light source using microwave-synthesized CuO nanopetals

Govinda Lakhotiya<sup>\*1,2</sup>, Sonal Bajaj<sup>2</sup>, Arpan Kumar Nayak<sup>1</sup>, Debabrata Pradhan<sup>1</sup>, Pradip Tekade<sup>2</sup> and Abhimanyu Rana<sup>\*3</sup>

### Full Research Paper

[Open Access](#)**Address:**

<sup>1</sup>Material Science Center, Indian Institute of Technology Kharagpur, Kharagpur-721302, W.B., India, <sup>2</sup>Jankidevi Bajaj College of Science, Wardha-442001, M.S., India and <sup>3</sup>MESA+ Institute for Nanotechnology, University of Twente, 7500 AE, Enschede, Netherlands

**Email:**

Govinda Lakhotiya<sup>\*</sup> - lakhotiya.govinda@gmail.com;  
Abhimanyu Rana<sup>\*</sup> - rana.abhimanyu@gmail.com

<sup>\*</sup> Corresponding author

**Keywords:**

CuO nanopetals; dark catalytic activity; fast degradation of dyes; microwave synthesis

*Beilstein J. Nanotechnol.* **2017**, *8*, 1167–1173.

doi:10.3762/bjnano.8.118

Received: 06 February 2017

Accepted: 25 April 2017

Published: 30 May 2017

Associate Editor: R. Xu

© 2017 Lakhotiya et al.; licensee Beilstein-Institut.  
License and terms: see end of document.

### Abstract

We report enhanced catalytic activity of CuO nanopetals synthesized by microwave-assisted wet chemical synthesis. The catalytic reaction of CuO nanopetals and H<sub>2</sub>O<sub>2</sub> was studied with the application of external light source and also under dark conditions for the degradation of the hazardous dye methylene blue. The CuO nanopetals showed significant catalytic activity for the fast degradation of methylene blue and rhodamine B (RhB) under dark conditions, without the application of an external light source. This increased catalytic activity was attributed to the co-operative role of H<sub>2</sub>O<sub>2</sub> and the large specific surface area ( $\approx 40 \text{ m}^2 \cdot \text{g}^{-1}$ ) of the nanopetals. We propose a detail mechanism for this fast degradation. A separate study of the effect of different H<sub>2</sub>O<sub>2</sub> concentrations for the degradation of methylene blue under dark conditions is also illustrated.

### Introduction

Controlling air quality and water pollutants is a big challenge for environmental research [1]. Particularly, efforts have been taken to control these pollutants with the development of cost effective and ecologically friendly methods [2]. Metal oxides have attracted significant attention as a photocatalyst for the degradation of these pollutants [3-6]. Copper oxide (CuO) is one of the most efficient materials for the oxidation of the air pollutant carbon monoxide (CO) [7-9]. CuO is one of the few

p-type metal oxide semiconductors with a narrow band gap  $\approx 1.24 \text{ eV}$  [10]. The properties of CuO nanomaterials (nanoparticles, nanowires, nanosheets, etc.) are closely related to morphology and crystallite size [7]. These different nanoscale morphologies enhance the photoconductive and photochemical properties in various energy applications [7]. Being inexpensive, nontoxic, and readily available, CuO has attracted particular attention. However, in the degradation of water pollutants

(e.g., industrial dyes) as a photocatalytic oxidative species, CuO is found to be less effective as compared to other metal oxides [8-12]. Thus, in order to enhance its photocatalytic activity, CuO can be used with hydrogen peroxide ( $H_2O_2$ ) [12-21]. However, the degradation time of dyes is an important problem when using CuO as the photocatalyst.

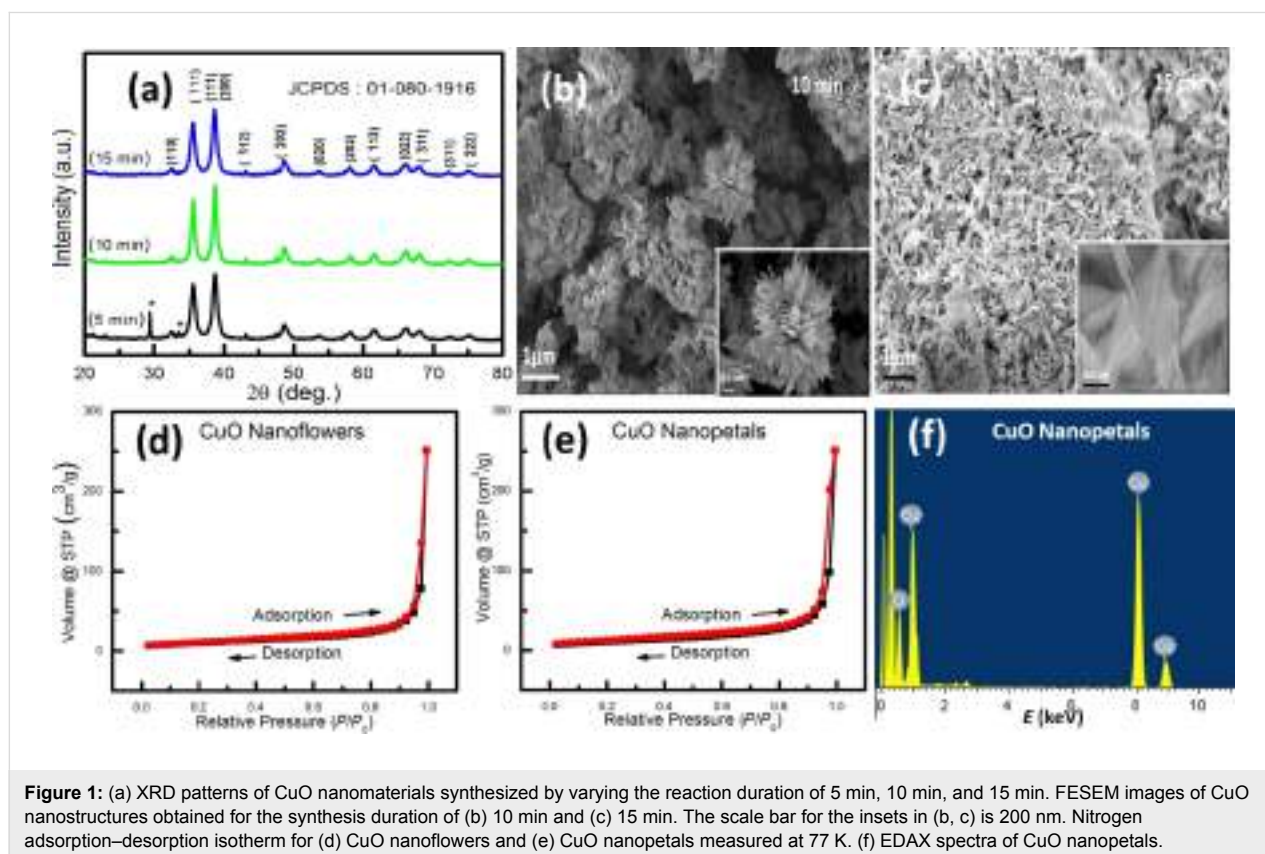
Here, we have adopted the simple microwave-assisted route for the wet chemical surfactantless synthesis of copper oxide (CuO) nanostructures (nanoflowers and nanopetals) having a large specific surface area. The catalytic reaction of CuO nanopetals and  $H_2O_2$  was studied under the application of an external light source and also under dark conditions for the degradation of hazardous dyes such as methylene blue and rhodamine B. We report enhanced catalytic activity of the synthesized CuO nanopetals, even without the use of an external light source (UV/visible light) for the degradation of these dyes. This is attributed to the role of  $H_2O_2$  and the large specific surface area of the nanopetals. The amount of the catalyst (CuO nanopetals) and the hazardous  $H_2O_2$  is minimized, and the reproducibility of the degradation of the dye with the same catalyst has been tested. The catalytic activity of CuO nanopetals activated by irradiation with photons (visible light) in the absence of  $H_2O_2$  is also studied and compared with the activity under dark conditions.

## Results and Discussion

### Structural and morphological study

Figure 1a illustrates X-ray diffraction (XRD) patterns of CuO nanostructures synthesized by varying the reaction duration of 5, 10, and 15 min. The sample obtained after 5 min of reaction time shows the diffraction peaks of both CuO and  $Cu_2O$  (marked by \*), indicating mixed-phase growth. It is interesting to observe that with the increase in the reaction duration, the diffraction peaks for  $Cu_2O$  disappear. For the samples obtained after 10 and 15 min of reaction time, the XRD pattern matches with JCPDS card no. 01-080-1916, which confirms the formation of phase-pure monoclinic CuO. The average crystallite size for the samples obtained after 10 and 15 min was calculated by using the Scherrer equation and is estimated to be  $\approx 11$  nm. As the sample obtained after 5 min exhibits phase impurity, only samples obtained with the reaction duration of 10 and 15 min were considered for further characterization.

Figure 1b,c shows field-emission scanning electron microscope (FESEM) images of CuO nanostructures synthesized with microwave irradiation for 10 min and 15 min. The CuO sample obtained with the reaction time of 10 min was found to resemble a flower-like morphology. Increasing the reaction duration to 15 min resulted in distinct and individual, uniform features having a petal-like morphology, which is clearly visible



in Figure 1c. The average width and length of these petal-like features are measured to be 250 and 400 nm, respectively. The insets of Figure 1b,c show the corresponding, magnified image, illustrating their size and morphology. The prolonged microwave agitation is believed to provide the necessary thermal energy for the morphological transformation. This can be inferred on the basis of the similarity in the morphological parameters of both the nanostructures. The growth of these surfactant-free nanostructures depends on certain parameters, including the concentration of NaOH, which promotes the preferential growth of CuO primary crystals along the  $\langle 010 \rangle$  and suppresses the growth in  $\langle 001 \rangle$  [22,23]. This preferential growth of the CuO nanostructure has also been observed in the sample obtained after a reaction time of 5 min, where some flake-like morphology is formed (Supporting Information File 1, Figure S1).

### Surface study

The Brunauer–Emmett–Teller (BET) technique was used to measure the surface area, pore radius, and pore volume of the CuO nanoflowers and nanopetals obtained by microwave synthesis at a duration of 10 and 15 min, respectively. Figure 1d,e shows nitrogen adsorption–desorption plots for the CuO nanoflowers and nanopetals. The effective specific surface area, pore radius and pore volume of nanoflowers (and nanopetals) were measured to be  $37.2 \text{ m}^2 \cdot \text{g}^{-1}$  ( $39.87 \text{ m}^2 \cdot \text{g}^{-1}$ ),  $17.48 \text{ \AA}$  ( $17.646 \text{ \AA}$ ), and  $0.38 \text{ mL} \cdot \text{g}^{-1}$  ( $0.38 \text{ mL} \cdot \text{g}^{-1}$ ), respectively. The marginal increase in the surface area of nanopetals as compared

to nanoflowers supports the hypothesis of disintegration of nanoflowers into nanopetals with increasing reaction duration. It should be noted that the specific surface area of the products in the present work is larger than that of previous reports on materials with similar morphology [24]. Figure 1f depicts the energy disperse X-ray photon spectroscopy (EDS) spectra of nanopetals of CuO, which confirms the stoichiometry and atomic percent of the synthesized material. The effective specific surface area of the sample obtained after a reaction duration of  $\approx 5$  min was found to be  $\approx 25.58 \text{ m}^2 \cdot \text{g}^{-1}$  (Supporting Information File 1, Figure S2), which is in good agreement with the preferential growth of nanocrystals along a certain direction with respect to time. As the effective surface area of as-synthesized nanopetals was larger than that of as-synthesized nanoflowers with the same morphology, further experiments were performed with as-synthesized nanopetals.

### Optical study

The UV–vis absorption spectra of as-synthesized CuO nanopetals is shown in the Figure 2a. It reflects a wide absorption spectrum up to 700 nm covering almost the entire visible spectrum. The absorption onset was estimated from the Tauc's plot as shown in Figure 2b. The band gap of CuO nanopetals was calculated by extrapolating the linear part of the plot of  $(\alpha h\nu)^{1/2}$  vs  $h\nu$  and is found to be  $\approx 1.85 \text{ eV}$  as shown in Figure 2b. This is different from the bulk bandgap of CuO, which is  $1.24 \text{ eV}$  [10]. This blue shift in the absorption further confirms the nanometer range of synthesized material.

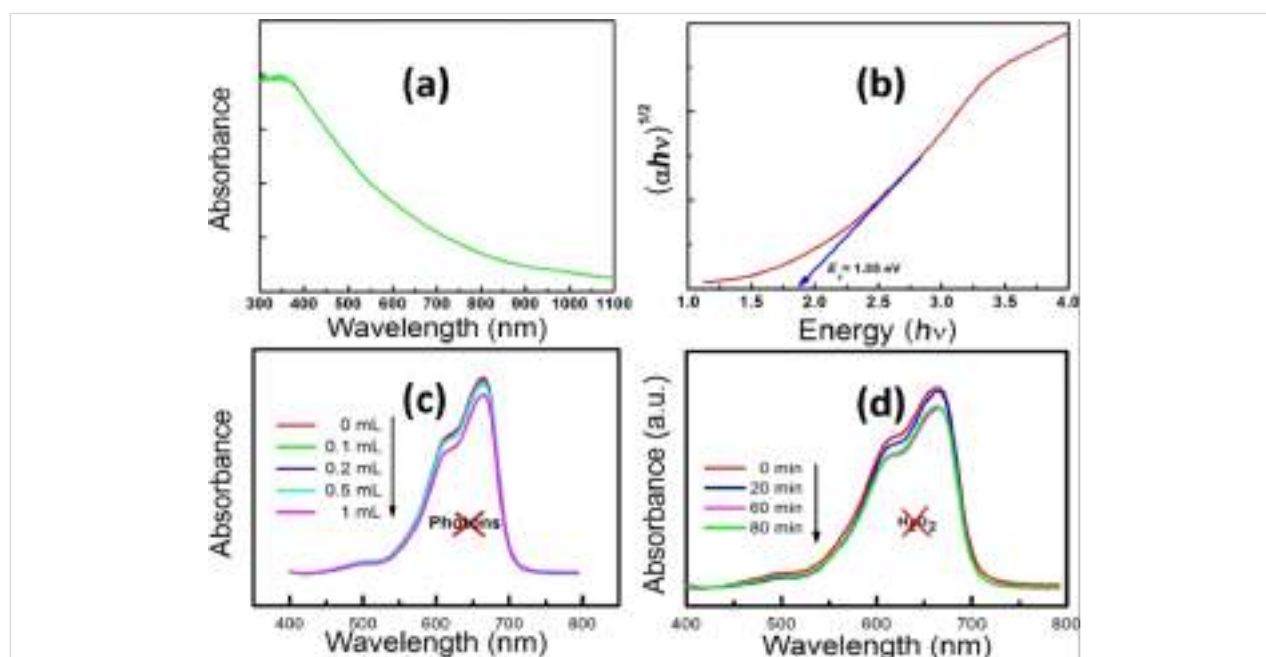


**Figure 2:** (a) UV–vis absorption spectra of CuO nanopetals. (b) Tauc's plot for CuO nanopetals (c) UV–vis absorption spectra illustrating the effect of different concentrations of  $\text{H}_2\text{O}_2$  in methylene blue degradation in the absence of CuO nanopetals (catalyst) under dark conditions. (d) UV–vis absorption spectrum of methylene blue degradation using CuO nanopetals as a photocatalyst for different durations.

## Catalytic activity of nanopetals for the degradation of methylene blue

The use of inorganic semiconductors as a heterogeneous, photocatalytic material has been extensively investigated under UV–vis light illumination, yet continues to attract even more attention due to the use of advanced materials in the process [3–5]. The catalytic photo-degradation of dyes takes place with the excitation of a catalyst using UV–vis light, leading to the generation of electrons and holes which are further responsible for the degradation through the formation of radicals [6,25]. The wide band gap, high surface area of CuO nanopetals was expected to be suitable for the photocatalytic activity for the degradation of the common cationic dye methylene blue (MB), and hence initially, a study has been carried out in which 40 mg of CuO nanopetal powder was dispersed in 40 mL of 50  $\mu$ M MB solution. This solution was allowed to stir for  $\approx$ 30 min under dark conditions and was then subjected to irradiation using an incandescent lamp (Philips, 200 W) at a working distance of 100 cm. Aliquots of about 4 mL were taken from the suspension at regular intervals and were centrifuged to filter suspended CuO powder. The MB concentration in the filtered suspension was studied with a Perkin Elmer Lambda 750 UV–vis spectrophotometer. Figure 2b shows the UV–vis absorption spectra of the aliquots taken out at different time intervals. In this study, the MB degradation rate is found to be very slow and only  $\approx$ 10% degradation has been observed in three hours. No further noticeable bleaching was observed within the next hour. This slow rate of degradation is in agreement with Miyauchi et al. [13], which may be due to the more negative valence band position of CuO than that of the redox potential required for producing free radicals for effective degradation. This slow rate of degradation was then overcome by introducing  $\text{H}_2\text{O}_2$  along with CuO, which resulted in the enhancement of the degradation of pollutants [12,26]. Recently, Zhang et al. successfully enhanced the catalytic activity by using peroxymonosulfate in their system instead of  $\text{H}_2\text{O}_2$  [6]. Few reports are available in which degradation of water pollutants were studied with CuO and  $\text{H}_2\text{O}_2$  without photon irradiation (UV/visible) [27,28]. Therefore, a separate study was carried out to investigate the effect of different concentrations of  $\text{H}_2\text{O}_2$  for MB degradation in the absence of CuO nanopetals (catalyst) without any irradiation (UV/visible light). Figure 2c shows the UV–vis absorption spectra for different concentrations of  $\text{H}_2\text{O}_2$  in MB solution, without catalyst, after one hour without photon irradiation. As can be seen from the Figure 2c, the concentration of  $\text{H}_2\text{O}_2$  with less than 1 mL had almost no effect on the degradation of the dye. However, the higher concentration of  $\text{H}_2\text{O}_2$  alone was found to be effective to some extent in the degradation of dye (6% in 1 h) even in the absence of catalyst. Furthermore, an experiment was performed by adding 1 mL of  $\text{H}_2\text{O}_2$  to a solution containing 40 mg CuO

nanopetals in 40 mL of 50  $\mu$ M MB solution. The solution went from a bluish color (MB solution) to colorless within two minutes. This fast activity without any irradiation unveils the interesting co-operative role of CuO and  $\text{H}_2\text{O}_2$  for the degradation of MB.

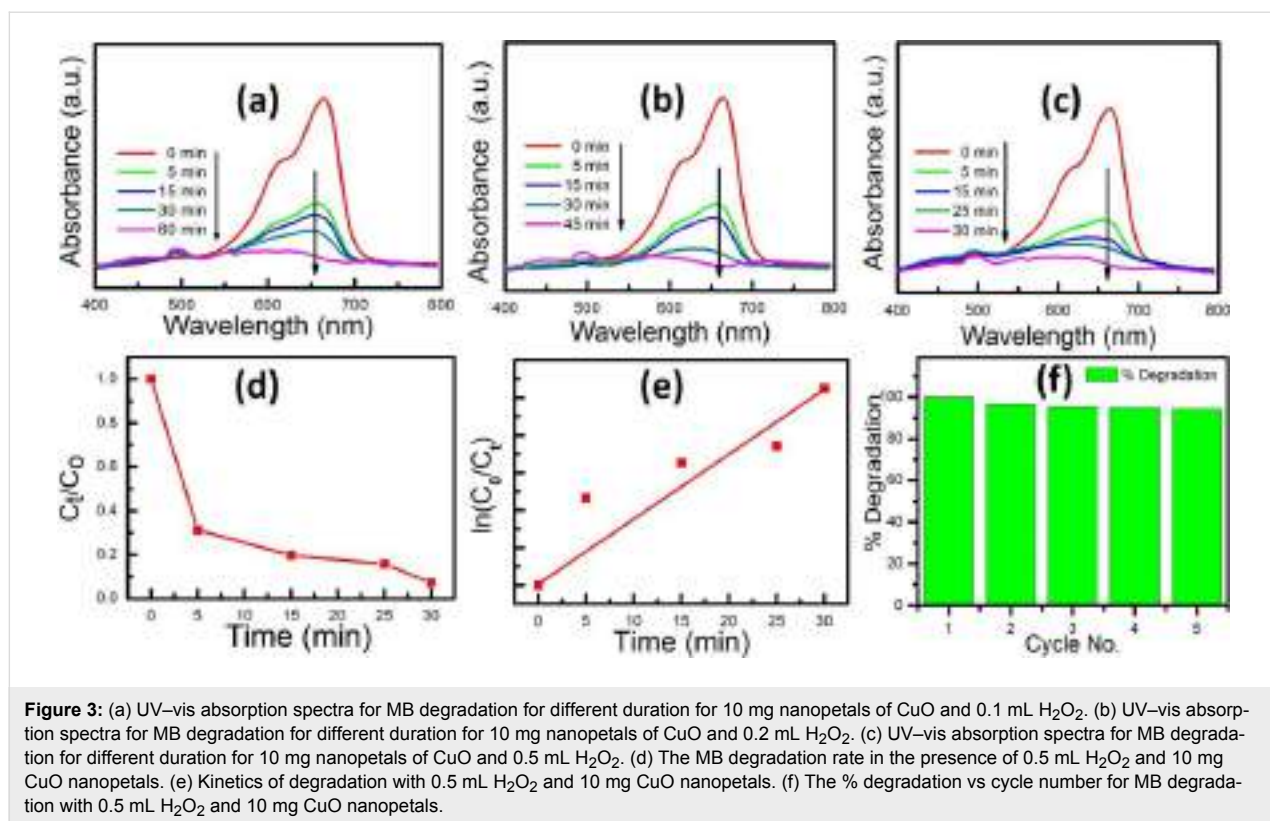
Further experiments were focused to achieve a higher rate of MB degradation with the optimum use of the cost effective catalyst and the hazardous  $\text{H}_2\text{O}_2$ . The amount of CuO nanopetals was minimized and fixed at 10 mg and concentrations of  $\text{H}_2\text{O}_2$  were varied (0.1 mL, 0.2 mL and 0.5 mL) to study the catalytic activity for the degradation of 40 mL of 50  $\mu$ M MB solution without irradiation. Figure 3a–c depicts the UV–vis absorption spectra of MB aliquot using 0.1 mL, 0.2 mL and 0.5 mL of  $\text{H}_2\text{O}_2$ , respectively, with 10 mg of catalyst. It can be clearly observed that the concentration of  $\text{H}_2\text{O}_2$  has an obvious effect on the degradation time, which decreases with increasing  $\text{H}_2\text{O}_2$  concentration.

As can be seen from Figure 3c, the complete degradation of the dye within 30 min was successfully achieved with 0.5 mL  $\text{H}_2\text{O}_2$  along with 10 mg CuO nanopetals. Figure 3d represents the kinetics of the MB degradation with 0.5 mL  $\text{H}_2\text{O}_2$  and 10 mg CuO nanopetals. The apparent rate constant of this degradation was calculated from the slope of  $\ln(C/C_0)$  vs time (Figure 3e) and found to be  $0.087 \text{ min}^{-1}$ . In order to examine the stability of the catalyst used for MB degradation, experiments with 0.5 mL  $\text{H}_2\text{O}_2$  and 10 mg nanopetals were repeated five times using the same CuO nanopetals without irradiation. Figure 3f shows the efficiency of the catalyst (five continuous cycles) in which degradation was efficiently achieved within 30 min. In the fifth cycle, the same catalyst could still successfully degrade  $\approx$ 94% of MB dye in 30 min. This highlights the efficacy and high stability of CuO nanopetals as a catalyst in this dye degradation activity. The phase and morphology of CuO nanopetals after the fifth cycle was also confirmed by XRD and FESEM (not shown).

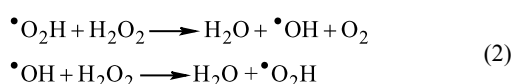
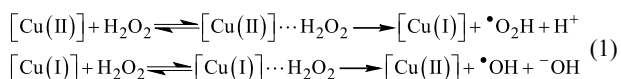
The catalytic activity of the sample obtained after 10 min (nanoflowers), whose surface area was closer to nanopetals, was also checked in the presence of  $\text{H}_2\text{O}_2$  under dark conditions. For this, 10 mg of CuO nanoflowers along with 0.5 mL of  $\text{H}_2\text{O}_2$  was used in a 40 mL, 50  $\mu$ M solution of MB. As expected, the nanoflowers could efficiently degrade  $\approx$ 93% of MB in 30 min (Supporting Information File 1, Figure S3).

## Reaction mechanism

It is well understood that the rate of degradation of organic dyes depends on the formation of free radicals [7,25,28]. The fast degradation of MB with the assistance of  $\text{H}_2\text{O}_2$  and as-synthesized CuO nanostructures (petals/flowers) without irradiation



with photons is believed to be the co-operative phenomenon and proceeds through the following two vital steps:



At first, H<sub>2</sub>O<sub>2</sub> reacts with the complex surface of nanopetals [Cu(II)] and reduces it to produce free radical  $\bullet\text{O}_2\text{H}$  and species [Cu(I)], which again, upon reaction with H<sub>2</sub>O<sub>2</sub>, become oxidized to give back [Cu(II)] along with radical  $\bullet\text{OH}$ , as represented in Equation 1. Thus, the free radicals  $\bullet\text{OH}$  and  $\bullet\text{O}_2\text{H}$  are generated in the reaction solution due to the oxidizing and reducing property of H<sub>2</sub>O<sub>2</sub>. These free radicals may be adsorbed on H<sub>2</sub>O<sub>2</sub> and can produce each other as depicted in Equation 2. Then, these free radicals  $\bullet\text{OH}$  and  $\bullet\text{O}_2\text{H}$ , which have a very high oxidizing capability, interact with the S atom in the middle heterogeneous ring of MB dye. This leads to the very easy degradation of the dye and produces SO<sub>4</sub><sup>2-</sup> ions (the main product of MB oxidation) [29]. The formation of SO<sub>4</sub><sup>2-</sup> ions in the mineralized degraded product was confirmed by adding BaCl<sub>2</sub> to it, which produces the white color precipitate of

BaSO<sub>4</sub>. Here, the larger surface area of CuO nanopetals provides higher adsorption of H<sub>2</sub>O<sub>2</sub> molecules for more radical formation to enhance the rate of degradation. Thus, the complete degradation reaction of MB under dark conditions was achieved in ample time and found to proceed through the co-operative activity between CuO nanostructures and H<sub>2</sub>O<sub>2</sub>.

### Catalytic activity of nanopetals for the degradation of rhodamine B

The catalytic performance of synthesized CuO nanopetals was also extended for the degradation of rhodamine B (RhB) using 40 mL of a 50 μM solution of RhB with the same experimental conditions, i.e., 10 mg catalyst and 0.5 mL H<sub>2</sub>O<sub>2</sub> and was found to be efficient (Supporting Information File 1, Figure S4). This confirms that the same as-synthesized CuO nanopetals can also be optimized for the efficient degradation of hazardous dyes other than MB.

### Conclusion

In summary, we have synthesized CuO nanoflowers and nanopetals in the absence of any surfactant and/or template using a microwave-assisted wet chemical technique. These nanostructures exhibited an increased band gap with larger surface area. The CuO nanopetals, with a specific surface area  $\approx 40 \text{ m}^2 \cdot \text{g}^{-1}$ , have proven to be an efficient catalyst for the degradation of water pollutant, industrial dyes, even in the absence

of photon irradiation (UV/visible). A corresponding mechanism for the fast degradation observed was also proposed.

## Experimental

### Materials and instrumentation

Commercial, high-grade copper sulphate ( $\text{CuSO}_4 \cdot 5\text{H}_2\text{O}$ , 99.95%), sodium hydroxide (NaOH), ethanol ( $\text{C}_2\text{H}_5\text{OH}$ ), acetone ( $\text{C}_3\text{H}_6\text{O}$ ), methylene blue (MB), hydrogen peroxide ( $\text{H}_2\text{O}_2$ , 30%), and rhodamine B (RhB) were obtained from Sigma–Aldrich, Merck and SD Fine. CuO nanostructures were characterized by X-ray diffraction by a PANalytical high-resolution X-ray diffractometer (PW 3040/60) operated at 40 kV and 30 mA using  $\text{Cu K}\alpha$  X-rays ( $1.54 \text{ \AA}$ ), energy dispersive X-ray spectroscopy using Oxford detectors, field-emission scanning electron microscopy using a Carl Zeiss SUPRA 40 instrument, and the surface area was characterized using a Quantachrome ChemBET TPR/TPD analyzer. The optical properties were analyzed using a UV–vis absorption spectrophotometer by Shimadzu 1800.

### Material synthesis

In the present study, the microwave-assisted synthesis of CuO nanoflowers and nanopetals was carried out using a microwave-irradiated wet chemical technique. At first, equimolar solutions (0.5 M) of copper sulphate and sodium hydroxide were prepared separately in 25 mL of ethanol and were allowed to stir at room temperature for about 15 min. Thereafter, sodium hydroxide solution was added drop wise to copper sulphate solution. The resulting mixture was transferred to the microwave chamber with the reaction conditions of 700 W for 10 min or 15 min. During the reaction, the color of the solution changed initially from blue to colorless and then slowly turned black. The black colloidal solution was centrifuged to separate out the precipitates. These precipitates were then washed using double distilled water, absolute ethanol, and acetone in sequence. This procedure was repeated several times. Finally, the black powder was dried at  $60 \text{ }^\circ\text{C}$  for 4 h and used for further characterization. The synthesis parameters such as reaction time, molar concentration of the precursors, and power of microwave irradiation were monitored so as to obtain phase-pure CuO nanoflowers and nanopetals. All the reactions were carried out using Raga's commercial scientific microwave oven attached with a reflux system.

### Catalytic activity study

The photocatalytic and the catalytic activity under dark conditions of the as-synthesized CuO nanopetals were studied for the degradation of a common cationic dye, methylene blue (MB), in the absence and presence of  $\text{H}_2\text{O}_2$ , respectively. For the photocatalytic activity study, 40 mg of CuO nanopetal powder was dispersed in 40 mL of a 50  $\mu\text{M}$  MB solution and allowed to stir

for  $\approx 30$  min under dark conditions and was then subjected to irradiation using an incandescent lamp (Philips, 200 W) at a working distance of 100 cm. The dark catalytic study was performed with 10 mg of CuO nanopetals and varying concentrations of  $\text{H}_2\text{O}_2$ . During both the studies, i.e., under dark conditions and the photocatalytic study, aliquots of about 4 mL were taken out from the suspension at regular intervals and were centrifuged to filter suspended CuO powder. The MB concentration in the filtered suspension was studied with a Perkin Elmer Lambda 750 UV–vis spectrophotometer. The dark catalytic activity of the as-synthesized CuO nanopetals was also checked for the degradation of RhB under the same experimental conditions.

## Supporting Information

### Supporting Information File 1

Additional figures.

[<http://www.beilstein-journals.org/bjnano/content/supplementary/2190-4286-8-118-S1.pdf>]

## Acknowledgements

GL thanks Head, Material Science Center, Indian Institute of Technology, Kharagpur, India and Principal, Jankidevi Bajaj College of Science, Wardha (M.S.), India for providing facilities for carrying out a part of this work. DP acknowledges funding from SERB, DST through the grant SB/S1/IC-15/2013. All the authors agreed on the results and have given approval of the manuscript.

## References

- Gogate, P. R.; Pandit, A. B. *Adv. Environ. Res. (Oxford, U. K.)* **2004**, *8*, 501–551. doi:10.1016/s1093-0191(03)00032-7
- Rauf, M. A.; Ashraf, S. S. *Chem. Eng. J.* **2009**, *151*, 10–18. doi:10.1016/j.cej.2009.02.026
- Zhao, Q.; Ju, D.; Deng, X.; Huang, J.; Cao, B.; Xu, X. *Sci. Rep.* **2015**, *5*, 7874. doi:10.1038/srep07874
- Shao, M.; Xu, X.; Huang, J.; Zhang, Q.; Ma, L. *Sci. Adv. Mater.* **2013**, *5*, 962–981. doi:10.1166/sam.2013.1545
- Zhao, Q.; Ju, D.; Song, X.; Deng, X.; Ding, M.; Xu, X.; Zeng, H. *Sens. Actuators, B* **2016**, *229*, 627–634. doi:10.1016/j.snb.2016.01.129
- Zhang, S.; Fan, Q.; Gao, H.; Huang, Y.; Liu, X.; Li, J.; Xu, X.; Wang, X. *J. Mater. Chem. A* **2016**, *4*, 1414–1422. doi:10.1039/c5ta08400h
- Zhang, Q.; Zhang, K.; Xu, D.; Yang, G.; Huang, H.; Nie, F.; Liu, C.; Yang, S. *Prog. Mater. Sci.* **2014**, *60*, 208–33737. doi:10.1016/j.pmatsci.2013.09.003
- Lam, S.-M.; Sin, J.-C.; Abdullah, A. Z.; Mohamed, A. R. *Desalin. Water Treat.* **2012**, *41*, 131–169. doi:10.1080/19443994.2012.664698
- Xu, H.; Zhu, G.; Zheng, D.; Xi, C.; Xu, X.; Shen, X. *J. Colloid Interface Sci.* **2012**, *383*, 75–81. doi:10.1016/j.jcis.2012.06.017

10. Chong, M. N.; Jin, B.; Chow, C. W. K.; Saint, C. *Water Res.* **2010**, *44*, 2997–3027. doi:10.1016/j.watres.2010.02.039
11. Liu, J.; Jin, J.; Deng, Z.; Huang, S.-Z.; Hu, Z.-Y.; Wang, L.; Wang, C.; Chen, L.-H.; Li, Y.; Van Tendeloo, G.; Su, B.-L. *J. Colloid Interface Sci.* **2012**, *384*, 1–9. doi:10.1016/j.jcis.2012.06.044
12. Yang, C.; Su, X.; Xiao, F.; Jian, J.; Wang, J. *Sens. Actuators, B* **2011**, *158*, 299–303. doi:10.1016/j.snb.2011.06.024
13. Miyauchi, M.; Nakajima, A.; Watanabe, T.; Hashimoto, K. *Chem. Mater.* **2002**, *14*, 2812–2816. doi:10.1021/cm020076p
14. Yu, H.; Yu, J.; Liu, S.; Mann, S. *Chem. Mater.* **2007**, *19*, 4327–4334. doi:10.1021/cm070386d
15. Deng, X.; Zhang, Q.; Zhao, Q.; Ma, L.; Ding, M.; Xu, X. *Nanoscale Res. Lett.* **2015**, *10*, 8. doi:10.1186/s11671-014-0726-x
16. Deng, X.; Zhang, Q.; Zhou, E.; Ji, C.; Huang, J.; Shao, M.; Ding, M.; Xu, X. *J. Alloys Compd.* **2015**, *649*, 1124–1129. doi:10.1016/j.jallcom.2015.07.124
17. Liu, L.; Yang, W.; Li, Q.; Gao, S.; Shang, J. K. *ACS Appl. Mater. Interfaces* **2014**, *6*, 5629–5639. doi:10.1021/am500131b
18. Deng, X.; Wang, C.; Zhou, E.; Huang, J.; Shao, M.; Wei, X.; Liu, X.; Ding, M.; Xu, X. *Nanoscale Res. Lett.* **2016**, *11*, 29. doi:10.1186/s11671-016-1246-7
19. Wu, F.; Banerjee, S.; Li, H.; Myung, Y.; Banerjee, P. *Langmuir* **2016**, *32*, 4485–4493. doi:10.1021/acs.langmuir.6b00915
20. Basnet, P.; Zhao, Y. *Catal. Sci. Technol.* **2016**, *6*, 2228–2238. doi:10.1039/C5CY01464F
21. Deng, X.; Wang, C.; Shao, M.; Xu, X.; Huang, J. *RSC Adv.* **2017**, *7*, 4329–4338. doi:10.1039/c6ra27634b
22. Jung, A.; Cho, S.; Cho, W. J.; Lee, K.-H. *Korean J. Chem. Eng.* **2012**, *29*, 243–248. doi:10.1007/s11814-011-0168-4
23. Xu, L.; Xu, H.-Y.; Wang, F.; Zhang, F.-J.; Meng, Z.-D.; Zhao, W.; Oh, W.-C. *J. Korean Ceram. Soc.* **2012**, *49*, 151–154. doi:10.4191/kcers.2012.49.2.151
24. Xu, X.; Yang, H.; Liu, Y. *CrystEngComm* **2012**, *14*, 5289–5298. doi:10.1039/c2ce25420d
25. Kumar, S. G.; Rao, K. S. R. K. *Appl. Surf. Sci.* **2017**, *391*, 124–148. doi:10.1016/j.apsusc.2016.07.081
26. Srivastava, R.; Prathap, M. U. A.; Ore, R. *Colloids Surf., A* **2011**, *392*, 271–282. doi:10.1016/j.colsurfa.2011.10.004
27. Zaman, S.; Zainelabdin, A.; Amin, G.; Nur, O.; Willander, M. *J. Phys. Chem. Solids* **2012**, *73*, 1320–1325. doi:10.1016/j.jpcs.2012.07.005
28. Gaya, U. I.; Abdullah, A. H. *J. Photochem. Photobiol., C: Photochem. Rev.* **2008**, *9*, 1–12. doi:10.1016/j.jphotochemrev.2007.12.003
29. Houas, A.; Lachheb, H.; Ksibi, M.; Elaloui, E.; Guillard, C.; Herrmann, J.-M. *Appl. Catal., B* **2001**, *31*, 145–157. doi:10.1016/s0926-3373(00)00276-9

## License and Terms

This is an Open Access article under the terms of the Creative Commons Attribution License (<http://creativecommons.org/licenses/by/4.0>), which permits unrestricted use, distribution, and reproduction in any medium, provided the original work is properly cited.

The license is subject to the *Beilstein Journal of Nanotechnology* terms and conditions: (<http://www.beilstein-journals.org/bjnano>)

The definitive version of this article is the electronic one which can be found at:  
doi:10.3762/bjnano.8.118

# Synthesis of Diethyl 4-(Phenyl-substituted)-2,6-dimethyl-1,4-dihydropyridine-3,5-dicarboxylates Catalyzed by CoCl<sub>2</sub>/K-10 Montmorillonite in Water and Their Antimicrobial Activity<sup>1</sup>

S. D. Bajaj, O. A. Mahodaya, P. V. Tekade\*, V. B. Patil, and Suraj D. Kukade

Department of Chemistry, Jankidevi Bajaj College of Science,  
Jammalal Bajaj Marg, Civil Lines, Wardha, 442001 India  
\*e-mail: jbsciencewardha@yahoo.co.in; pradiptekade@gmail.com

Received July 26, 2016

**Abstract**—A simple and efficient method of one pot synthesis of 1,4-dihydropyridine by three components reaction of aromatic aldehydes with 1,3-dicarbonyl compound, ammonium acetate and catalytic amount of CoCl<sub>2</sub> based on the Hantzsch reaction is developed. The process is catalyzed by an inexpensive catalyst in water medium, gives high yield of products and involves no volatile organic solvents. Some synthesized compounds demonstrated antimicrobial activity.

**Keywords:** antimicrobial activity, CoCl<sub>2</sub> catalyst, 1,4-dihydropyridine, Hantzsch reaction, K-10 montmorillonite

**DOI:** 10.1134/S1070363217030264

## INTRODUCTION

Dihydropyridyl compounds attract close attention due to various applications in medicine and specific properties determined by several reactive centers combined in their molecules [1, 2]. Dihydropyridine derivatives, including nifedipine, nitrendipine and nimodipine [3, 4], are calcium channel blockers. A number of dihydropyridines are potential drugs for treatment of congestive heart failure [5, 6] and demonstrate properties of neuroprotective [7], anti-hypertensive, antibacterial, and anticancer agents [8, 9].

## RESULTS AND DISCUSSION

We report herein water-mediated method of synthesis of Hantzsch dihydropyridines bearing various substituents (Table 1) using CoCl<sub>2</sub>/K-10 Montmorillonite as the catalyst (Scheme 1). A number of aryl and heteroaryl aldehydes smoothly underwent rapid multicomponent condensation to accomplish several substituted functionally important Hantzsch dihydropyridines in high yield and purity.

Different solvents, including dimethylformamide, chloroform, tetrahydrofuran, acetonitrile, ethanol, and

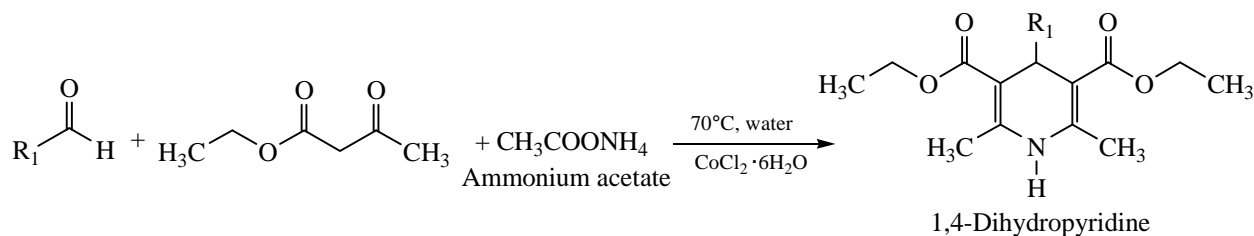
water were tested in the process. Water was determined to be the most efficient media for the reaction.

Aryl aldehydes with electron-donating and electron-withdrawing substituents at various positions produced the corresponding products without affecting the substituents and the substitution pattern.  $\alpha,\beta$ -Unsaturated aryl aldehydes (cinnamaldehyde) underwent rapid conversion without polymerization and other side reactions.

**Table 1.** Physical characteristics of the synthesized compounds

Comp. no.	R	Formula	M, mg	Time, min
<b>1a</b>	C <sub>6</sub> H <sub>5</sub> O	C <sub>17</sub> H <sub>21</sub> NO <sub>5</sub>	319.35	65
<b>1b</b>	C <sub>6</sub> H <sub>4</sub> OH	C <sub>19</sub> H <sub>23</sub> NO <sub>5</sub>	345.38	95
<b>1c</b>	C <sub>6</sub> H <sub>4</sub> NO <sub>2</sub>	C <sub>19</sub> H <sub>22</sub> N <sub>2</sub> O <sub>6</sub>	374.38	60
<b>1d</b>	C <sub>7</sub> H <sub>7</sub> O	C <sub>20</sub> H <sub>25</sub> NO <sub>5</sub>	359.41	85
<b>1e</b>	C <sub>8</sub> H <sub>7</sub>	C <sub>21</sub> H <sub>26</sub> NO <sub>4</sub>	343.41	105
<b>1f</b>	C <sub>5</sub> H <sub>4</sub> N	C <sub>18</sub> H <sub>22</sub> N <sub>2</sub> O <sub>4</sub>	330.37	70
<b>1g</b>	C <sub>6</sub> H <sub>4</sub> NO <sub>2</sub>	C <sub>19</sub> H <sub>22</sub> N <sub>2</sub> O <sub>6</sub>	374.39	75
<b>1h</b>	C <sub>4</sub> H <sub>3</sub> O	C <sub>17</sub> H <sub>21</sub> NO <sub>5</sub>	319.35	70
<b>1i</b>	C <sub>6</sub> H <sub>4</sub> Br	C <sub>19</sub> H <sub>22</sub> BrNO <sub>4</sub>	408.29	65
<b>1j</b>	C <sub>6</sub> H <sub>4</sub> Br	C <sub>19</sub> H <sub>22</sub> BrNO <sub>4</sub>	408.29	60

<sup>1</sup> The text was submitted by the authors in English.

**Scheme 1.** Synthesis of 1,4-dihydropyridine derivatives.

$\text{CoCl}_2$  in combination with K-10 Montmorillonite clay acted as efficient catalysts in the synthesis of title compounds from acid sensitive aldehydes (Table 2).

Application of  $\text{CoCl}_2$  as a catalyst reduced time required for the reaction to complete and led to high yields of the process. Influence of concentration of  $\text{CoCl}_2$  catalyst was studied (Table 3). Concentration of 2 mol % was determined to be the optimum one.

**Antibacterial screening.** The compounds **1a–1j** were tested for their *in vitro* antibacterial activity against *Pseudomonas aeruginosa* (MTCC-2435), *Streptococcus epidermidis* and *Staphylococcus aureus* (MTCC-96) by the disc diffusion method using Muller–Hinton agar (Hi-Media) medium and ciprofloxacin tablet (250 mg) as the standard. The compounds **1a–1j** were tested at concentrations of 50, 100, 200, and 300  $\mu\text{g}/\text{mL}$  in DMSO. The minimum inhibitory concentration of all compounds was determined to be 100  $\mu\text{g}/\text{mL}$ . The zones of inhibition (mm) were measured after 24 h incubation at 37°C (Table 4).

Effectivity classified into four zones on the basis of the diameter of the zone of inhibition: 0–5 mm (poor activity); 6–10 mm (moderate activity); 11–15 mm (high activity); and above 16 mm (very high activity);

Each value is an average of three independent determinations.

**Table 2.** Optimization of catalysts with respect to yield, time, and temperature

Catalyst	Yield, %	Time, min	$T$ , °C
KF/Alumina	71	120	78
Silica gel	75	500	–
Alumina sulphuric acid	80	200	70
$\text{AlCl}_3 \cdot 6\text{H}_2\text{O}$	70	180	60
$\text{CoCl}_2$	95	65	70

## EXPERIMENTAL

Melting points were determined on a digital melting point apparatus (EQ-730).  $^1\text{H}$  and  $^{13}\text{C}$  NMR spectra were measured on a BRUKER Avance II 500.1 spectrometer in  $\text{CDCl}_3$  using TMS as the internal standard. IR spectra were recorded on a Bruker Alpha FT-IR spectrophotometer. MS were measured on an Accu TOF Mass spectrometer. Elemental analysis was carried out on an Elemental analyser EURO EA 3000.

**Synthesis of diethyl 4-(phenyl-substituted)-2,6-dimethyl-1,4-dihydropyridine-3,5-dicarboxylates (1a–1j).** A mixture of an aromatic aldehyde (1 mmol), ethyl acetoacetate (2 mmol), ammonium acetate (1.3 mmol), and cobalt chloride hexahydrate (2 mol %) was vigorously stirred in water (2 mL) at 70°C for the stipulated period of time. Upon completion of the reaction (TLC), 1–2 mL of ethanol were added to facilitate granulation of a product and poured into crushed ice. A solid product was filtered off, washed several times with water and crystallized from aqueous ethanol. Sometimes the products were isolated as viscous oils. In such cases those were refluxed with 0.2 g of K-10 Montmorillonite clay as a solid state catalyst to facilitate formation of a solid product.

**Diethyl 4-(furan-2-yl)-2,6-dimethyl-1,4-dihydropyridine-3,5-dicarboxylate (1a).** Yield 90%, mp 166°C.  $R_f$  0.57. IR spectrum,  $\nu$ ,  $\text{cm}^{-1}$ : 3334 (NH), 2978 (C–H), 1686 (C=O), 1639 (C=O), 1529 (=C–H and C=C),

**Table 3.** Optimization of the catalyst concentration

Concentration of $\text{CoCl}_2$ , mol %	Yield, %
6.0	95
4.0	95
2.0	95
1.0	75
0.5	70

**Table 4.** Zones of inhibition for compounds **1a–1j** against bacterial strains

Compound	Zone of inhibition, mm (100 µg/mL)		
	<i>Pseudomonas aeruginosa</i>	<i>Streptococcus epidermidis</i>	<i>Staphylococcus aureus</i>
<b>1a</b>	16	18	17
<b>1b</b>	0	14	18
<b>1c</b>	8	10	14
<b>1d</b>	10	12	12
<b>1e</b>	14	0	8
<b>1f</b>	12	7	0
<b>1g</b>	14	8	10
<b>1h</b>	0	10	9
<b>1i</b>	9	13	15
<b>1j</b>	14	8	0
Ciprofloxacin	18	20	20

1487 (C=C in furan), 1371 (CH<sub>3</sub> in O–CH<sub>2</sub>–CH<sub>3</sub>), 1325 (C–N in C<sub>Ar</sub>–N), 1296 (C–O–C). <sup>1</sup>H NMR spectrum, δ, ppm: 1.26 s (3H, CH<sub>3</sub>), 2.33 q (2H, CH<sub>2</sub>), 4.14 t (3H, CH<sub>3</sub>), 5.20 s (1H, CH), 5.81 s (1H, NH), 5.94–7.27 m (3H, Ar-H). LC-MS (*m/z*): Found: *m/z* 343.27 [*M* + Na]<sup>+</sup>. Calculated: [*M* + Na]<sup>+</sup> 343.35.

**Diethyl 4-(4-hydroxyphenyl)-2,6-dimethyl-1,4-dihydropyridine-3,5-dicarboxylate (1b).** Yield 93%, mp 241°C. *R*<sub>f</sub> 0.60. IR spectrum, ν, cm<sup>-1</sup>: 3344 (N–H), 2986 (C–H), 1792 (C=O), 1716 (C=O), 1540 (=C–H and ring C=C), 1218 (C–O–C). LC-MS (*m/z*): Found: *m/z* 368.28 [*M* + Na]<sup>+</sup>. Calculated: [*M* + Na]<sup>+</sup> 368.

**Diethyl 2,6-dimethyl-4-(4-nitrophenyl)-1,4-dihydropyridine-3,5-dicarboxylate (1c).** Yield 85%, mp 170°C. *R*<sub>f</sub> 0.54. IR spectrum, ν, cm<sup>-1</sup>: 3342 (NH), 1703 (C=O), 1643 (C=O), 1523 (=C–H and ring C=C), 1485 (C=C), 1369 (sym. CH<sub>3</sub> in O–CH<sub>2</sub>–CH<sub>3</sub>), 1345 (C–N in C<sub>Ar</sub>–N). <sup>1</sup>H NMR spectrum, δ, ppm: 1.23 t (3H, CH<sub>3</sub>), 2.40 s (3H, CH<sub>3</sub>), 4.09 q (2H, CH<sub>2</sub>), 5.09 s (1H, CH), 5.80 s (1H, NH). <sup>13</sup>C NMR spectrum, δ, ppm: 14.88 (CH<sub>3</sub>), 18.66 (CH<sub>3</sub>), 59.35 (CH<sub>2</sub>), 167.56 (C=O). <sup>13</sup>C NMR-DEPT spectrum, δ, ppm: 14.07 (CH<sub>3</sub>), 18.66 (CH<sub>3</sub>), 40.15 (CH), 61.90 (CH<sub>2</sub>), 115.61 (CH, Ar), 128.74 (CH, Ar). LC-MS (*m/z*): Found: *m/z* 397.18 [*M* + Na]<sup>+</sup>. Calculated: [*M* + Na]<sup>+</sup> 397.

**Diethyl 4-(4-methoxyphenyl)-2,6-dimethyl-1,4-dihydropyridine-3,5-dicarboxylate (1d).** Yield 85%, mp 161°C. *R*<sub>f</sub> 0.65. IR spectrum, ν, cm<sup>-1</sup>: 3324 (N–H), 2974 (C–H), 1696 (C=O), 1649 (C=O), 1529 (=C–H

and ring C=C), 1487 (C=C), 1371 (CH<sub>3</sub> in O–CH<sub>2</sub>–CH<sub>3</sub>), 1326 (C–N in C<sub>Ar</sub>–N), 1295 (C–O–C). <sup>1</sup>H NMR spectrum, δ, ppm: 0.88 s (3H, CH<sub>3</sub>); 1.23 q (2H, CH<sub>2</sub>), 2.33 t (3H, CH<sub>3</sub>), 3.90 s (1H, CH), 4.07 s (1H, NH). LC-MS (*m/z*): Found: *m/z* 358.30 [*M* + H]<sup>+</sup>. Calculated: [*M* + H]<sup>+</sup> 357.

**Diethyl-2,6-dimethyl-4-(2-phenylethylene)-1,4-dihydropyridine-3,5-dicarboxylate (1e).** Yield 85%, mp 224°C. *R*<sub>f</sub> 0.70. IR spectrum, ν, cm<sup>-1</sup>: 3334 (N–H), 2978 (C–H), 1686 (C=O), 1639 (C=O), 1487 (C=C), 1214 (C–O–C). LC-MS (*m/z*): Found: *m/z* 378.31. Calculated: [*M* + Na]<sup>+</sup> 378.

**Diethyl 2',6'-dimethyl-1',4'-dihydro-2,4'-bipyridine-3',5'-dicarboxylate (1f).** Yield 95%, mp 196°C. *R*<sub>f</sub> 0.65. IR spectrum, ν, cm<sup>-1</sup>: 3100 (N–H), 2927 (C–H), 1685 (C=O), 1632 (C=O), 1504 (=C–H and ring C=C), 1428 (C=C), 1377 (CH<sub>3</sub> in O–CH<sub>2</sub>–CH<sub>3</sub>), 1300 (C–N in C<sub>Ar</sub>–N), 1266 (C–O–C). <sup>1</sup>H NMR, δ, ppm: 1.12 s (3H, CH<sub>3</sub>), 2.32(q, 2H, CH<sub>2</sub>), 2.48 t (3H, CH<sub>3</sub>), 4.15 s (1H, CH), 4.72H s (1H, NH). LC-MS (*m/z*): Found: *m/z* 368.28 [*M* + K]<sup>+</sup>. Calculated: [*M* + K]<sup>+</sup> = 369.

**Diethyl 2,6-dimethyl-4-(3-nitrophenyl)-1,4-dihydropyridine-3,5-dicarboxylate (1g).** Yield 75%, mp 173°C. *R*<sub>f</sub> 0.65. IR spectrum, ν, cm<sup>-1</sup>: 3343 (N–H), 2888 (C–H), 1702 (C=O), 1642 (C=O), 1523 (=C–H and ring C=C), 1485–1433 (C=C), 1369 (CH<sub>3</sub> in O–CH<sub>2</sub>–CH<sub>3</sub>), 1346 (C–N in C<sub>Ar</sub>–N). <sup>1</sup>H NMR spectrum, δ, ppm: 1.19 t (3H, CH<sub>3</sub>), 2.42 q (2H, CH<sub>2</sub>), 2.466 s (3H, CH<sub>3</sub>), 5.09 s (1H, CH), 6.46 s (1H, NH).

**Diethyl 4-(furan-3-yl)-2,6-dimethyl-1,4-dihydropyridine-3,5-dicarboxylate (1h).** Yield 70%, mp 169°C.  $R_f$  0.70. IR spectrum,  $\nu$ ,  $\text{cm}^{-1}$ : 3344 (N–H), 2960 (C–H), 1697 (C=O), 1644 (C=O), 1539 (=C–H and ring C=C), 1475 (C=C), 1369 ( $\text{CH}_3$  in O– $\text{CH}_2$ – $\text{CH}_3$ ), 1320 (C–N in  $\text{C}_{\text{Ar}}$ –N), 1296 (C–O–C).  $^1\text{H}$  NMR spectrum,  $\delta$ , ppm: 1.23 t (3H,  $\text{CH}_3$ ), 2.18 q (2H,  $\text{CH}_2$ ), 2.32 s (3H,  $\text{CH}_3$ ), 4.30 s (1H, NH), 5.19 s (1H, CH).

**Diethyl 4-(3-bromophenyl)-2,6-dimethyl-1,4-dihydropyridine-3,5-dicarboxylate (1i).** Yield 65%, mp 212°C.  $R_f$  0.75.  $^1\text{H}$  NMR spectrum,  $\delta$ , ppm: 1.05 t (3H,  $\text{CH}_3$ ), 2.12 s (3H,  $\text{CH}_3$ ), 2.30 q (2H,  $\text{CH}_2$ ), 5.00 s (1H, CH), 5.82 s (1H, NH).

**Diethyl 4-(4-bromophenyl)-2,6-dimethyl-1,4-dihydropyridine-3,5-dicarboxylate (1j).** Yield 60%, mp 211°C.  $^1\text{H}$  NMR spectrum,  $\delta$ , ppm: 1.41 t (3H,  $\text{CH}_3$ ), 2.32 s (3H,  $\text{CH}_3$ ), 2.41 q (2H,  $\text{CH}_2$ ), 4.41 s (1H, NH), 5.19 s (1H, CH).

#### CONCLUSIONS

A simple, efficient and green method of synthesis of substituted 1,4-dihydropyridines via a one-pot three component coupling of aromatic aldehydes, 1,3-dicarbonyl compounds and ammonium acetate catalysed by  $\text{CoCl}_2$  and K-10 montmorillonite is developed. The advantages of this method include operational simplicity, short reaction time, use of relatively inexpensive, commercially available catalysts and high yields of products. Screening for antibacterial activity of products was carried out.

#### ACKNOWLEDGMENTS

Authors are thankful to the Department of Chemistry, Jankidevi Bajaj College of Science, Wardha for the support to carry out this research work.

#### REFERENCES

- Vijesh, A.M., Isloor, A.M., Peethambar, S.K., Shivananda, K.N., Arulmoli, T., and Isloor, N.A., *Eur. J. Med. Chem.*, 2011, vol. 46, no. 11, p. 5591. doi 10.1016/j.ejmech.2011.09.026
- Klusa, V., *Pharmacol. Res.*, 2016, vol. 113, p. 754. doi 10.1016/j.phrs.2016.05.017
- Janis, R.A. and Triggle, D.J., *J. Med. Chem.*, 1983, vol. 26, p. 775. doi 10.1021/jm00360a001
- Bocker, R.H. and Guengerich, E.P., *J. Med. Chem.*, 1986, vol. 29, p. 1596. doi 10.1021/jm00159a007
- Gordeev, M.F., Patel, D.V., and Gordon, E.M., *J. Org. Chem.*, 1996, vol. 61, p. 924. doi 10.1021/jo951706s
- Sunkel, C.E., Fau de Casa-Juana, M.F., and Santos, L., *J. Med. Chem.*, 1992, vol. 35, p. 2407. doi 10.1021/jm00091a008
- Matowe, W.C., Ramesh, M., and Iqbal, N., *J. Med. Chem.*, 1995, vol. 38, p. 2851. doi 10.1021/jm00015a007
- Bossert, F., and Vater, W., *Med. Res. Rev.*, 1989, vol. 9, no. 3, p. 291. doi 10.1002/med.2610090304
- Anand, K., Ananda kumar, S., Singh, S., Chaturgoon, A.A., and Gengan, R.M., *J. Photochem. Photobiol., B: Biol.*, 2016, vol. 165, p. 266. doi 10.1016/j.jphotobiol.2016.10.009